

**ACOUSTIC RADIATION FORCES AND TORQUES ON ELASTIC MICRO RINGS**

by

**FATEMEH MALEKABADI**

Submitted to the Graduate School of Engineering and Natural Sciences

in partial fulfilment of

the requirements for the degree of Doctor of Philosophy

Sabancı University

April 2023

# ACOUSTIC RADIATION FORCES AND TORQUES ON ELASTIC MICRO RINGS

Approved by:

Prof. Serhat Yesilyurt .....

(Dissertation Supervisor)

Assoc. Prof. Ayhan Bozkut .....

Assoc. Prof. Bekir Bediz.....

Assoc. Prof. Ahmet Fatih Tabak.....

Assist. Prof. Onur Özcan.....

Date of Approval: April, 2023

FATEMEH MALEKABADI 2023 ©

All Rights Reserved

# ABSTRACT

## ACOUSTIC RADIATION FORCES AND TORQUES ON ELASTIC MICRO RINGS

FATEMEH MALEKABADI

MECHATRONICS ENGINEERING Ph.D DISSERTATION, APRIL 2023

Dissertation Supervisor: Prof. Serhat Yesilyurt

Keywords: acoustic radiation force, acoustic radiation torque, scattering, fluid-particle interaction, finite element method

Acoustic radiation forces (ARFs) and torques (ARTs), which arise from the scattering of acoustic waves by suspended particles in a fluid, have attracted considerable attention for manipulating particles in different fields. Considering biocompatible nature of acoustic fields and their potential biomedical applications such as handling biological cells, which can have a variety of shapes, sizes, and orientations, it is necessary to study the ARFs and ARTs on non-spherical particles. This dissertation analyses ARFs and ARTs on ring-shaped microstructures subjected to a standing wave using a finite-element method (FEM). Two numerical models are employed to study the viscous effects in addition to the geometrical and physical parameters. Significant fluctuations in ART are observed for specific combinations of geometric and physical characteristics as a resonance indicator. Furthermore, effects of size, density, and microstreaming on secondary ARFs caused by the re-scattering of the waves from its neighboring particles are investigated. The results reveal that microstreaming close to the pressure node can lead to attractive forces in the wave direction. Besides, the relative effect of secondary ARFs due to self-scattering is studied using segmented-ring simulations. Moreover, a comparison is made between FEM and chain-of-spheres method, a reduced-order and computationally efficient model. The torque estimations deviate dramatically; however, the rapid evaluations of forces match well. The thesis findings are applicable to development of precise, efficient, and selective acoustofluidic devices for manipulation, trapping and coagulation purposes for ring-like elastic microfilaments and slender bodies. These results also can be used in directional reinforcing of ring-shaped composites.

# ÖZET

## ELASTİK MİKRO HALKALAR ÜZERİNDEKİ AKUSTİK RADYASYON KUVVETLERİ VE TORKLARI

FATEMEH MALEKABADI

MEKATRONİK MÜHENDİSLİĞİ DOKTORA TEZİ, NISAN 2023

Tez Danışmanı: Prof. Dr. Serhat Yeşilyurt

Anahtar Kelimeler: akustik radyasyon kuvveti, akustik radyasyon torku, saçılma, sıvı-  
parçacık etkileşimi, sonlu elemanlar yöntemi

Akustik dalgaların bir akışkan içinde asılı kalan parçacıklar tarafından saçılmasından kaynaklanan akustik radyasyon kuvvetleri (ARF'ler) ve torklar (ART'ler), farklı alanlarda parçacıkları manipüle etmek için büyük ilgi çekmiştir. Akustik alanların biyouyumlu doğası ve biyomedikal uygulamaların potansiyeli göz önüne alındığında, biyolojik hücrelerin işlenmesi gibi, çeşitli şekil, boyut ve yönlere sahip olabilen, küresel olmayan parçacıklar üzerindeki ARF'leri ve ART'leri incelemek gerekir. Bu çalışmada, bir sonlu elemanlar yöntemi (FEM) kullanılarak, duran dalgaya maruz kalan halka şeklindeki mikro yapılar üzerindeki ARF'leri ve ART'leri analiz edilmiştir. Geometrik ve fiziksel parametrelere ek olarak viskoz etkileri incelemek için iki sayısal model kullanılmıştır. Bir rezonans göstergesi olarak geometrik ve fiziksel özelliklerin belirli kombinasyonları için ART'de önemli dalgalanmalar gözlemiştir. Ayrıca, dalgaların komşu parçacıklardan yeniden saçılmasının neden olduğu ikincil ARF'ler üzerindeki boyut, yoğunluk ve mikro akışın etkileri araştırılmıştır. Sonuçlar basınç düğümüne yakın mikro akışın dalga yönünde çekici kuvvetlere yol açabileceğini ortaya koymaktadır. Ayrıca, ikincil ARF'lerin kendiliğinden saçılma nedeniyle göreceli etkisi, parçalı halka simülasyonları kullanılarak incelenmiştir. Dahası, FEM ile küreler zinciri adı verilen, azaltılmış sıralı ve hesaplama açısından verimli bir model arasında bir karşılaştırma yapılmıştır. Tork tahminleri önemli ölçüde sapıyor; ancak, kuvvetlerin hızlı değerlendirmeleri iyi bir şekilde eşleşmektedir. Tez bulguları, halka benzeri elastik mikrofilamentler ve ince groveler için manipülasyon, yakalama ve pıhtılaşma amaçlarına yönelik hassas, verimli ve seçici akusto-akışkan cihazların geliştirilmesine uygulanabilir. Bu sonuçlar halka şeklindeki kompozitlerin yönlü takviyesinde de kullanılabilir.

## ACKNOWLEDGEMENTS

I would like to express my sincere gratitude to my supervisor, Prof. Serhat Yesilyurt, for his guidance, support, and valuable insights throughout my doctoral studies. His commitment to excellence has been an inspiration to me, and I am deeply grateful for the opportunities that he has provided me to develop my research skills.

I am also grateful to the members of my thesis committee, Assoc. Prof. Ayhan Bozkurt and Assoc. Prof. Bekir Bediz, for their constructive feedback and helpful suggestions, which have greatly contributed to the quality of my research.

I would like to extend my heartfelt thanks to my family for their unwavering support and encouragement, for their love, encouragement, and for the sacrifices they made to give me the best education possible, even though they are far away from me. Their faith in me has been a great motivation.

I am grateful to my husband, Hossein, who has been with me every step of the way during this journey. His patience, understanding, and encouragement have been a constant source of strength and support for me. I am blessed to have him as my partner in life.

Finally, I would like to thank all of the participants in my research project, Hakan Osman Çaldag and Milad Shojaeian, without whom this thesis would not have been possible. Your willingness to share your experiences and insights with me has been invaluable, and I am deeply grateful for your contributions.

## TABLE OF CONTENTS

<b>LIST OF TABLES</b> .....	ix
<b>LIST OF FIGURES</b> .....	x
<b>LIST OF ABBREVIATIONS</b> .....	xiv
<b>1. INTRODUCTION</b> .....	15
1.1. Background.....	19
1.1.1. Primary Acoustic Radiation Force in an Inviscid Fluid.....	19
1.1.2. Primary Acoustic Radiation Forces in a Viscous Fluid.....	22
1.1.3. Secondary Forces.....	26
1.2. Novelties of the Thesis.....	31
<b>2. METHODOLOGY</b> .....	33
2.1. Governing equations.....	33
2.1.1. Perturbation Theory.....	33
2.1.2. Deformation of Solid Particles.....	35
2.1.3. Boundary and Coupling Conditions.....	35
2.2. Acoustic Radiation Forces on a Ring.....	36
2.2.1. Primary Acoustic Radiation Forces.....	37
2.3. Acoustic Radiation Torques on a Ring.....	38
2.3.1. Secondary Radiation Forces on a Ring.....	39
2.4. Finite Element Method Simulations.....	39
2.4.1. For an Inviscid Fluid.....	39
2.4.2. For a Viscous Fluid.....	42
2.4.3. For a Pair of Particles.....	44
2.4.4. Mesh Convergence.....	45
2.4.5. Validation and Verification of the Model.....	48
<b>3. ACOUSTIC RADIATION FORCES AND TORQUES ON A RING</b> .....	51
3.1. Effects of the Ring's Placement.....	51
3.2. Effects of the Ring Geometry.....	54
3.2.1. Rotation Angle.....	54
3.2.2. Major and Minor Radius.....	60
3.3. Effects of the Physical Parameters.....	63
<b>4. SECONDARY FORCES AND SCATTERING EFFECTS</b> .....	68
4.1. Comparison with Chain of Spheres Approach.....	68

4.1.	Self Scattering.....	70
4.2.	Microstreaming Effects on the Secondary Forces .....	76
4.2.1.	Ring-Ring Interactions.....	76
4.2.2.	Sphere-Sphere Interactions .....	81
4.2.3.	Ring-Sphere Interactions .....	82
5.	<b>CONCLUSIONS</b> .....	86
5.1.	Future Work.....	88
	<b>BIBLIOGRAPHY</b> .....	90
	<b>APPENDIX A</b> .....	100

## LIST OF TABLES

Table 2.1. Fluid properties and geometric parameters for the reference ring.....	41
Table 2.2. Solid properties of materials and the geometric parameters for the reference ring. .....	41
Table 2.3. Geometric parameters of the ring used for the convergence studies of the 3D FEM model.....	45
Table 2.4. Comparison of 3-dimensional FEM model results with the literature.....	49

## LIST OF FIGURES

Fig 1.1 Some applications of ring-shaped structures: **(I)** Active Brownian ring polymer (Mousavi et al., 2019), **(II)** sedimenting elastic rings (Gruziel-Słomka et al., 2019), **(III)** Particle reinforced composites (Egbo, 2021), **(IV)** Rigid toroidal inhomogeneity and its effect on composites (Krasnitskii et al., 2019), **(V)** Poloidal Flow and Toroidal Particle Ring Formation (Rezk et al., 2014), **(VI)** Toroidal Bubbles (Alloul et al., 2022)..... 17

Fig 1.2. (a) Acoustophoresis of disk-shaped microparticles (Garbin et al., 2015), (b) Scattering of acoustic wave from a small particle (Bruus, 2012), (c) Finite element model for calculation of radiation forces on a compressible sphere (Glynne-Jones et al., 2013) ..... 21

Fig 1.3. (a) Numerical simulations to find acoustic forces on rigid cylinders (Wang & Dual, 2009), (b) Finite-element modeling for calculation of acoustic forces on heavy compressible spheres (Baasch et al., 2019)..... 24

Fig 1.4. Finite-element modeling of secondary forces between spheres (Hoque & Sen, 2020) ..... 29

Fig 2.1. (a) Geometric parameters of the ring. (b) Ring is positioned inside a fluidic domain with radiation conditions at the boundaries in the simulation domain. (c) Ring rotation angle depiction,  $\theta$ . ..... 40

Fig 2.2. Viscous Simulation domain with the ring placed inside a fluidic domain with PML, nonreflecting radiation conditions at the boundaries. .... 44

Fig 2.3. Depiction of simulated geometries. (a)-(c) show the configuration where the rings are placed along the propagation axis of the acoustic field and. (a) depict the 3-dimensional geometry, (b) show the arrangement of the rings alongside the geometric parameters and (c) show the 2-dimensional, axisymmetric domains simulated with the standing acoustic field. Note that the ring or domain dimensions are not to the scale. .... 45

Fig 2.4. Mesh on a) a ring particle, b) fluid domain. .... 46

Fig 2.5. Convergence of  $F^{rad}$  with respect to the degrees of freedom..... 47

Fig 2.6. Mesh convergence studies with respect to the maximum element size. .... 48

Fig 2.7. a) comparison of our numerical model for a ring and cylinder in water b) ARF versus frequency for a sphere in water compared with analytical results considering viscosity effects. .... 49

Fig 2.8. The comparison of the secondary forces between spheres (sphere1: sphere2). Dashed lines are the simulation results, datapoints are from Hoque and Sen (Hoque & Sen, 2020). .50

Fig 3.1. The radiation force and torque with respect to  $\Delta z$  in a standing wave on a horizontal ( $\theta = 0$ ) and tilted ( $\theta = 30^\circ$ ) polystyrene ring in water for a  $f = 2 \text{ MHz}$ . a) Color plot of the pressure amplitude, b) Change of  $p$  with respect to  $\Delta z$  and the corresponding c)  $F^{rad}$  and d)  $\tau^{rad}$  profiles. ....52

Fig 3.2. The radiation force and torque with respect to  $\Delta z$  in a standing wave on a horizontal ( $\theta = 0^\circ$ ) and tilted ( $\theta = 30^\circ$ ) polystyrene ring in a viscous water for  $f = 2 \text{ MHz}$ . a)  $F^{rad}$  and b)  $\tau^{rad}$  profiles. ....53

Fig 3.3. a) Comparison of the acoustic radiation forces corresponding to inviscid and viscous fluids b) Acoustic radiation torque comparison of viscous and inviscid fluids. ....54

Fig 3.4. The change of (a)  $F^{rad}$  and (b)  $\tau^{rad}$  with respect to  $\theta$ . (c) shows the ring's orientation when  $\theta = 0^\circ$  and (d) shows the orientation when  $\theta = 90^\circ$ . The standing field is applied in the  $z$ - direction. (e) shows the pressure and momentum flux-driven component of the radiation torque on a polystyrene ring when  $\Delta z = 0$ . ....55

Fig 3.5. The change of (a)  $F^{rad}$  and (b)  $\tau^{rad}$  with respect to  $\theta - \Delta z$ . The standing field is applied in the  $z$ - direction on a polystyrene ring in an inviscid fluid when  $\theta$  varies between  $0^\circ$  and  $90^\circ$ . ....56

Fig 3.6. (a,b) comparison of Acoustic radiation forces and torques of inviscid and viscous fluids for  $\Delta z = \lambda/8$ , (c) Acoustic radiation torques and contribution of pressure and velocity for a polystyrene ring in viscous fluid for  $\Delta z = 0$ , (d) Comparison of acoustic radiation torque of inviscid and viscous fluid for  $\Delta z = 0$ . ....57

Fig 3.7 The change of (a)  $F^{rad}$  and (b)  $\tau^{rad}$  with respect to  $\theta - \Delta z$ . The standing field is applied in the  $z$ - direction on a polystyrene ring in a viscous fluid when  $\theta$  varies between  $0^\circ$  and  $90^\circ$ . ....58

Fig 3.8 The change of (a)  $F^{rad}$  and (b)  $\tau^{rad}$  with respect to  $\theta - \delta a$ . The standing field is applied in the  $z$ - direction on a polystyrene ring in a viscous fluid with different viscosities when  $\theta$  varies between  $0^\circ$  and  $90^\circ$ . ....59

Fig 3.9 The change of (a)  $F^{rad}$  and (b)  $\tau^{rad}$  with respect to  $\theta - \rho_p/\rho_0$ . The standing field is applied in the  $z$ - direction in a viscous fluid with different densities for the ring when  $\theta$  varies between  $0^\circ$  and  $90^\circ$  at  $\Delta z = \lambda/8$ . ....59

Fig 3.10. (a) Change of  $F^{rad}$  with respect to  $a$ , (b) change of  $\tau^{rad}$  with respect to  $a$ , (c) change of  $F^{rad}$  with respect to  $R$  and (d) Change of  $\tau^{rad}$  with respect to  $R$ . ....60

Fig 3.11. The displacement ((a)-(b)) and the pressure ((c)-(d)) distributions on non-resonating ((a) and (c)) and resonating ((b) and (d)) rings. .... 62

Fig 3.12. Comparison of results for viscous and inviscid fluids (a) Change of  $F^{rad}$  with respect to  $a$ , (b) change of  $\tau^{rad}$  with respect to  $a$ , (c) change of  $F^{rad}$  with respect to  $R$  and (d) Change of  $\tau^{rad}$  with respect to  $R$ ..... 63

Fig 3.12. The change of (a)  $F^{rad}$  and (b)  $\tau^{rad}$  with respect to  $\phi$ . The change of (c)  $F^{rad}$  and (d)  $\tau^{rad}$  with respect to  $f$ . Insets show the deformations (5000 times scaled-up) and Mises stresses in the rings. .... 65

Fig 3.14. Comparison of the results of viscous and inviscid fluids; The change of (a)  $F^{rad}$  and (b)  $\tau^{rad}$  with respect to  $f$  (c) Comparison of  $F^{rad}$  with considering different contributions. The change of (d)  $F^{rad}$  and (e)  $\tau^{rad}$  with respect to  $\rho_0/\rho_p$  and  $\delta/a$ ..... 67

Fig 4.1. Schematic of chain-of-spheres methodology. (a) Shows the original ring geometry, (b) shows the representation of the ring with  $N_{sph} = 14$  spheres with radius  $a$  as placed along the circle of the ring which is  $R$  away from the center of the ring. The circle is shown in red dashes. .... 69

Fig 4.2. Comparison of the radiation forces ((a), (c) and (e)) and torques ((b), (d) and (f)) obtained from the FEM model and with the CoS method. (a) and (b) the results for polystyrene ring, (c) and (d) the results for copper ring and (e) and (f) the results for aluminum ring. .... 70

Fig 4.3. (a) The depiction of the ring decomposed into segments; local acoustic radiation forces (ARF) on each segment of polystyrene (b), copper (c) and aluminum (d) rings. ARF on each individual segment placed in the acoustic field without others is shown with black circles; forces on the detached segments forming a ring (see the picture in (a)) is shown with red stars; and the forces on the complete ring composed of segments in contact are shown with blue squares..... 72

Fig 4.4. local acoustic radiation forces (ARF) on each segment of polystyrene and contribution of pressure and velocity terms to ARF for  $f = 0.6MHz$ ; (a) the forces on the complete ring composed of segments in contact, (b) forces on the detached segments forming a ring (c) forces on each individual segment placed in the acoustic field without others (see the picture in Fig.4.3a) ..... 73

Fig 4.5. local acoustic radiation forces (ARF) on each segment of aluminum ring and contribution of pressure and velocity terms to ARF; (a) the forces on the complete ring composed of segments in contact, (b) forces on the detached segments forming a ring (c) forces on each individual segment placed in the acoustic field without others (see the picture in Fig.

4.3a). .....	74
Fig 4.6. local acoustic radiation forces (ARF) on each segment of copper ring and contribution of pressure and velocity terms to ARF; (a) forces on the complete ring composed of segments in contact; (b) forces on the detached segments forming a ring; (c) forces on each individual segment placed in the acoustic field without others (see the picture in Fig. 4.3a). .....	75
Fig 4.7. Acoustic radiation forces on particle 2 with respect to surface-to-surface distances, $d$ , ( $1\mu\text{m}$ to $10\mu\text{m}$ ) for various sizes of the rings at $f = 500\text{KHz}$ and $R = 10\mu\text{m}$ with various combination of $a$ : (a,b,d,e) Polystyrene rings ,(c,f) First particle, a copper ring, centered at nodal plane; second particle is a polystyrene ring away from the nodal plane , (g,h) Copper rings (yellow rings represent the copper rings).....	77
Fig 4.8. Streaming patterns and second-order velocity field are shown for polystyrene rings at $f = 500\text{KHz}$ and $R = 10\mu\text{m}$ with various inter-distances, $d = 10,3,1\mu\text{m}$ respectively (a-c) for $a_1 = a_2 = 5\mu\text{m}$ , (a-c) for $a_1 = a_2 = 0.5\mu\text{m}$ . .....	79
Fig 4.9. Streaming patterns and second-order velocity field are shown for polystyrene rings at $f = 500\text{KHz}$ and $R = 10\mu\text{m}$ with various inter-distances, $d = 10,3,1\mu\text{m}$ respectively (a-c) for $a_1 = 5\mu\text{m}$ , $a_2 = 0.5\mu\text{m}$ , (a-c) for $a_1 = 0.5\mu\text{m}$ , $a_2 = 5\mu\text{m}$ . .....	80
Fig 4.10. Streaming patterns and second-order velocity field are shown for polystyrene and copper rings at $f = 500\text{KHz}$ and $R = 10\mu\text{m}$ with various inter-distances, $d = 10,3,1\mu\text{m}$ respectively (a-c) for $a_1 = 5\mu\text{m}$ copper, $a_2 = 0.5\mu\text{m}$ polystyrene , (a-c) for $a_1 = 0.5\mu\text{m}$ copper, $a_2 = 5\mu\text{m}$ polystyrene . .....	81
Fig 4.11. Acoustic radiation forces shown for polystyrene spheres at $f = 500\text{KHz}$ and reported forces are forces on the second particle.....	82
Fig 4.12. Acoustic radiation forces shown for polystyrene sphere and ring at $f = 500\text{KHz}$ and (first particle is ring with $R = 10\mu\text{m}$ and second particle is sphere): reported forces are forces on the second particle.....	83
Fig 4.13. Acoustic radiation forces shown for polystyrene sphere and copper ring at $f = 500\text{KHz}$ and (first particle is ring with $R = 10\mu\text{m}$ and second particle is sphere). .....	84
Fig 4.14. Streamline patterns for polystyrene sphere and copper ring in water subjected to a standing wave at $f = 500\text{KHz}$ at different inter-distances: a) $d = 1\mu\text{m}$ b) $d = 10\mu\text{m}$ c) $d = 1\mu\text{m}$ ; first particle is a ring with $a = 5\mu\text{m}$ and $R = 10\mu\text{m}$ , and second particle is a sphere with the radius of $a = 5\mu\text{m}$ . .....	85

## LIST OF ABBREVIATONS

Acoustic Radiation Force	
(ARF).....	5
Acoustic Radiation Torque	
(ART).....	17
Chain-Of-Spheres	
(Cos).....	20
Computational Fluid Dynamic	
(CFD).....	18
Degrees Of Freedom	
(DOF).....	48
Finite Volume Method	
(FVM).....	16
Finite Element Method	
(FEM).....	20
Non-Reflection Radiation Boundary Conditions	
(NRBC).....	42
Perfectly Matched Layers	
(PML).....	23

## 1. INTRODUCTION

Applying a suitable force to control the motion of fluids and objects at microscale may be based on, for instance, the transfer of energy and momentum from electromagnetics (Kummer et al., 2010; Cao et al., 2020), optics (Fan et al., 2014; Mallea et al., 2018), chemicals (Manjare et al., 2013); (Yamamoto & Shioi, 2015), or acoustic waves (Friend & Yeo, 2011; Rufo et al., 2022). In this thesis, the focus is on the strengthening of underlying theoretical understandings of acoustic waves that can be applicable to life sciences, chemistry, and material development. The acoustic radiation force (ARF), the acoustic interaction force, and the Stokes drag from environmental acoustic streaming all contribute to the motion of objects in acoustic fields in fluids, known as acoustophoresis.

Acoustic radiation force (ARF) is a time-averaged force exerted by sound waves on the surface of obstacles due to radiation pressure. Manipulation of microparticles using ARF has received significant interest in recent years due to its applications in a variety of fields, including medicine (Rufo et al., 2022), biology (Saeidi et al., 2020), imaging (Wang, 2018), chemistry (Chen et al., 2022), material science for particle filtration (Fakhfoury et al., 2016), sorting (Wang et al., 2018), trapping (Li et al., 2021), handling (Laurell et al., 2007), mixing (Huang et al., 2013), and pumping (JunáHuang, 2014). Ultrasonic manipulation is a contactless method which can move suspended objects in a fluid (e.g., cells, bacteria, fibers, bubbles, droplets, swimmers) to desired positions, such as lines or patterns.

In addition to ARF, acoustic radiation torque (ART) arises from the interaction of acoustic waves with the particle and the transfer of angular momentum, influencing the acoustic manipulation. Along with the translational displacement brought on by the ARF, the controllable rotation of the particle by using the ART offers an additional degree of freedom. Potential applications for such controlled rotation, including disease diagnosis, micro-motors, micro-valves, and lab-on-a chip applications, would involve micro robotic tasks.

ARF and ART have widely been investigated on simple particle shapes. However, some of

these studies have taken the complex shape of particles into account generally, viscosity of the fluid was ignored. Thus, a more comprehensive study is needed on particles of different shapes that are utilized in different fields, such as biology, as biological cells have various shapes, sizes, and orientations in microfluidic chips. Such a study can also be helpful in reinforcing composites while orienting anisotropic particles. Composites, known as engineered materials, combine two or more basic materials. The characteristics of these constituent materials, as well as their relative volume fractions and configurations in the material system, lead to the distinctive qualities of these composites. Composites can be created to meet the specific geometrical, structural, mechanical, chemical, and even aesthetic requirements depending on the intended purpose. These synthetic materials are used in a variety of industries, including construction (for buildings and bridges), the automotive sector (for car bodywork), the aerospace and naval sector (for ships and boats), as well as biomedical fields.

The objective of this thesis is to characterize ARFs and ARTs on ring-shaped elastic rods numerically, via a computational fluid dynamic (CFD) model, an indispensable tool for experimental design and optimization purposes. Proteins, DNA, algae, bacteria, polymers, and red blood cells are only a few examples of compressible objects that can be deformed into ring-shaped structures. Examples of images from previous studies related to ring-shaped structures are shown in Fig 1.1.

Further, previous studies have mostly considered the effects of ARF and ART on a single particle; however, in various applications, numerous particles interact with the acoustic field. The interaction force, or secondary force, stems from the presence of multiple particles and results in an additional scattering that can influence the manipulation tasks. Hence, in order to obtain precise manipulation in real tasks such as in vivo ultrasonic applications, further study on the effects of ARFs and ARTs on multiple particles with irregular shapes is greatly needed as acoustic fields have been widely adopted in medical applications for their bio-compatible and non-invasive nature.

Moreover, an object's surface deformations and scattering in a viscous fluid result in microstreaming (also known as acoustic streaming), which affects the object's overall ARF. Further investigation and understanding of microstreaming offer potential for more effective use of acoustofluidic devices for handling particles. Such understanding has a huge potential to allow researchers to either suppress or manipulate microstreaming to serve useful purposes. When studying microstreaming in microchannels, an inevitable physical phenomenon is the viscous boundary layer,  $\delta$ , a constrained area near a fluid-solid boundary where the fluid

velocity adjusts to the solid velocity. Nevertheless, the boundary layer experiences substantial time-averaged viscous effects that cause microstreaming and dissipation. In addition to the boundary-driven streaming produced by the viscous boundary layer, bulk-driven streaming can also occur due to viscous processes outside the boundary layer. In a microfluidic environment, this type of streaming was frequently disregarded in the literature, but as demonstrated in this thesis, it may be crucial in many circumstances with the aim of improving particle manipulations.

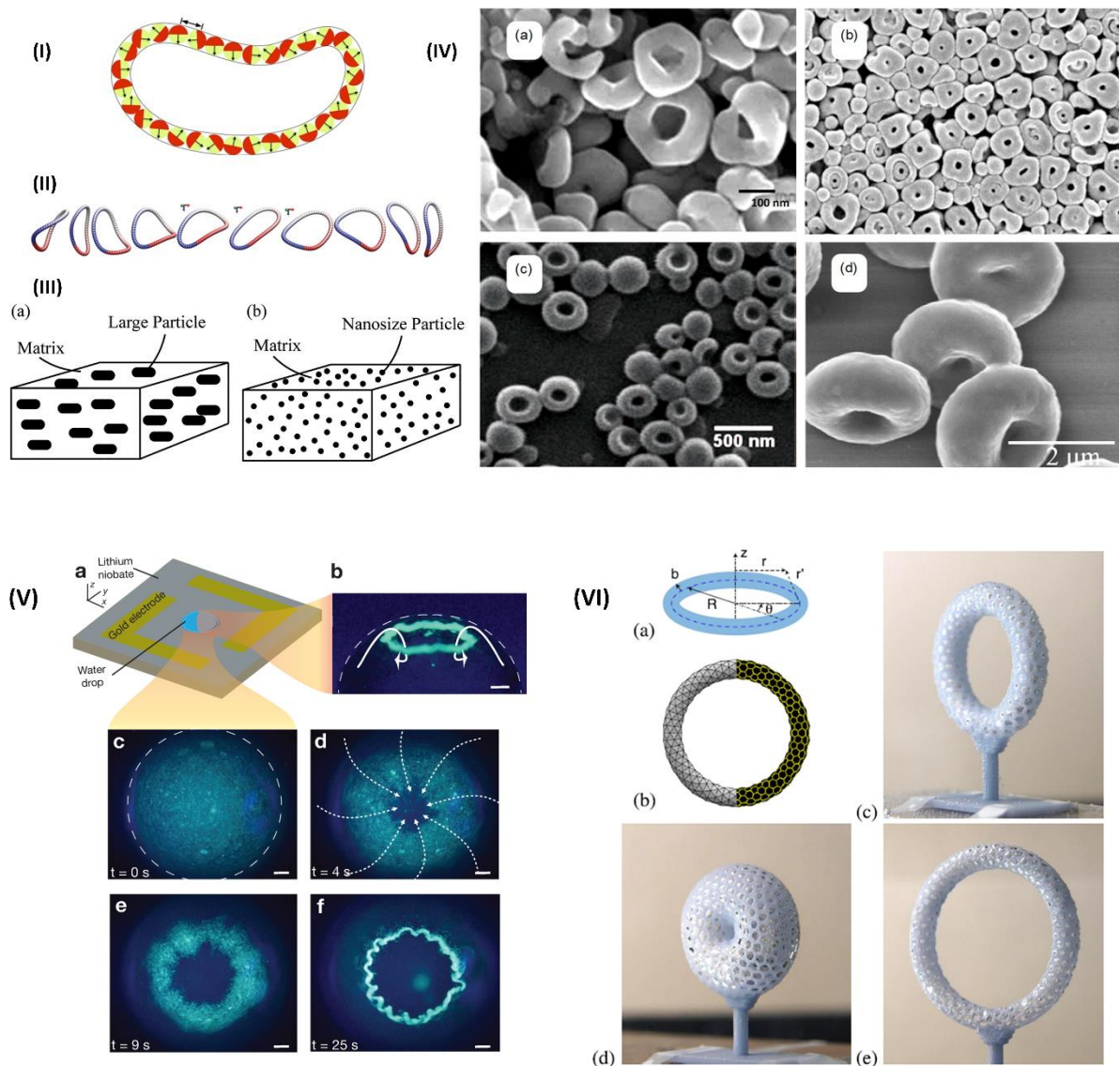


Fig 1.1 Some applications of ring-shaped structures: **(I)** Active Brownian ring polymer (Mousavi et al., 2019), **(II)** sedimenting elastic rings (Gruziel-Słomka et al., 2019), **(III)** Particle reinforced composites (Egbo, 2021), **(IV)** Rigid toroidal inhomogeneity and its effect on composites (Krasnitskii et al., 2019), **(V)** Poloidal Flow and Toroidal Particle Ring Formation (Rezk et al., 2014), **(VI)** Toroidal Bubbles (Alloul et al., 2022)

This thesis presents an analysis of acoustic radiation forces (ARFs) and torques (ARTs) on ring-shaped slender microstructures under a standing wave in both an inviscid fluid and a

viscous fluid using a three-dimensional finite-element-method (FEM) model. The influence of geometric and physical parameters on the primary acoustic radiation forces, torques and streaming is characterized. The primary acoustic radiation force is mainly caused by the scattered wave on a single particle, whereas the secondary force is caused by the re-scattering of the waves from its neighboring particles. In applications such as particle trapping, acoustic cavitation, acoustic coagulation and precipitation of aerosols, and biological ultrasonics, this secondary force is extremely significant. In particular, the effect of microstreaming on these primary and secondary forces is investigated in this thesis. The finite-element method (FEM) was used to calculate the secondary acoustic forces between two rings under a standing wave in an inviscid and viscous fluid. Furthermore, the FEM results were compared with a reduced-order model called chain-of-spheres (CoS), which works very well in estimating the radiation forces at a fraction of the computational cost but deviates significantly in torque evaluations. Lastly, a segmented ring was used to understand the relative effect of secondary forces due to self-scattering.

The conclusions offer guidance for improving ultrasonic control in biomedical applications as well as for the development of acoustic manipulation systems for biological cells and ring-like elastic microfilaments with arbitrary forms and orientations. Additionally, the ART produced by ultrasonic standing waves can improve fiber alignment, and our findings can also be applied to the directional reinforcement of composites in the form of rings.

## 1.1. Background

Acoustic radiation forces (ARFs) are typically divided into two types: primary forces and secondary forces. The primary ARF is mainly caused by the scattered wave experienced by a single particle, while the secondary ARF is caused by the interactions among multiple particles. Secondary radiation forces, also known as interaction or Bjerknes forces, arise when other particles exist in a fluid medium that causes additional incident waves to be scattered from the particles and re-scattering among the particles (Doinikov, 2003).

In a standing wave field, the primary ARF pulls the particle towards the pressure node or anti-node, depending on the acoustic contrast factor (Mitri, 2010). Since the primary ARF is zero at the pressure node, the secondary ARF becomes the dominant force and may affect particle motion and orientation (Doinikov, 1996). Secondary ARFs cause particles to attract or repel one another, which sometimes leads to the formation of stable multi-particle structures.

In accordance with the numerical nature of this thesis, seminal works for primary ARF in an inviscid fluid are introduced first; studies on primary ARF in a viscous fluid and secondary ARFs are then discussed, mostly through analytical and numerical studies.

### 1.1.1. Primary Acoustic Radiation Force in an Inviscid Fluid

Acoustic radiation forces (ARFs), which are caused by second-order pressure and momentum flux acting on a particle's surface in an inviscid fluid, are a versatile control for manipulating microparticles such as cells (Schmitt, 1929; Coakley et al., 1989; Haake et al., 2005; Peng et al., 2020), droplets and bubbles (Deshmukh et al., 2014; Li et al., 2021), particles (Glynne-Jones et al., 2009; Gong & Baudoin, 2021; Leão-Neto et al., 2021), organisms (Kvåle Løvmo et al., 2021), and colloids in microfluidic devices (Glynne-Jones et al., 2013).

ARF exerted on basic shapes like spheres and cylinders has received a great deal of attention in the literature. King was the first to investigate the effects of planar progressive and standing waves on incompressible spherical particles in an inviscid fluid (King, 1934). Gor'kov (Gor'kov, 1962) proposed a generalized potential for the computation of ARF for a variety of applications in inviscid fluids, while Yosioka and Kawasima extended King's analysis to compressible spheres (Yosioka & Kawasima, 1955). Simple analytical equations for ARFs

under travelling and standing acoustic waves were provided by Hasegawa and Yosioka (Hasegawa & Yosioka, 1969) and Hasegawa (Hasegawa, 1979), respectively.

Viscous effects on ARF have been taken into account in the literature (Doinikov, 1994; Doinikov, 1994; Settnes & Bruus, 2012), and thermal effects on ARF have also been thoroughly studied (Doinikov, 1997; Doinikov, 1997; Doinikov, 1997; Karlsen & Bruus, 2015), which is discussed in detail in the next section. For spheroidal objects, ARF has been investigated under different arbitrary acoustic fields: standing waves and Bessel beams (Mitri, 2008), travelling waves (Johnson et al., 2016), Gaussian quasi-standing field (Wu et al., 2016), a beam of the arbitrary wavefront (Silva & Drinkwater, 2018), and transient acoustic field (Wang et al., 2021).

King (King, 1935) also modeled the acoustic pressure on very thin and rigid disks; this theory has been further expanded for forces on disks (Xie & Wei, 2004), deformed droplets (Shi & Apfel, 1996), cylinders (Haydock, 2005; Mitri, 2005; Wang & Dual, 2009; Cai et al., 2010), and ellipsoids (Marston et al., 2006). Subsequently, experimental research focused on the role of ARF in cylindrical particle trapping (Mitri, 2006). For the ARF of a Bessel beam on rigid oblate and prolate spheroids, Mitri established an analytical formula (Mitri, 2015). Based on series expansion, Mitri evaluated the ARF and ART on a viscoelastic cylinder in an inviscid flow (Mitri, 2016).

Although significant research has used analytical solutions for ARF, numerical approaches are required, which avoid oversimplifications of the fluid and particle parameters. Numerical studies of ARF in the literature can be categorized into two types. The first discusses the subject as a fluid mechanics problem, with the acoustic field presented as a flow field. In one study, for example, the ARFs on cylinders were calculated using a finite volume method (FVM) (Wang & Dual, 2009). These findings were extremely consistent with the analytical calculations; however, employing the Navier-Stokes equations to solve for the entire flow field is very computationally costly. Such a method, therefore, is not practical, especially if only the radiation force computation is of interest. In another example, using a finite-difference time-domain method based on the Lagrangian specification of the flow field, the authors (Grinenko et al., 2012) calculated ARF directly from nonlinear governing equations; this method has no restrictions on particle geometry and no excessively restrictive boundary conditions. In another case, the boundary-element approach was used by Wijaya et al. (Wijaya & Lim, 2016; Wijaya & Lim, 2016) to investigate the ARFs and ARTs caused by acoustic radiation on spherical and non-spherical particles.

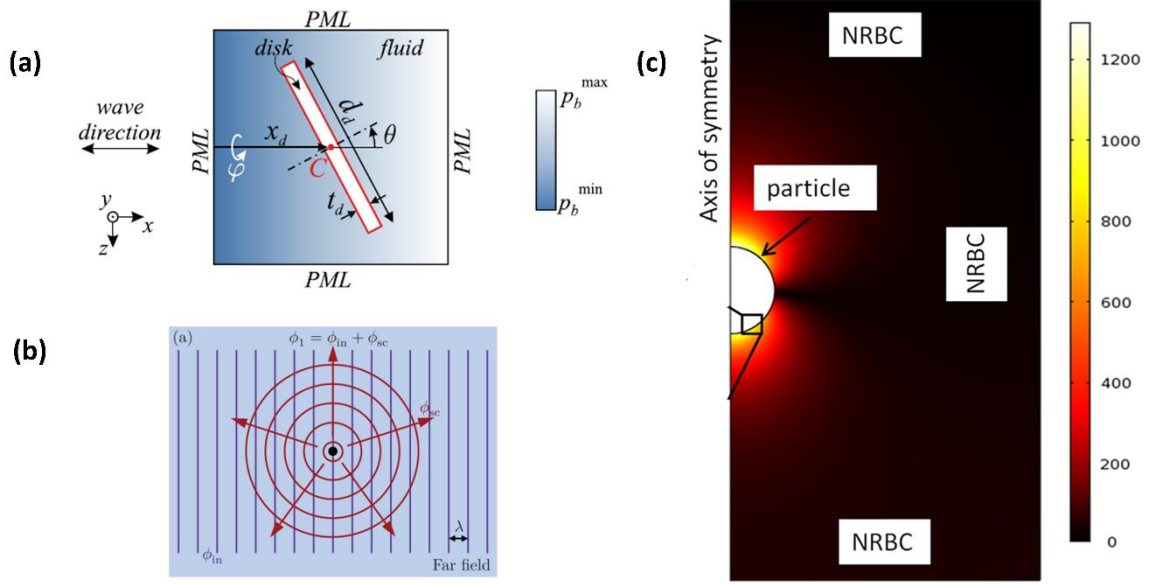


Fig 1.2. (a) Acoustophoresis of disk-shaped microparticles (Garbin et al., 2015), (b) Scattering of acoustic wave from a small particle (Bruus, 2012), (c) Finite element model for calculation of radiation forces on a compressible sphere (Glynne-Jones et al., 2013)

In the second category of numerical simulations for ARF, perturbation methods are used to solve the Helmholtz equation for the acoustic field, velocity, and fluid density. This method is used to determine the ARF on a spherical particle in a standing acoustic field by Glynne-jones et al. for an inviscid fluid shown in Fig 1.2. b (Glynne-Jones et al., 2013), and for a viscous fluid (Baasch et al., 2019). These studies used a two-dimensional axisymmetric geometry that takes advantage of spherical symmetry to further reduce processing expenses. A three-dimensional finite-element model was suggested by Garbin et al. to calculate the ARFs and ARTs acting on disk-shaped particles (Garbin et al., 2015). To prevent outgoing waves from being reflected, their fluid domain was surrounded by perfectly matched layers (PML), as shown in Fig 1.2a; other examples of using PMLs are shown in Fig 1.3. However, studies in the literature report that proper radiation boundary conditions perform just as well as PMLs while requiring less computational effort, can be seen in Fig 1.2c (Glynne-Jones et al., 2013). In particular, for complicated three-dimensional structures like helices at high acoustic frequencies for which the resolution of the acoustic field is more demanding, while perturbation-based methods are computationally more efficient, the computational expense may remain. Recently, Caldag & Yesilyurt (Caldag & Yesilyurt, 2020) introduced the chain-of-spheres (CoS)

reduced-order model to calculate the ARFs on thin objects in inviscid fluids by simulating the thin structure as a chain of tiny spheres, each of which has the same volume as the corresponding segment of the thin body. In this approach, the sum of the individual forces acting on small spheres was used to compute the overall radiation force on the thin structure. Depending on the incident acoustic wave type, this calculation was done analytically based on either plane wave-related expressions (Hasegawa & Yosioka, 1969) or plane quasi-stationary wave formulas (Hasegawa, 1979). In comparison to the results obtained from the direct numerical solution for the object placed in an acoustic field, this method was shown to be both incredibly computationally efficient and fairly accurate.

### 1.1.2. Primary Acoustic Radiation Forces in a Viscous Fluid

Computation of acoustic radiation force (ARF) in a viscous fluid is more challenging than for inviscid fluids due to the emergence of nonlinear phenomena such as streaming which affect the momentum transfer between the acoustic field and the particles. However, the viscosity of the surrounding fluid plays a significant role in achieving precise, efficient, and robust particle control in practical applications in medicine, biophysics, industry, and material science.

The influence of the viscosity and viscous boundary layer on the ARF acting on a spherical particle was studied initially by Westervelt (Westervelt, 1951; Westervelt, 1957). This researcher calculated ARF for fixed spheres which were small in comparison to the acoustic wavelength and viscous boundary layer. Later work (Zhuk, 1983; Zhuk, 1984) investigated ARF on a spherical particle that was free to move in a low viscous fluid, but similar to previous studies, this work ignored the compressibility of the particle and acoustic streaming. The authors concluded that viscosity could not be ignored under the condition of  $a \gg \delta$ , where  $\delta$  is boundary layer thickness,

$$\delta = \sqrt{(2\eta)/(\rho_0\omega)} \quad (1-1)$$

Subsequently, Danilov considered acoustic streaming in a viscous fluid on a spherical particle, but these analytical studies were for limited cases and disregarded, for example, heavy particles (Danilov, 1985; Danilov, 1986). ARF was derived for a rigid sphere in a viscous fluid by Doinikov (Doinikov, 1994) for an arbitrary particle size without any

limitation on its movement. Later, the compressibility of the spherical particle as well as the viscosity of the fluid, was regarded for computation of ARF (Doinikov, 1994). This work was expanded to develop (Doinikov, 1997) a general formula for a spherical particle in a viscous fluid considering thermal effects. The formula from this work can be used in any symmetric acoustic wave for any spherical particle with specific limitations on its size with respect to the wavelength and boundary layer thickness,  $\delta \ll a \ll \lambda$  and  $a \ll \delta \ll \lambda$ .

As a result of advancements in microfabrication technologies that enable the integration of acoustic fields and microfluidic chips, ARF has become more attractive for manipulation of small particles. Thus, Settnes and Bruus (Settnes & Bruus, 2012) corrected analytically computed acoustic radiation force on a compressible spherical particle in a viscous fluid to encompass any particle with  $a, \delta \ll \lambda$ . Their solution has proven applicable to lab-on-a-chip applications that manipulate micrometre-sized particles (Xie et al., 2019). Such applications include cell separation (Laurell et al., 2007), trapping (Hultström et al., 2007; Svennebring et al., 2009; Cai et al., 2020), cell sorting (Svennebring et al., 2009), compressibility analysis (Fu et al., 2021), and ultrasonic levitation (Jeger-Madiot et al., 2022) as in these cases  $\delta \sim a \ll \lambda$ . Settnes and Bruus developed their analytical expression based on the second-order perturbation theory of the Navier Stokes equations for the viscous boundary layer of the particle, neglecting acoustic streaming (second-order viscosity). They utilized the Gorkov's analysis (Gor'kov, 1962) for a compressible fluid far away from the particle and an incompressible fluid near the particle in the viscous boundary layer. They defined the acoustic contrast factor dependent on the viscosity of the fluid as well as on the density ratio of the particle and its surrounding fluid. Then, Karlsen and Bruus (Karlsen & Bruus, 2015) extended the previous work by considering both viscous and thermal effects on droplets and compressible particles.

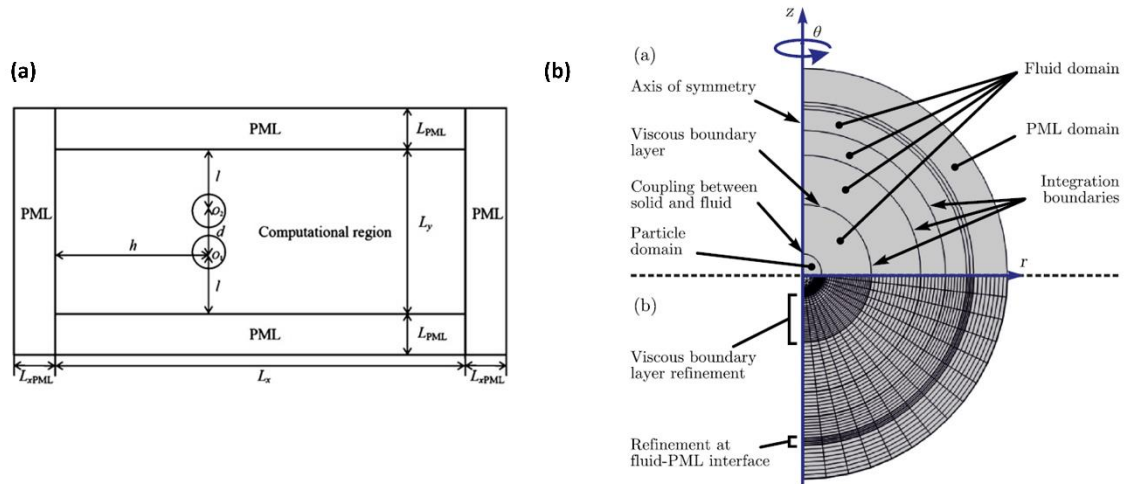


Fig 1.3. (a) Numerical simulations to find acoustic forces on rigid cylinders (Wang & Dual, 2009), (b) Finite-element modeling for calculation of acoustic forces on heavy compressible spheres (Baasch et al., 2019)

Muller et al. created a multi-step finite-element model for the acoustophoretic motion of spherical particles suspended in a microfluidic device subjected to ultrasonic waves. To determine the ARF, they first solved for first-order acoustic fields, then used the first-order field to compute the second-order fields. In order to compute the particles' paths, the evaluated forces were then applied to them (Muller et al., 2013).

Recently, Qiao et al. investigated the ARF analytically on a compressible sphere in a viscous fluid. They derived a general formula applicable to real applications in which compressible spherical particles are free to move in a viscous fluid; they confirmed their theoretical results experimentally. For a compressible sphere, their experiments and simulations showed that the ARF is dependent on incident sound pressure, acoustic wave frequency, and fluid viscosity (YupeiQiao et al., 2021). Moreover, many researchers have analyzed the ARF on rigid and compressible spheres exerted by different types of waves that have the potential for applications in various fields, including Bessel beam (Mitri, 2009), travelling waves (Johnson et al., 2016), and transient acoustic fields (Wang et al., 2021).

While the analytical solutions mentioned above are only relevant to basic shapes, there are two main categories of numerical solutions that can be used to determine the ARF on any shape. In the first method, the acoustic wave is introduced as a pressure wave in a domain of compressible fluid to resolve entire flow fields under acoustic waves through the complete solution of the Navier-Stokes equations. One related study, Wang & Dual, through a 2-D finite volume method-based (FVM) model, assessed the ARF and viscosity

effects for cylindrical objects (Wang & Dual, 2009). For various geometric parameters, their conclusions were in excellent agreement with their analytical computations. Their simulation for a basic structure like a cylinder took hours to complete since the forces were calculated from the total solution of compressible Navier-Stokes equations, in which viscous effects led to enhanced ARF compared to inviscid fluids. Also, Wang & Dual developed their numerical simulations to calculate the radiation force for rigid cylinders in slightly viscous fluids to study the effect of arbitrary wave types (Wang & Dual, 2011). Their results showed that the ARF is much greater than in plane travelling waves compared to plane stationary waves. Authors' analytical solution, which agreed with their FVM numerical solutions for ARF and ART, was derived based on shear stress.

In the second method of numerical solutions for viscous fluid, the perturbation approach is combined with Helmholtz equations derived from the first-order time-harmonic extension of Navier Stokes equations. This method greatly simplifies the solution procedure and dramatically lowers the processing cost. Muller et al. investigated ARF using such a numerical method in two steps. In the first step, first-order thermoacoustic equations were solved, and in the second step, the results from the first step were utilized as source terms for solving second-order equations, which led to computing the net ARF on the particles (Muller et al., 2012). The authors computed particle velocities numerically using the particle-tracking method. Their model depicted that acoustophoretic particle motion varied from being dominated by streaming-induced drag to being dominated by ARFs as a result of being a function of particle size, channel geometry, and material parameters. Later, the ARF on a spherical object was computed using a 2-D axisymmetric finite element method (FEM) model by Baasch et al. (Baasch et al., 2019). They evaluated first-order fields through a frequency domain study. Then, second-order fields were computed using the calculated first-order fields. Time-averaged ARF was obtained via these first- and second-order fields. They demonstrated that the ARF resulted predominantly from acoustic microstreaming when the viscous boundary layer thickness to particle radius ratio was sufficiently high, and the particle was adequately dense. Their results confirmed Doinikov's analysis (Doinikov, 1994), in which the second-order viscosity (microstreaming) contributed to moving heavy particles towards a pressure antinode in contrast to light particles that tend to move to pressure nodes.

As seen from the literature review, although many studies have focused on sphere particles in viscous fluids, only a few publications have been related to ARF on non-spherical particles in viscous fluids. Even though, similar to spherical particles, analysis of ARF on

non-spherical particles has received much theoretical interest. In one such study, Hahn et al. numerically simulated the arbitrary shape of rigid particles in a viscous fluid to calculate ARF and ART to predict particle motion (Hahn et al., 2015). They used a semi-analytical method alongside the numerical method to predict complex particle rotation and translation inside experimental micro-devices. In another numerical study, Pavlic et al. numerically examined the influence of particle shape and density on ARF and microstreaming (Pavlic et al., 2022). They considered a spherical particle with protruding crowns on its surface. Their findings showed a transition from viscous scattering to microstreaming dominance, which resulted from the density-dependency nature of ARF. In this study, as a deviation of the particle from a spherical shape approached the thickness of the viscous boundary layer, the impact of shape on viscous contributions to ARF decreased. The authors concluded that theoretical models for spherical particles could approximate ARF reasonably under such conditions. Moreover, they revealed that extremely asymmetric shape disturbances, like crowns with sharp edges, nevertheless resulted in noticeable viscous contributions for large dense particles of greater than viscous boundary layer thickness.

### **1.1.3. Secondary Forces**

Secondary ARFs among microparticles can be crucial in various applications, such as in the design of microfluidic devices for particle manipulation (Mohapatra et al., 2018), sorting (Gao et al., 2020), and separation (Gao et al., 2020; Vargas-Jiménez et al., 2021). In these applications, multiple particles are often present in the same region, and the interaction among particles can affect their behavior and movement. Secondary forces can either enhance or inhibit the primary radiation forces acting on each particle.

In microfluidic devices for cell sorting, ARFs can separate cells based on their size, density, and other physical properties. However, the presence of multiple cells in the same region can lead to the formation of clusters and unpredictable particle motion, which can interfere with the sorting process. A recent study (Gao et al., 2020) showed that secondary ARFs had a significant impact on behavior of particles in microfluidic devices. In this study, secondary forces helped break up particle clusters, which enhanced separation efficiency. They proposed several strategies to mitigate the effect of secondary ARFs, such as optimizing the channel geometry and introducing secondary acoustic waves to counteract the primary ARFs. Overall,

they highlighted the importance of considering the effect of secondary ARF in the design of microfluidic devices for particle manipulation and presented potential solutions to improve the performance and accuracy of these devices.

Secondary ARFs can also play a role in mixing and stirring fluids in microfluidic devices. By manipulating the secondary ARFs between microparticles, a group of particles can be manipulated, sorted or separated, which can have applications in areas such as drug delivery and chemical synthesis. Therefore, the significance of secondary ARFs among microparticles depends on the specific application and behavior of the particles involved. In cases where the presence of multiple particles can affect the efficiency or accuracy of the manipulation process, the investigation and control of secondary ARFs may be necessary. The secondary ARF has a great deal of importance in applications such as particle trapping (Ng et al., 2017), acoustic cavitation (Altay et al., 2020), acoustic coagulation (Li et al., 2014) and precipitation of aerosols and biomedical ultrasonics (Wang et al., 2018; Wu et al., 2019). Thus, predicting secondary ARF has become critical in developing new precise applications.

In the last decade, secondary ARFs have received considerable attention. Bjerknes' pioneering work on bubble-bubble interactions (Bjerknes, 1906) in an inviscid flow with an analytical expression for secondary ARF was followed by other studies on bubble interaction at both short inter-distances (Embleton, 1962; Zheng & Apfel, 1995; Doinikov & Zavtrak, 1996; Doinikov, 1996) and at long inter-distances (Zhuk, 1985; Doinikov, 1999; Doinikov, 2002). Crum (Crum, 1975) investigated the secondary ARFs between bubbles experimentally and theoretically, demonstrating that the secondary ARF between air bubbles was relatively small compared to the primary ARF, especially at bubble radii of less than 1 mm. Zheng and Apfel (Zheng & Apfel, 1995) derived an expression for the secondary ARF between two fluid particles. Doinikov and Zavtrak studied the secondary ARF between bubbles (Doinikov & Zavtrak, 1995) and bubble-rigid particles (Doinikov & Zavtrak, 1996) numerically and analytically using multiple expansions.

Also, at inter-distances comparable to a particle's size, the behavior of ARF between a gas bubble and a liquid droplet was studied (Doinikov, 1996). As the distance between the bubble and the droplet decreased, the interaction force increased in magnitude. It even changed its sign depending on the density ratio of the liquid to the surrounding fluid. Later, viscosity's effect on bubbles' interactions was studied in the literature (Doinikov, 1999; Doinikov, 2002). The separation distance between the bubbles was assumed to be significantly greater than their radii, and the surrounding medium was supposed to be an incompressible viscous liquid.

Bubble translational oscillations, the vorticity of the linear scattering field, and acoustic streaming were incorporated into a more precise formula for the contact force. It was demonstrated that viscous effects could lead micro-bubbles to repel one another across a reasonably wide parameter range.

The secondary ARF on rigid particles was studied by Embleton (Embleton, 1962) and Nyborg (Nyborg, 1989); they showed that repulsive secondary ARFs between rigid spheres decreased with increasing distance between the particles aligned in a wave direction. Mohapatra calculated the secondary ARFs for a pair of polystyrene particles within the Rayleigh limit and observed the same trend (Mohapatra et al., 2018). Sepehrirahnama proposed an analytical solution for both a single sphere and multiple spheres in viscous fluids subjected to an acoustic standing wave (Sepehrirahnama et al., 2015; Sepehrirahnama et al., 2016), in contrast to previous analytical solutions (Doinikov, 1994; Settnes & Bruus, 2012) that were limited to a single sphere. Silva and Bruus (Silva & Bruus, 2014) suggested a general analytical model for compressible particles with no restriction on the distance among the particles. Zhuk investigated the secondary ARFs between rigid spheres for various propagation directions of incident wave (Zhuk, 1985).

Few experimental studies have measured secondary ARFs (Yasui et al., 2008; Garcia-Sabaté et al., 2014). These studies showed that interacting with surrounding bubbles greatly influenced bubble pulsation under an ultrasonic horn. The interaction between bubbles significantly reduced the tendency of bubbles to expand during the ultrasound rarefaction phase.

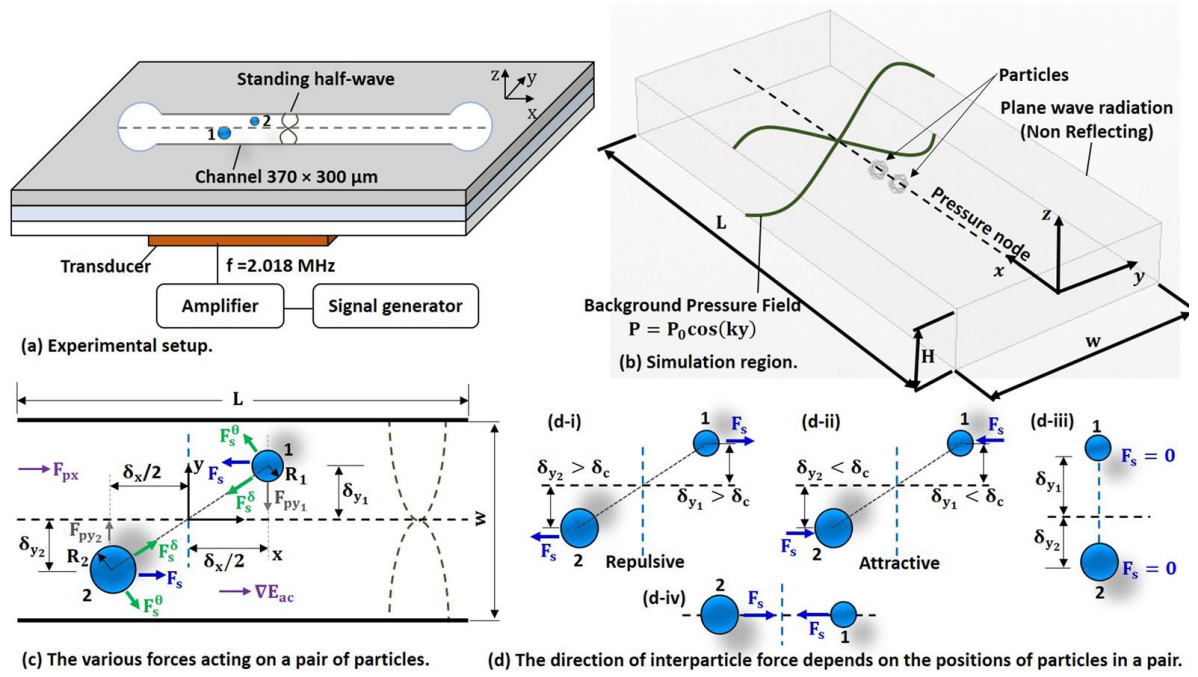


Fig 1.4. Finite-element modeling of secondary forces between spheres (Hoque & Sen, 2020)

Despite a wide range of studies utilizing analytical solutions for secondary ARF calculations, numerical methods are necessary to solve the problem without oversimplifying particle size, acoustic wavelength and fluid viscosity. The secondary ARF and ART between spheroidal particles were calculated using the boundary element method (BEM) in the literature (Wijaya et al., 2018). Their numerical findings demonstrated that, as in the case of two spheres, the secondary ARF predominated over the primary ARF when the spheroids were close to the pressure nodal plane. On the other hand, even when the spheroids were close to one another, the interparticle torque was negligible compared to the primary torque. These findings also offered a preliminary analysis of how biological cells, the majority of which are not spherical, agglomerate and arrange themselves close to the pressure node. Recently, Hoque et al. showed that secondary ARFs between spheres with different geometrical configurations depended on the distance between the particles relative to the direction of acoustic waves with experiments and numerical analysis using the FEM method, as shown in Fig 1.4 (Hoque & Sen, 2020). Another study compared two numerical approaches for calculating secondary ARFs on small spheres (Simon et al., 2019). Both of these approaches were based on the finite-element method: one of the methods utilized Gor'kov's potential approach (Gor'kov, 1962) in a 2D axisymmetric geometry, while the other used a tensor integral method for the evaluation of the force in 3D geometry. The evaluated results of both models matched the analytical approaches.

Fluid viscosity, another critical factor, was considered using an analytical approach by other authors (Sepehrihnama et al., 2016). These researchers observed that secondary ARF increased when the viscosity of the fluid was considered. However, they found it challenging to incorporate all the abovementioned factors using analytical approaches. Recently, the effect of microstreaming on the secondary ARF between elastic spherical particles was investigated numerically (Pavlic et al., 2022). It was illustrated that the microstreaming near the pressure node could result in attractive secondary ARF in the direction of the standing wave if one or both particles are smaller or comparable to  $\delta$ . Similar behavior was demonstrated when one of the particles' density was sufficiently greater than the density of the other particle.

## 1.2. Novelties of the Thesis

Despite widespread acoustophoresis applications, understanding the underlying physics behind ARF on non-spherical particles still needs to be completed, and further research is required to utilize its potential fully. Since particles in real life frequently have non-spherical shapes, a comprehensive study is needed to predict the motion of such objects. Acoustic radiation force (ARF) and torque (ART) on rings are complex phenomena that have not been studied in the literature. Different models are utilized to compute the relevant ARFs and ARTs in both inviscid and viscous fluids to fully understand the motion of flexible rods and loops such as rings subjected to acoustic waves. The present thesis aims to investigate the effect of different parameters, such as viscosity, geometry, and physical parameters, on the ARF and ART acting on rings and the secondary ARF that arise between rings. The novelty of this thesis lies in its comprehensive investigation of the ARFs and ARTs on rings. It provides insights into the behavior of shapes that are more complex than spheres and cylinders, which may have applications in fields such as cell manipulation, in which the cell's shape is often more complex than a simple sphere. In this dissertation, the influence of viscosity, including microstreaming, on ARFs and ARTs acting on rings in a standing wave is numerically analyzed.

In addition to viscosity, the geometry and the material of the ring, as a representative of elastic properties of the structure, is also a crucial parameter that affects ARF and ART. This thesis aims to investigate the effect of different ring geometries on ARF and ART, including minor and major radii and orientation. These results may have applications in the design of acoustic tweezers, where different geometries may be used to trap or manipulate particles of different sizes. Furthermore, the present thesis also considers the effect of physical parameters such as frequency, contrast factor, and phase of the acoustic wave on ARF and ART acting on rings. Investigating these parameters and their interaction with viscosity and geometry may provide a complete understanding of the behavior of acoustic forces and torques on rings. In another study, the ARF and ART results of the FEM method are compared with the computational chain-of-spheres approach on the rings with various materials. This method reduces the computational expense compared to the numerical methods of 3D structures, while the computational cost in the FEM method is a critical restriction. Then, self-scattering behavior between segments of the ring using the FEM method showed that self-scattering between the segments does not significantly affect local forces. In contrast, the elastic behavior of the entire

slender structure has a more significant effect.

Another novelty of this thesis is its focus on the interaction forces between rings. The influence of viscosity, microstreaming, and elasticity on secondary ARFs between rings are investigated. The results of this study may have applications in fields where the interaction between particles and their neighboring particles can affect the efficiency and accuracy of the manipulation process and control of multiple particles. Furthermore, this study contributes to a better understanding of the underlying physics of microstreaming, which is an essential factor in various applications such as mixing and stirring fluids. Overall, investigating the interaction forces between rings and their dependence on different parameters represents a significant and novel contribution to the field of acoustofluidic.

In summary, the novelty of this thesis lies in investigating the effect of viscosity, geometry, and physical parameters on primary and secondary ARF and ART on rings. By considering these parameters simultaneously, this thesis aims to provide a comprehensive understanding of the behavior of ARF and ART on complex shapes. It may have applications in various fields, such as cell manipulation, acoustic tweezers, particle separation, and composite reinforcement.

The findings of this thesis have resulted in several publications that are provided below:

- Malekabadi, F., H. O. Caldag and S. Yesilyurt (2023). "Acoustic radiation forces and torques on elastic micro rings in standing waves." Journal of Fluids and Structures 118: 103841.
- Malekabadi, F., H. Caldag, S. Yesilyurt, "Acoustic radiation forces and torques on compressible micro rings in standing waves. ", APS Division of Fluid Dynamics (DFD) Conference (November 2022), Phoenix, AZ
- Malekabadi, F., S. Yesilyurt, "Numerical Determination of Primary and Interparticle Acoustic Radiation Force Between a Pair of Rings in a Standing Wave, International Ultrasonics Symposium (IUS 2020), Las Vegas, Nevada

## 2. Methodology

This chapter briefly introduces the numerical methods used to simulate ARF and ART computations in viscous and inviscid fluids. The aim of this thesis is not to develop these computational techniques. However, instead, the methods are implemented to investigate the impact of various parameters on behavior of ring-shaped particles. Moreover, the governing equations used in the numerical methods are presented.

### 2.1. Governing equations

Generally, the conservation laws of mass, momentum, and energy can be used to generate the governing equations that describe fluid motion. However, in this thesis that thermal effects are not considered; the Navier–Stokes equations govern the fluid motion:

$$\rho \partial_t v = -\nabla p - \rho(v \cdot \nabla)v + \eta \nabla^2 v + \beta \eta \nabla(\nabla \cdot v) \quad (2-1)$$

and the continuity equation is:

$$\partial_t \rho = -\nabla \cdot (\rho v) \quad (2-2)$$

where  $v$  is the velocity field,  $\eta$ , and  $\beta$  are dynamic and bulk viscosity, respectively. The fluid density,  $\rho$ , is a function of only pressure  $p$ :

$$\rho = \rho(p) \quad (2-3)$$

#### 2.1.1. Perturbation Theory

The linearized compressible Navier-Stokes equations are utilized to calculate the ARF on small particles in fluids as it was used in the literature, e.g. (Glynne-Jones et al., 2013; Baasch et al., 2019). If thermal effects are disregarded, the density is only dependent on pressure,  $p$ . The perturbation method requires expanding the physical fields in series:

$$\rho = \rho_0 + \rho_1 + \rho_2 + \dots \quad (2-4)$$

$$p = p_0 + c_a^2 \rho_1 + p_2 + \dots \quad (2-5)$$

$$\mathbf{v} = \mathbf{0} + \mathbf{v}_1 + \mathbf{v}_2 + \dots \quad (2-6)$$

where  $\mathbf{v}$  is the velocity vector,  $c_a$  is the speed of sound inside the fluid,  $\rho$  and  $p$  are the fluid's density and pressure, respectively. The subscript 0 denotes the values in a quiescent fluid, so  $v_0 = 0$ . The subscripts in the terms denote the order of the terms. If all the fields inside the fluid are time-harmonic in the first order, the first-order fields can be written as follow:

$$\rho_1(r, t) = \rho_1(r) e^{-i\omega t} \quad (2-7)$$

$$p_1(r, t) = c_a^2 \rho_1(r) e^{-i\omega t} \quad (2-8)$$

$$\mathbf{v}_1(r, t) = \mathbf{v}_1 e^{-i\omega t} \quad (2-9)$$

where  $f$  is the frequency,  $t$  is the time, and  $\omega = 2\pi f$  is the angular velocity of the acoustic field; the acoustic wavelength is defined as  $\lambda = c_a/f$ .

### 2.1.1.1. First Order Perturbation Equations

First-order continuity and Navier Stokes equations are resulted from replacing the first-order perturbed fields in the governing equations of Eqs. (2-1) and (2-2) (Glynne-Jones et al., 2013):

$$\partial_t \rho_1 = -\rho_0 \nabla \cdot \mathbf{v}_1, \quad (2-10)$$

$$\rho_0 \partial_t \mathbf{v}_1 = -c_a^2 \nabla \rho_1 + \eta \nabla^2 \mathbf{v}_1 + \beta \eta \nabla (\nabla \cdot \mathbf{v}_1) \quad (2-11)$$

$$\rho_0 \partial_t \mathbf{v}_1 = -c_a^2 \nabla \rho_1, \text{ for an inviscid fluid } \mu, \beta = 0 \quad (2-12)$$

the time derivative is denoted by the subscript "t" in the expression.

### 2.1.1.2. Second Order Perturbation Equations

The time-averaged second-order continuity equations and Navier Stokes equations are obtained by replacing the second-order expansions in Eqs. (2-10) and (2-11),

$$\rho_0 \nabla \cdot \langle \mathbf{v}_2 \rangle = -\nabla \cdot \langle \rho_1 \mathbf{v}_1 \rangle \quad (2-13)$$

$$\eta \nabla^2 \mathbf{v}_2 + \beta \eta \nabla (\nabla \cdot \langle \mathbf{v}_2 \rangle) - \nabla \langle p_2 \rangle = \langle \rho_1 \partial_t \mathbf{v}_1 \rangle + \rho_0 \langle (\mathbf{v}_1 \cdot \nabla) \mathbf{v}_1 \rangle \quad (2-14)$$

$$-\nabla \langle p_2 \rangle = \langle \rho_1 \partial_t \mathbf{v}_1 \rangle + \rho_0 \langle (\mathbf{v}_1 \cdot \nabla) \mathbf{v}_1 \rangle, \quad \text{for an inviscid fluid } \mu, \beta = 0 \quad (2-15)$$

" $\langle \rangle$ " shows the time average over a full period,  $\tau$ , described as

$$\langle X \rangle = \frac{1}{\tau} \int_0^{\tau} dt X(t)$$

### 2.1.2. Deformation of Solid Particles

Newton's second law provides the equilibrium equations for solid mechanics stating the balance between forces and changes in motion (linking the body forces and stresses). Stresses and strains vary throughout a material relating to displacement through Hook's law. Typically, Hooke's law for linear elasticity is expressed as follows:

$$\sigma = C : \varepsilon \quad (2-16)$$

The constitutive tensor  $C$  is a fourth-order tensor in this case, while the stress,  $\sigma$ , and strain tensors,  $\varepsilon$  are second-order tensors. A contraction spanning two indices is indicated by the character ":". The same equation can be written as follows in a notation where the indices are displayed:

$$\sigma_{ij} = C_{ijkl} \varepsilon_{kl} \quad (2-17)$$

Using Einstein summation convention

$$\sigma_{ij} = \sum_{k=1}^3 \sum_{l=1}^3 C_{ijkl} \varepsilon_{kl} \quad (2-18)$$

Typically, motion's equation is expressed in terms of the Cauchy stress tensor as follows:

$$\rho_p \frac{\partial^2 u}{\partial t^2} = \nabla \cdot \sigma + F_v \quad (2-19)$$

where  $F_v$  is a body force per unit deformed volume, and  $\rho_p$  is the density of the solid material.

### 2.1.3. Boundary and Coupling Conditions

In acoustics, the specific acoustic impedance of a material ( $Z = \rho c$ ), represented by the subscripts 1 and 2, defines the conditions at a planar interface between materials 1 and 2. By using the reflection ( $R_{12}$ ) and transmission ( $T_{12}$ ) coefficients for the pressure (Lenshof et al., 2012).

$$R_{12} = \frac{Z_2 - Z_1}{Z_2 + Z_1} \quad \text{and} \quad T_{12} = 1 - R_{12} \quad (2-20)$$

respectively, which are held for an incident plane wave originating from material 1 and moving in a direction normal to their interface.  $R_{12}$  and  $T_{12}$  can provide information on the kind of boundary condition that could be used to replace one of the material domains in the modelling; To explain further, for  $R_{12} \approx -1$  at the water-air interface, the acoustically-soft-wall boundary condition can take the place of the air domain, which implies  $p_1 = 0$  on the water at the interface; On the other hand, for  $R_{12} \approx 1$ , where the water domain is being substituted, the acoustically-hard-wall boundary condition is applied to the air at water-air interface ( $n \cdot v_1 = 0$  enforced on the air, which  $n$  is a unit vector normal to the interface).

The acoustically-hard-wall boundary condition for viscous fluids corresponds to the no-slip boundary condition, further restricting the velocity component tangential to the interface. Additionally, the no-slip boundary condition is applicable when the system is being constrained through velocity by equating the fluid's velocity to the interface's velocity at the interface.

Moreover, when two materials are modeled, coupling conditions must be applied at the interface. Typically to couple a viscous fluid and a compressible solid, continuity of velocity and stresses are assumed at the interface (Doinikov et al., 2017). Similarly, to couple an inviscid fluid and a compressible solid, normal velocity and normal stress components must be matched, and the tangential component of the shear stress in the solid must disappear at the interface (Jr., 1951).

## 2.2. Acoustic Radiation Forces on a Ring

A physical phenomenon known as acoustic radiation force (ARF) occurs when an acoustic wave interacts with an obstruction in its path, disturbing the pressure and momentum transfer. Acoustic Radiation Force (ARF) consists of two kinds of forces: primary and secondary forces. Primary forces arise when a single particle presents in an acoustic field and directs the particles away from the sound source. Secondary forces result from additional scattering from the multiple particles in the acoustic field that will cause attraction/repulsion between particles.

### 2.2.1. Primary Acoustic Radiation Forces

The pressure field on an object's surface is used to compute the force of acoustic radiation acting on it. The pressure field is evaluated by solving Helmholtz equations. The equation for a one-dimensional wave is:

$$\frac{\partial^2 p}{\partial z^2} - \frac{1}{c_0^2} \frac{\partial^2 p}{\partial t^2} = 0 \quad (2-21)$$

where  $c_0$  is the sound's velocity in the fluid,  $t$  represents time,  $z$  is the component of the Cartesian coordinate system, and  $p$  is the acoustic pressure. The solution to the given equation is:

$$p = p_a \sin(\omega t \pm kz) \quad (2-22)$$

in which the pressure wave's amplitude,  $p_a$ , the wave number is  $k = \frac{2\pi}{\lambda}$ , and the angular frequency is  $\omega = 2\pi f$ . A tiny object will disturb this acoustic field, and the overall pressure will have a background and scattered components:

$$p = p_b + p_{sc} \quad (2-23)$$

Many authors have preferred the perturbation theory for calculating the acoustic radiation force due to its efficiency and accuracy (Glynne-Jones et al., 2013; Garbin et al., 2015; Baasch et al., 2019).

#### 2.2.1.1. In a viscous fluid

The time-averaged acoustic radiation force can be calculated by an integration over the particle surface  $S(t)$ :

$$F_i = \left\langle \int_{S(t)} \sigma_{ij} \cdot n_j dS \right\rangle \quad (2-24)$$

where  $\sigma_{ij}$  is the stress tensor for  $i = 1, 2, 3$  and  $j = 1, 2, 3$ ,  $n_j$  is  $j$ -th component of the surface's outward normal vector and  $\langle \dots \rangle$  shows the time average over a total period, and repeated

indices imply summation. For a viscous fluid, by integrating over a fixed surface surrounding particle, one can get the time-averaged acoustic radiation force up to second order (Doinikov, 1994):

$$F^{rad} = \int_{S_0} \langle \sigma_2 - \rho_0(v_1 v_1) \cdot \mathbf{n} \rangle dS \quad (2-25)$$

The subscript of  $\sigma$  is not to be confused with the double-digit notation at Eq. (2-17), where the subscript indicates the order:

$$\sigma_2 = p_2 I + \eta(\nabla v_2 + (\nabla v_2)^T) \quad (2-26)$$

### 2.2.1.2. In an inviscid fluid

For an inviscid flow, the viscosity is set to zero, so the second-order stress tensor is obtained as (Bruus, 2012):

$$\langle \sigma_2 \rangle = -\langle p_2 \rangle I = -\left( \frac{1}{2\rho_0 c_0^2} \langle p_1^2 \rangle - \frac{\rho_0}{2} \langle |v_1|^2 \rangle \right) I \quad (2-27)$$

The simplified time-averaged acoustic radiation force can be written as:

$$F^{rad} = - \int_{S_0} \{ \langle p_2 + \rho_0(v_1 v_1) \cdot \mathbf{n} \rangle \} dS \quad (2-28)$$

where  $\mathbf{n}$  is the outward normal vector of the surface. Whenever two vectors are next to one another, as  $\langle v_1 v_1 \rangle$  are in Eq. (2-15), the tensor product is implied, and below is the formula for the time-averaged second-order acoustic pressure:

$$\langle p_2 \rangle = \left( \frac{1}{2\rho_0 c_0^2} \langle p_1^2 \rangle - \frac{\rho_0}{2} \langle |v_1|^2 \rangle \right) \quad (2-29)$$

## 2.3. Acoustic Radiation Torques on a Ring

Time-averaged acoustic radiation torque can be computed from the following formulae:

$$\boldsymbol{\tau}^{rad} = - \int_{S_0} (\mathbf{r} - \mathbf{r}_0) \times F^{rad} dS \quad (2-30)$$

where  $\mathbf{r}$  represents the location of a point on surface  $S_0$  and  $\mathbf{r}_0$  represents ring's center-of-

mass.

### 2.3.1. Secondary Radiation Forces on a Ring

When  $F^{rad}$  is written without a subscript, it should be inferred that the force is in the propagation direction of the acoustic wave and it is for a single ring only, primary force. The secondary radiation force is calculated with a set of two computations for each case. First, a single ring is placed in the domain to obtain the primary radiation force,  $F_p^{rad}$ . Second, the second ring is placed in the domain, which allows us to calculate the total radiation force,  $F_t^{rad}$ . The secondary radiation force  $F_s^{rad}$  is the difference between the total and primary forces:

$$F_s^{rad} = F_t^{rad} - F_p^{rad} \quad (2-31)$$

where  $F_t^{rad}$  and  $F_p^{rad}$  are obtained from Eqs. (2-25) and (2-28) for the viscous and inviscid fluid, respectively. In this study, secondary radiation forces in the z-direction are investigated.

## 2.4. Finite Element Method Simulations

The primary and secondary radiation forces on rings are analyzed using (FEM) model built in the commercial finite-element software COMSOL Multiphysics to solve the governing equations numerically to obtain acoustic radiation forces and torques with the given formulas in the previous section.

### 2.4.1. For an Inviscid Fluid

Calculating ARFs and ARTs over rings or torus analytically is quite challenging in-plane acoustic fields, especially when the ring is inclined relative to the plane of propagation. Therefore, the finite-element method is employed, which can accurately describe intricate three-dimensional structures like rings and is reliable when applied to linear problems. An elastic ring with a major radius  $R$  and a minor radius  $a$  is positioned in a fluid domain while

being rotated by an angle  $\theta$  around the  $y$ -axis, schematically shown in Fig 2.1. Using the COMSOL Multiphysics program, a three-dimensional finite-element model of the ring is created. We employed time-harmonic formulas in the frequency domain for the pressure amplitude in the fluid and the displacement amplitude in the elastic solid under the assumption of a planar background pressure field in the  $z$ -direction that depicts standing waves. Time-averaged forces (ARFs) and torques (ARTs) can be calculated from Eqs. (2-28) and (2-30) when  $S_0$  is ring surface. To provide a standing acoustic field without any reflections, planar non-reflection radiation boundary conditions (NRBC) are utilized (COMSOL; Givoli & Neta, 2003). Because comparisons between NRBC and PML conditions reveal insignificant differences, planar NRBC is recommended over perfectly matched layers (PML) for computational efficiency. Furthermore, the domain size is significantly larger than the ring size to maintain optimal acoustic field resolution by keeping the boundaries away from the ring. The spherical and cylindrical fluid domains were compared to the cubic fluid domain, but no discernible differences were found.

The physical and geometric parameters utilized in the simulations are listed in Tables 2.1 and 2.2. To investigate the effect of rigidity on the ARFs and ARTs, polystyrene, copper, and aluminum rings are simulated as a solid domain in a fluid domain made up of water. The primary and secondary speeds of sound,  $c_p$  and  $c_s$ , are applied in the equations of linear elasticity to define the solid particles (Graff, 2012).

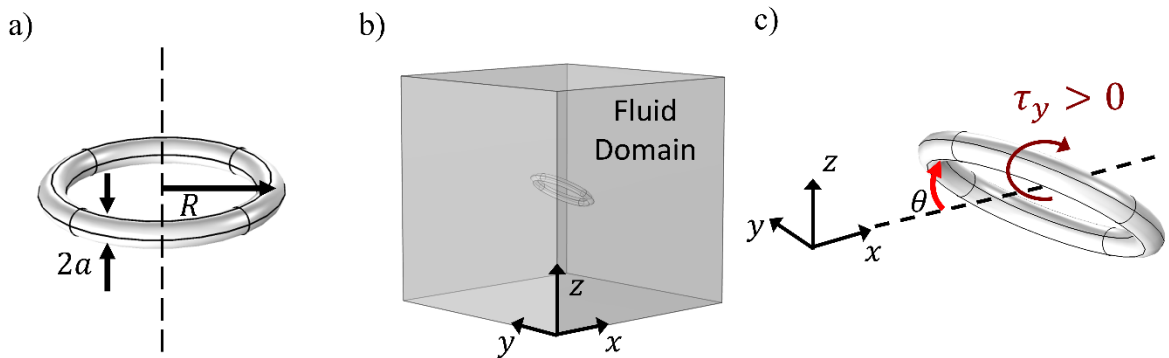


Fig 2.1. (a) Geometric parameters of the ring. (b) Ring is positioned inside a fluidic domain with radiation conditions at the boundaries in the simulation domain. (c) Ring rotation angle depiction,  $\theta$ .

Table 2.1. Fluid properties and geometric parameters for the reference ring.

Parameter	Symbol	Value	Units
Fluid density	$\rho_f$	998.2	$\text{Kgm}^{-3}$
Fluid compressibility	$\kappa_f$	$4.76 \times 10^{-10}$	$\text{Pa}^{-1}$
Fluid speed of sound	$c_a$	1482	$\text{ms}^{-1}$
Pressure amplitude	$p_a$	100	kPa
Minor Radius	$a$	3	$\mu\text{m}$
Major Radius	$R$	25	$\mu\text{m}$

Table 2.2. Solid properties of materials and the geometric parameters for the reference ring.

Parameter	Symbol	Polystyrene	Copper	Aluminum	Units
Particle density	$\rho_p$	1050	8930	2700	$\text{Kgm}^{-3}$
Particle compressibility	$\kappa_p$	4.25e-10	8.26e-12	1.42e-11	$\text{Pa}^{-1}$
Longitudinal velocity	$c_p$	2400	5010	6420	$\text{ms}^{-1}$
Shear velocity	$c_s$	1150	2270	3040	$\text{ms}^{-1}$

The pressure acoustics module is coupled with the solid mechanics' module in COMSOL, and a non-reflecting boundary condition (NRBC) is implemented to absorb the outgoing waves. Background pressure leads to the acoustic field, which is imposed as a standing wave and is defined as follows:

$$p_b = p_a \cos(k(z - \Delta z)) \quad (2-32)$$

where  $z$  is the axial position with respect to the direction of wave propagation,  $k$  is the acoustic wavenumber, and  $k\Delta z$  is the phase angle. Using acoustic-structure Multiphysics in COMSOL, the fluid domain is coupled with the solid domain by applying pressure from the fluid domain as boundary load onto the solid and acceleration from the solid domain as boundary acceleration onto the fluid at the solid-fluid interface.

#### 2.4.2. For a Viscous Fluid

To solve the problem numerically in COMSOL, we used the following approach for the viscous model:

The pre-defined interface of thermoacoustic physics coupled with solid mechanics physics through the thermoviscous acoustic-solid interaction interface is used to calculate the first-order acoustic fields of Eqs. (2-10), and (2-11) a perfectly matched layer (PML) is applied to truncate the computational domain and ensure that the wave is not reflected back from the domain boundaries, as shown in Fig 2.2. The acoustic field is imposed directly in thermoviscous acoustic interface as a standing pressure field via background pressure and velocity, defined as:

$$p_b = p_a \cos(k(z - dz)) \quad (2-33)$$

$$v_b = ik\varphi_a \sin(k(z - dz)) \quad (2-34)$$

where  $z$  is the axial position along the wave propagation direction and  $dz$  is the phase.  $k$  is the acoustic wavenumber and  $\varphi_a$  is the potential amplitude:

$$\varphi_a = -\frac{p_a}{i\omega\rho_0 + \left(\eta_B + \frac{4}{3}\eta\right)k^2} \quad (2-35)$$

$p_a$  is the pressure amplitude, and  $k$ , viscous wavenumber is defined as (Doinikov, 1994):

$$k = \left( \frac{1 - i\omega\left(\eta_B + \frac{4}{3}\eta\right)}{\rho_0 c_0^2} \right)^{-\frac{1}{2c_0}\omega} \quad (2-36)$$

The thermoviscous acoustics interface is switched into the adiabatic mode. This will simplify the governing equation to the viscous problem (otherwise, it is thermoviscous, including the

energy equation, etc.). Thermoviscous acoustics interface should use at least quadratic Lagrange elements for pressure and cubic Lagrange elements for velocity (temperature is not solved for, as we use adiabatic formulation, so it does not matter). The order should always be one higher for velocity to ensure numerical stability based on the information from COMSOL. Further, heat capacity is set to 0 and the ratio of specific heats to 1 in the thermoviscous acoustics interface settings. The continuity of velocity and stress are imposed at the fluid-solid interfaces. In an unlimited fluid, the first-order fields are assumed to converge to background fields far from the particle. With frequency domain study, the first-order acoustic problem is solved in the frequency domain.

Then, the laminar flow interface is implemented onto the fluid domain, excluding the particle and PML domain, to calculate the time-averaged second-order fields by modifying its governing equations by adding the right-hand side of Eq. (2-14) as volume forces to the domain and imposing the following boundary condition at the no-slip fluid-structure interface through wall boundary condition:

$$\langle v_2 \rangle = - \left\langle \left( \int v_1 dt \cdot \nabla \right) v_1 \right\rangle \quad (2-37)$$

where the negative Stokes drift velocity on the right-hand side of Eq. (2-37) compensates for the first-order oscillations at the interface. Using the pressure point constraint, the streaming problem is limited by setting the second-order pressure field to a fixed value at any point in the fluid domain. To improve the discretization in the Creeping flow interface, P3+P2 discretization is set to the entire domain; cubic discretization for the velocity to capture the streaming phenomenon in the viscous boundary layer and quadratic discretization for the pressure. The acoustic radiation forces are determined using Eq. (2-25) with the first-order fields from the thermoviscous acoustic interface and the second-order stress tensor from the creeping flow.

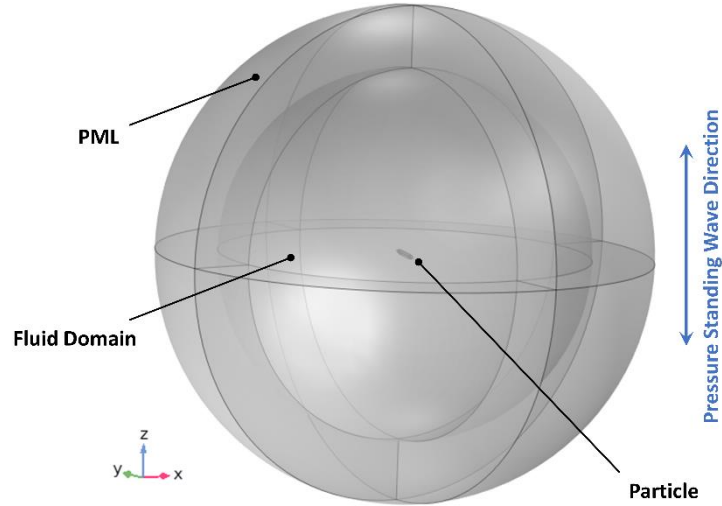


Fig 2.2. Viscous Simulation domain with the ring placed inside a fluidic domain with PML, nonreflecting radiation conditions at the boundaries.

### 2.4.3. For a Pair of Particles

Primary and secondary radiation forces between a pair of equal and unequal-sized rings are analyzed as shown in Fig 2.3 using a 2-dimensional, axisymmetric finite-element method (FEM) model built in COMSOL Multiphysics (Check Fig 2.3 for the representation of the 3-dimensional geometry in 2-dimensional axisymmetric configuration). In the arrangement shown in Fig 2.1a-c, the rings are axially placed in the direction of propagation of the standing acoustic wave at the same radial position. The second ring is placed away from the pressure node in a symmetric fashion with respect to  $z = 0$ , separated by a total distance of  $d$  from the first ring positioned at the pressure node, as shown in Fig 2.3;  $d$  is defined as the surface-to-surface distance between the particles. The major radius is identified with  $R$ , and  $a$  subscript is added to identify the ring in reference, as shown in Fig 2.3c.

The secondary acoustic radiation forces are determined using Eq. (2-31) with primary and total forces computed from Eq.(2-25 and 2-28) corresponding to viscous and inviscid fluids, respectively. Secondary forces arose from the re-scattered waves (Silva & Bruus, 2014) and interactions between the two particles' acoustic microstreaming fields (Sepehrihahnama et al., 2016). The FEM model is built based on the description in section 2.3.1. For any parameter set, computing the secondary forces for the two particles necessitates three simulations: one

simulation containing both particles and two single-particle simulations, one for each of the two particles. Axial symmetry can be used with the problem's definition, reducing computing expenses.

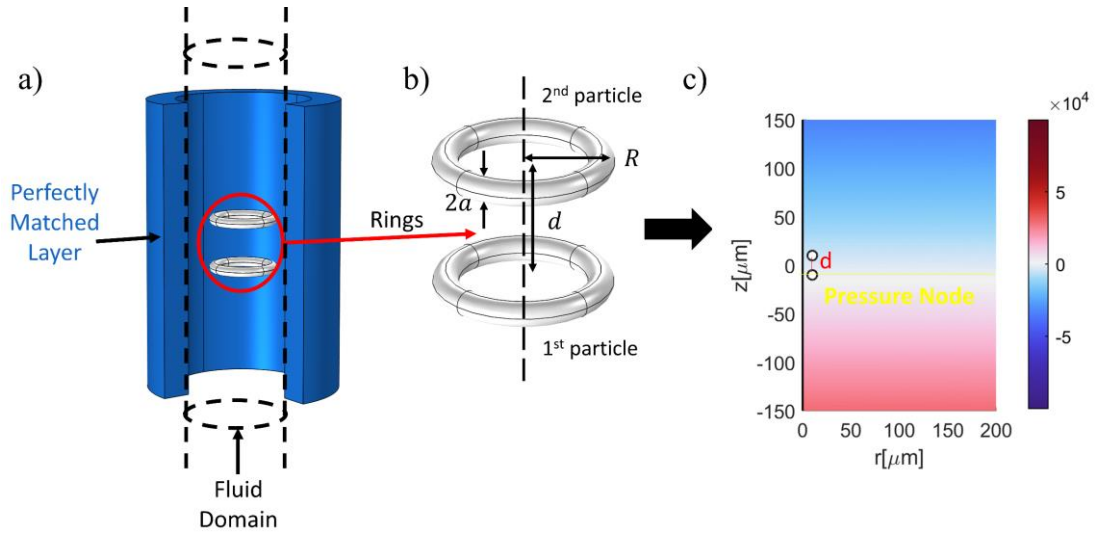


Fig 2.3. Depiction of simulated geometries. (a)-(c) show the configuration where the rings are placed along the propagation axis of the acoustic field and. (a) depict the 3-dimensional geometry, (b) show the arrangement of the rings alongside the geometric parameters and (c) show the 2-dimensional, axisymmetric domains simulated with the standing acoustic field. Note that the ring or domain dimensions are not to the scale.

## 2.4.4. Mesh Convergence

### 2.4.4.1. For an Inviscid Model

To investigate mesh convergence behavior of the FEM model, ARFs are determined over a polystyrene ring using Eq. (2-25) with implementing first- and second-order velocity and pressure fields. With using  $f = 6 \text{ MHz}$ , the lowest wavelength is obtained, resulting in the most restrictive study in terms of mesh element sizes.

Table 2.3. Geometric parameters of the ring used for the convergence studies of the 3D FEM model.

Parameter	Value
Minor Radius	$3 \mu\text{m}$
Major Radius	$25 \mu\text{m}$
Rotation Angle	$0^\circ$
Frequency	6 MHz

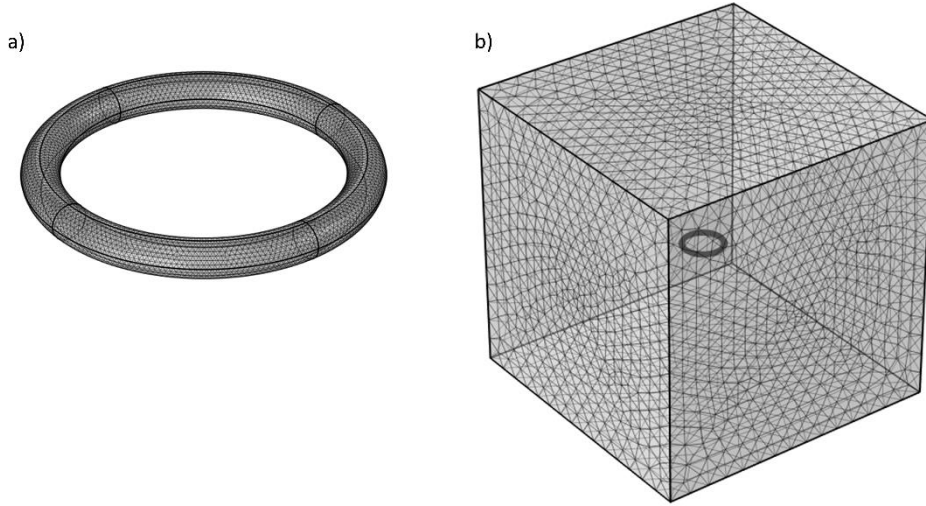


Fig 2.4. Mesh on a) a ring particle, b) fluid domain.

Figs 2.4a and 2.4b depict the ring geometry and the simulation setup, respectively. While a free tetrahedral mesh is preferred for the fluid domain, the swimmer surface has meshed with free triangular components. Tables 2.1 and 2.2 list the characteristics of the materials used in the thesis. Table 2.3 shows the geometric parameters used in the mesh convergence studies. Although the model has been refined to the point where the solver needs more than 300 GB of RAM, the initial testing with the ring model produced non-converging results.

Further analysis revealed that the ring's and the domain's meshing should differ significantly: Although the elements on the ring should be as small as a few microns for an acoustic frequency of 2 MHz, yielding an element size to ratio close to  $1/600$ , the model is insensitive to meshing in the fluid domain beyond the element size of  $\lambda/5$ . For the geometry with the parameters given in Table 2.3, the convergence is reached at roughly 1.2 million degrees of freedom (DOF), according to the convergence curve supplied in Fig 2.5. Thus, calculated force values are more sensitive to mesh density on the surface of the ring than the mesh in the fluid domain away from the ring.

Regarding computed forces in the z-direction acquired from the finest mesh, a relative convergence error  $e$  is computed:

$$e = \left| \frac{F^{rad} - F^{rad,finest}}{F^{rad,finest}} \right| \quad (2-38)$$

The results of the convergence investigation for a polystyrene ring in water are shown in Fig

2.5. The relative error is less than 2% for  $\delta = 0.002\lambda$ , corresponding to  $1.25 \times 10^6$  degrees of freedom and is used for the remaining simulations given here.

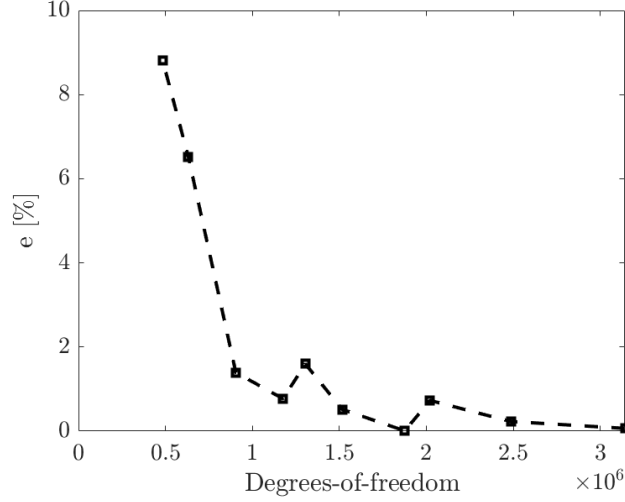


Fig 2.5. Convergence of  $F^{rad}$  with respect to the degrees of freedom.

#### 2.4.4.2. For a Viscous Model

A mesh convergence study is performed on the FEM model to ensure the accuracy of the calculations. The fluid and solid domains are meshed using triangular elements of quadratic order for pressure and cubic for velocity for a proper resolution. To improve the resolution of high-velocity gradients, a denser mesh is used inside the viscous boundary layer domain near the rings. The element size of the mesh is set to a fixed value,  $h$ , within the viscous boundary layer, and a maximum element size of  $10h$  is applied to the fluid domain. The acoustic radiation force in the  $z$ -direction ( $F^{rad}$ ) is depicted in Fig 2.6 for decreasing mesh element size,  $\delta/h$  where  $\delta$  is the thickness of the viscous boundary layer. A relative convergence error is calculated with respect to the result from the finest meshing as follows:

$$\text{Relative Error} = \left| \frac{F^{rad} - F^{rad,finest}}{F^{rad,finest}} \right| \quad (2-39)$$

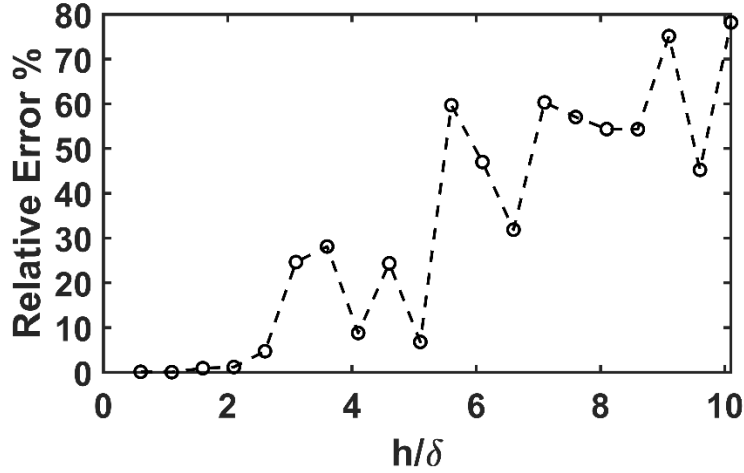


Fig 2.6. Mesh convergence studies with respect to the maximum element size.

As presented in Fig. 2.6, the results become insensitive to the meshing when  $h/\delta < 2.1\delta$  (Relative error is less than 1% for smaller  $h/\delta$ ). Thus, we use a mesh with the maximum element size of  $h = 2.2\delta$  for the rest of the paper.

#### 2.4.5. Validation and Verification of the Model

While no prior work has studied radiation forces on rings, the force values are compared on structures published in the literature to validate the model. The following three comparisons are made: In the first comparison, the radiation force on a ring and cylinder are compared following section 2.4.1 for the inviscid fluid case. In the second comparison, the acoustic radiation force on a sphere is compared with the findings in the literature for the viscous fluid model based on the model described in section 2.4.2. The third comparison is with the data from the literature on the two spheres' secondary force, based on the method in section 2.4.3.

Initially, a  $6 \mu m$  diameter polystyrene sphere is placed in a standing acoustic field with  $p_a = 100 kPa$  and  $f = 2 MHz$ . Compared to our 3-dimensional model, which calculates a radiation force of  $0.569 pN$ , Hasegawa's model (Hasegawa, 1979) yields a value of  $0.576 pN$ . The FEM model and the Hasegawa (Hasegawa, 1979) model's relative percentile error is 1.21, which indicates high accuracy.

Table 2.4. Comparison of 3-dimensional FEM model results with the literature

Evaluated Term	$F^{rad}$
FEM Model	0.569 pN
Hasegawa Analytical	0.567pN

The model is then validated by comparing the ARFs for a copper cylinder with an equivalent length and cross-section to the ring when  $a = 1 \mu\text{m}$ . Tables 2.1 and 2.2 list the remaining geometric and physical parameters employed in the simulations. The magnitude of the ARF computed on both particles using Eq. (2-28) is compared in Fig. 2.7a. In the most tested cases, the ARFs match and only start to diverge somewhat at large  $a$ , corresponding to a ring that is less resemblant than a cylinder as  $a \rightarrow R$ .

Secondly, to validate the viscous model,  $F^{rad}$  is calculated for a copper sphere with a radius of  $1 \mu\text{m}$  positioned at  $\lambda/8$  from the pressure node (between the pressure node and the antinode) in water. The agreement of the proposed FEM model in section 2.4.2, referred to as ‘‘FEM,’’ and Doinikov’s model (Doinikov, 1994) is shown in Fig 2.7b. Doinikov’s theory considers the first and second-order viscous effects as microstreaming around the sphere in the viscous fluid, and our numerical results support the second-order viscous theory of Doinikov (Doinikov, 1994).

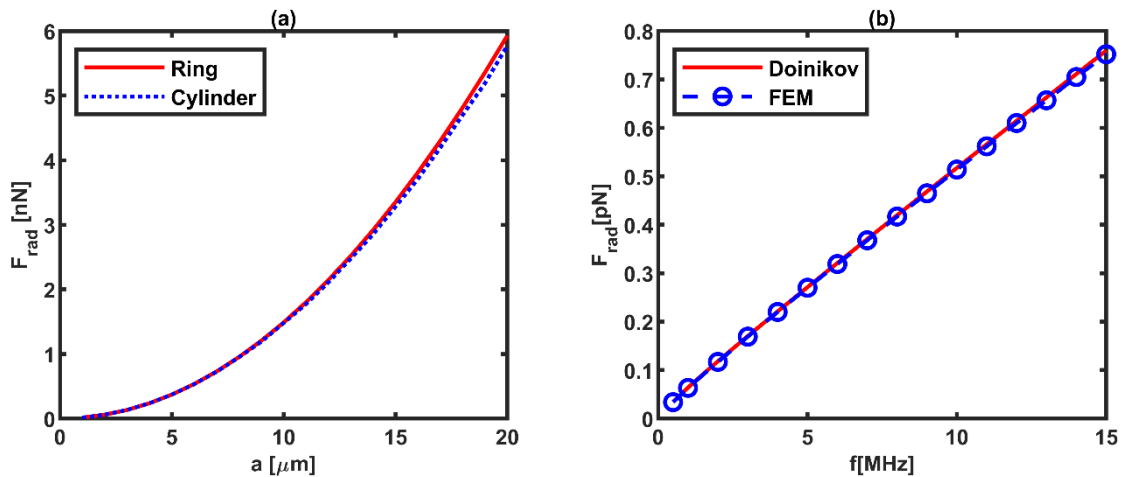


Fig 2.7. a) comparison of our numerical model for a ring and cylinder in water b) ARF versus frequency for a sphere in water compared with analytical results considering viscosity effects.

Lastly, the secondary force versus the dimensionless center-to-center distance between spheres ( $kd_v$ ) in an inviscid flow for a pair of particles with different sizes is compared with Hoque and Sen's results (Hoque & Sen, 2020), as shown in Fig 2.8. The model parameters are as the reference parameters (Hoque & Sen, 2020). The results are in good agreement for most cases, and the difference can be tracked back to the different mesh sizes and quality at low  $kd_v$ .

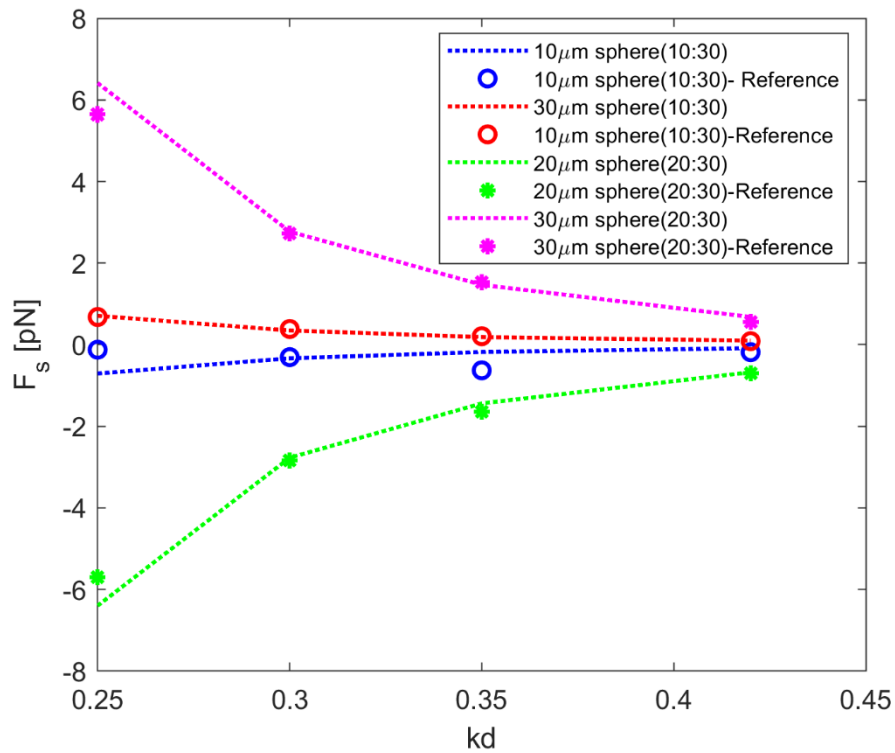


Fig 2.8. The comparison of the secondary forces between spheres (sphere1: sphere2). Dashed lines are the simulation results, datapoints are from Hoque and Sen (Hoque & Sen, 2020).

### 3. Acoustic Radiation Forces and Torques on a Ring

This chapter reports the effects of ring geometrical parameters, including ring major and minor radii, orientation, and its position in a standing wave, on the acoustic radiation force (ARF) and torque (ART) in a standing wave. Besides, the influence of the physical parameters such as frequency, density, and viscosity on the ARFs and ARTs acting on the ring are investigated. Unless otherwise stated, all results presented here use geometric and physical parameters from Tables 2.1 and 2.2.

All the results are provided in dimensional terms in accordance with studies in the literature (Glynn-Jones et al., 2013; Garbin et al., 2015; Baasch et al., 2019). However, Appendix A provides a thorough dimensional analysis of the ARFs and ARTs on a ring using analytical solutions for spheres. This study helps clarify the influences of the ring's orientation, position, and geometric features.

#### 3.1. Effects of the Ring's Placement

First, the effects of the position of the ring relative to the pressure field on the ARF and ART are studied. For a horizontal ( $\theta = 0^\circ$ ) and rotated ( $\theta = 30^\circ$ ) polystyrene ring, the corresponding  $F^{rad}$  profiles are depicted in Fig 3.1c, while the pressure nodes and values with respect to  $\Delta z$  are given in Fig 3.1a and Fig 3.1b. ARF depicts a sinusoidal trend regarding the ring position in the standing wave. As demonstrated in Appendix A, the dependence of  $F^{rad}$  on the position follows a sine profile. Additionally, the influence of orientation is insignificant on the ARF as deviations of ARF on a rotated ring from a ring that is not rotated ( $\theta = 0^\circ$ ) are negligible since  $R/\lambda = 0.0337 \ll 1$ . As shown in Fig 3.1c, rings that experience positive ARF close to multiples of  $\Delta z = \lambda/4$ , pressure nodes, are pushed to those nodes. Both pressure nodes and antinodes are equilibrium position for the ring, however only pressure nodes are stable positions as  $F^{rad} < 0$  for  $\Delta z > \lambda/4$  and vice versa.

As shown in Fig 3.1a, the maximum ARF is observed at a distance of  $\lambda/8$  from the pressure

node,  $\Delta z = \lambda/8$ . The torque values on the ring in Fig 3.1d shows zero torque at  $\theta = 0^\circ$  and a negative (restorative) torque for all  $\Delta z$  values at  $\theta = 30^\circ$ . Appendix A (Eq. A8) demonstrates that the tilted ring with  $\theta = 30^\circ$  has a cosine dependence regarding position. With the maximum happening at  $\Delta z = \lambda/4$  for ART, the force and torque profiles are out of phase.

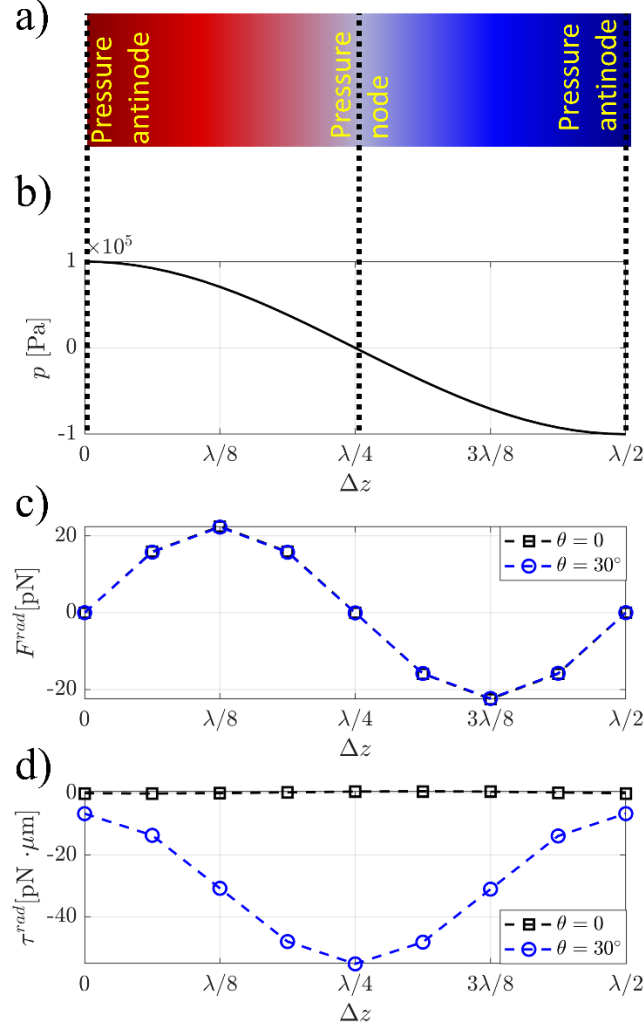


Fig 3.1. The radiation force and torque with respect to  $\Delta z$  in a standing wave on a horizontal ( $\theta = 0^\circ$ ) and tilted ( $\theta = 30^\circ$ ) polystyrene ring in water for a  $f = 2$  MHz. a) Color plot of the pressure amplitude, b) Change of  $p$  with respect to  $\Delta z$  and the corresponding c)  $F^{rad}$  and d)  $\tau^{rad}$  profiles.

Further, the work is extended to consider the viscosity, including the first and second order. The simulated model solves for a viscous fluid that includes microstreaming, which is a second-order viscous effect resulting from the presence of the particle in the acoustic field in the form of steady vortices around the particle. Thermal effects are disregarded following earlier publications (Doinikov, 1994; Doinikov, 1994; Settles & Bruus, 2012); thus, the compressible Navier–Stokes equations and the continuity equation govern the motion of the

viscous fluid and energy equations are not solved.

In this model, the ARF is analyzed concerning the particle's position in the acoustic wave with  $f = 2\text{MHz}$  for a horizontal ring and a tilted ring with  $\theta = 30^\circ$ . As can be seen in Fig 3.2, similar to inviscid fluids, rotated ring experiences slightly different acoustic radiation force than a non-rotated ring and viscosity does not affect the behavior of the acoustic radiation force with changing the position of the particle.

Moreover, as Fig 3.2 shows, the ring in a viscous fluid experiences restorative torque trying to align the ring toward  $\theta = 0$ . At  $\Delta z = \frac{\lambda}{4}$ , the pressure node, maximum torques occur where ARFs are zero, and the torque is zero at pressure antinodes, similar to the inviscid fluid. The results are also analogue to disk-shaped particles in the literature (Garbin et al., 2015). The torque is maximum in positions with the greatest fluid velocity, and in positions with zero fluid velocity, there is zero torque. According to Eqs. (2-33) and (2-34), pressure antinodes are velocity nodes with zero fluid velocity and consequently zero torque, whereas pressure nodes correspond to velocity antinodes that induce maximal torque.

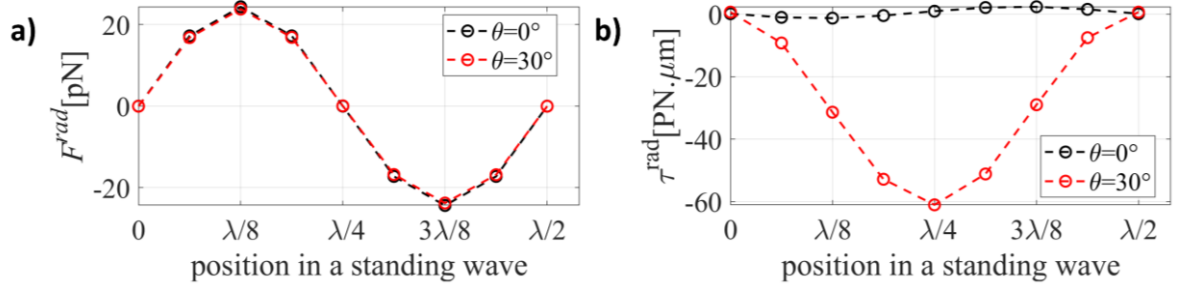


Fig 3.2. The radiation force and torque with respect to  $\Delta z$  in a standing wave on a horizontal ( $\theta = 0^\circ$ ) and tilted ( $\theta = 30^\circ$ ) polystyrene ring in a viscous water for  $f = 2\text{MHz}$ . a)  $F^{rad}$  and b)  $\tau^{rad}$  profiles.

The comparison of the acoustic radiation forces and torque versus position in a standing wave for inviscid and viscous are plotted in Fig 3.3. In both cases, the maxima are observed when the ring is  $\lambda/8$  away from the pressure node (the node is placed at  $\lambda/4$ , check Fig 3.1a). Looking at the direction of the force, it is noted that the force directs the polystyrene ring towards the pressure node for both the viscous and inviscid models. These results are consistent with the observations of (Baasch et al., 2019) on spherical particles. Considering viscosity at first and second order depicts the increased magnitude of the force as well as the torque. ARF shows the same sinusoidal trend (Fig 3.3a), and ART plots reveal cosine dependence with respect to

the position in standing wave,  $\Delta z$ . The torque in an inviscid fluid at  $\theta = 0$  is always negative, tending to keep the ring horizontally, while ring can be stayed vertically by the acoustic radiation torque in a viscous fluid depending on its position for non-rotated ring. Viscosity contribution and its counteracting effects on velocity gradients lead to smaller torque values near pressure antinodes, as shown in Fig 3.3b.

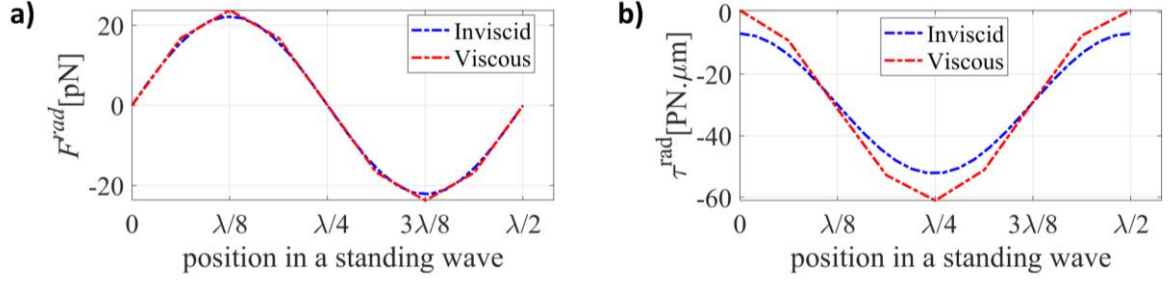


Fig 3.3. a) Comparison of the acoustic radiation forces corresponding to inviscid and viscous fluids b) Acoustic radiation torque comparison of viscous and inviscid fluids.

## 3.2. Effects of the Ring Geometry

### 3.2.1. Rotation Angle

The ARFs and ARTs in an inviscid fluid for varying  $\theta$  from  $0^\circ$  to  $90^\circ$  are plotted in Fig 3.4a and Fig 3.4b, respectively, for both  $\Delta z = 0$  and  $\Delta z = \lambda/8$ . For rings positioned at pressure nodes,  $\theta$  variation does not affect the ARF, which is almost zero as expected, indicating that pressure nodes are stable equilibrium points for the rings similar to spheres. Besides,  $F^{rad}$  for  $\Delta z = \lambda/8$  at  $\theta = 90^\circ$  deviates slightly from  $\theta = 0^\circ$ , the ratio of force values for  $\theta = 90^\circ$  and  $0^\circ$  is 0.9657. Simple analysis in Appendix A shows that ARF depends on  $J_0(2kR\sin\theta)$  in Eq.(A5); for example, for  $2kR = 0.424$ ,  $J_0(0.424 \times \sin\theta)$  changes between 1 and 0.9556 for  $0^\circ < \theta < 90^\circ$ .

The ARTs, on the other hand, follow a parabolic trend with the minimum around  $\theta = 30^\circ$ . In this configuration, the ART always aligns the ring horizontally as shown in Fig 3.4c, i.e., there

is no transition from negative to positive torque values. It should be noted that, the torque is, as expected, 0 for  $\theta = 0^\circ$  and  $\theta = 90^\circ$ . When  $\Delta z = 0$ , the torque is restorative (negative) to the horizontal alignment of the ring ( $\theta = 0$ , Fig 3.4c) up to  $\theta = 35^\circ$ , after that value, the torques are positive, indicating that the ring tends to align vertically ( $\theta = 90^\circ$ , check Fig 3.4d). Moreover, the maximum amplitude of  $\tau^{rad}$  is larger at positive torque values, indicating stronger forcing to vertical alignment. The contributions of the momentum and pressure components to the torque, seen in Fig 3.4e for  $\Delta z = 0$ , would also be of interest. It has been noted that the first and second-order terms in the ARF computation in Eq. (2-28), the force terms resulting from pressure and momentum flux, are acting antagonistically. The ring is rotated into a vertical alignment when the pressure-induced torque dominates at bigger  $\theta$ . However, at low  $\theta$ , the momentum flux component is dominant and aligns the ring horizontally. ART, in accordance with Eq. A8 in Appendix A has a slight sinusoidal dependence on the orientation angle,  $\theta$ .

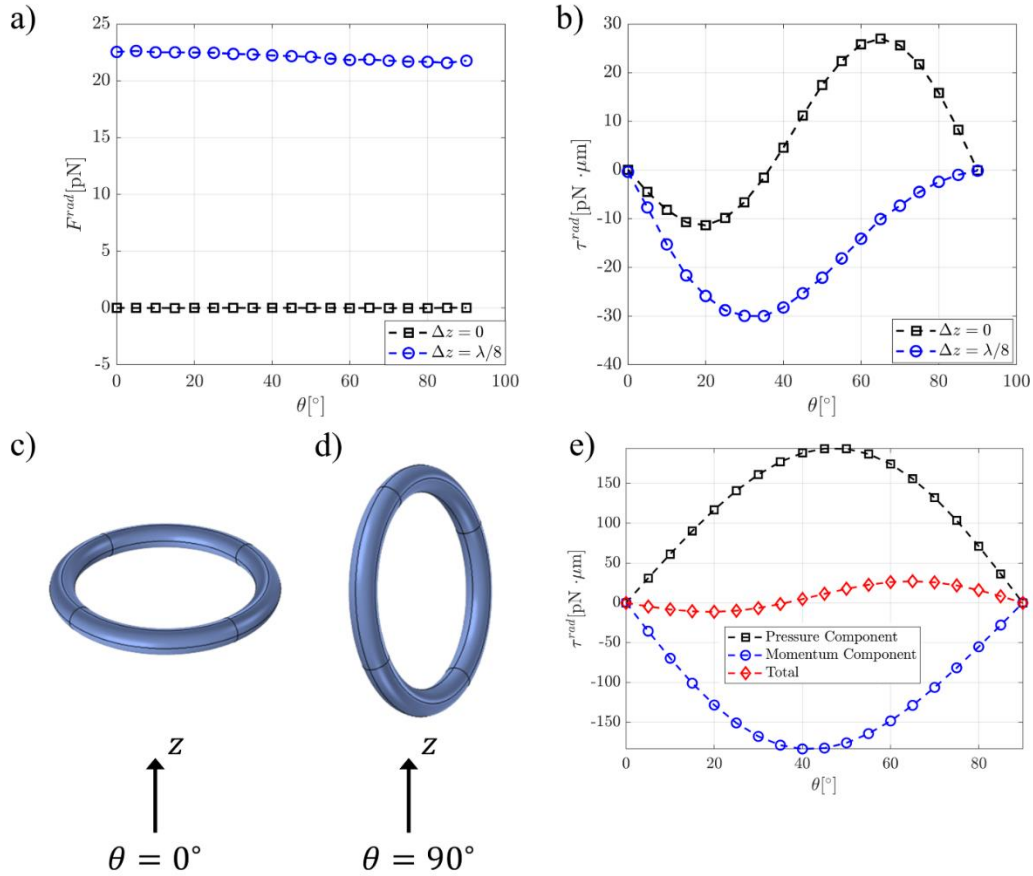


Fig 3.4. The change of (a)  $F^{rad}$  and (b)  $\tau^{rad}$  with respect to  $\theta$ . (c) shows the ring's orientation when  $\theta = 0^\circ$  and (d) shows the orientation when  $\theta = 90^\circ$ . The standing field is applied in the  $z$ - direction. (e) shows the pressure and momentum flux-driven component of the radiation torque on a polystyrene ring when  $\Delta z = 0$ .

Fig 3.5a and Fig 3.5b shows the radiation force and torque as a surface plot while varying both  $\Delta z$  and  $\theta$ . Fig.3.5a illustrates the harmonic nature of force and how it depends on location rather than rotation angle. The torque is 0 for  $\theta = 0^\circ$  and  $\theta = 90^\circ$ , as would be expected (Fig 3.5b). For other values, the torque is primarily restorative, i.e. negative or clockwise in the y-direction (Fig 2.1c); at low  $\theta$ , the ring aligns with the pressure wave on the xy-plane ( $\theta = 0$ , Fig. 3.5b). The restoring torque is the strongest when  $\Delta z$  is near to an odd multiple of  $\lambda/4$ . The torque value varies from negative to positive at great values of  $\theta$ , which causes the ring to revolve counterclockwise in the y-direction and align perpendicular to the standing wave ( $\theta = 90^\circ$ , Fig. 3.4 d). Furthermore, a zone separating the positive and negative torque values is observed (depicted in Fig 3.5b by a solid line). A rough approximation for the curve between the two regions is given by  $\theta = 62.5 - 27.5 \cos\left(\frac{k\Delta z}{2}\right)$ . This curve indicates that by adjusting  $\Delta z$ , the ring may be rotated and maintained at any  $\theta$ .

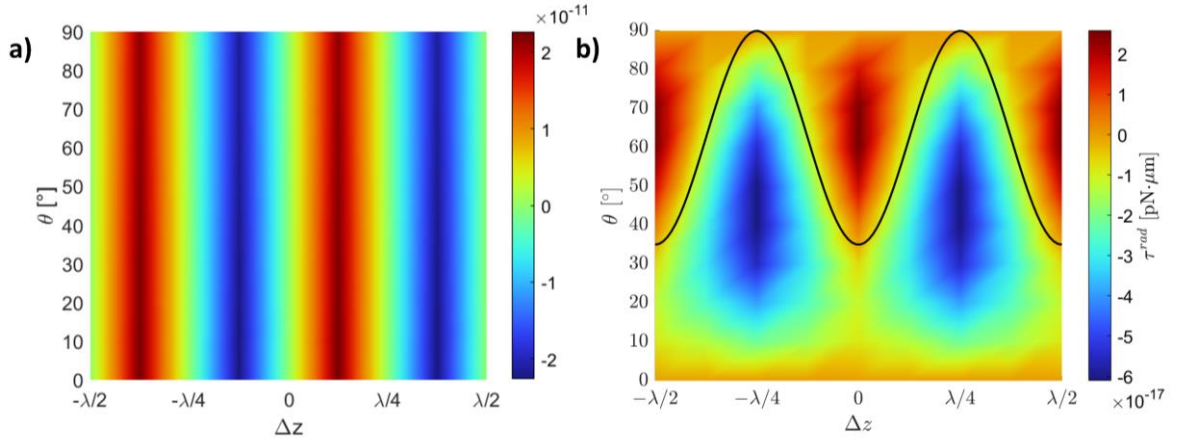


Fig 3.5. The change of (a)  $F^{rad}$  and (b)  $\tau^{rad}$  with respect to  $\theta - \Delta z$ . The standing field is applied in the z-direction on a polystyrene ring in an inviscid fluid when  $\theta$  varies between  $0^\circ$  and  $90^\circ$ .

On the other hand, as can be seen in Fig 3.6b, considering viscosity at  $\Delta z = \lambda/8$  and  $70^\circ < \theta < 90^\circ$  the torque is negligible, and the ARF and ART are at their minimum values. Indeed, by increasing the  $\theta$ , the torque increases to reach its maximum at  $\theta = 35^\circ$  when  $\Delta z = \lambda/8$  like inviscid study. Also, at  $\Delta z = \lambda/8$ , in both viscous and inviscid fluids, the torque is always negative and restorative to the horizontal alignment.

The ARF slightly varies in a viscous fluid when the ring rotates with maxima at  $\theta = 0^\circ$ , and its variation is greater than in an inviscid fluid shown in Fig 3.6a and Fig 3.7a. Similar to inviscid fluid, ARF mostly depends on the position of the ring in the standing wave rather than the rotation angle.

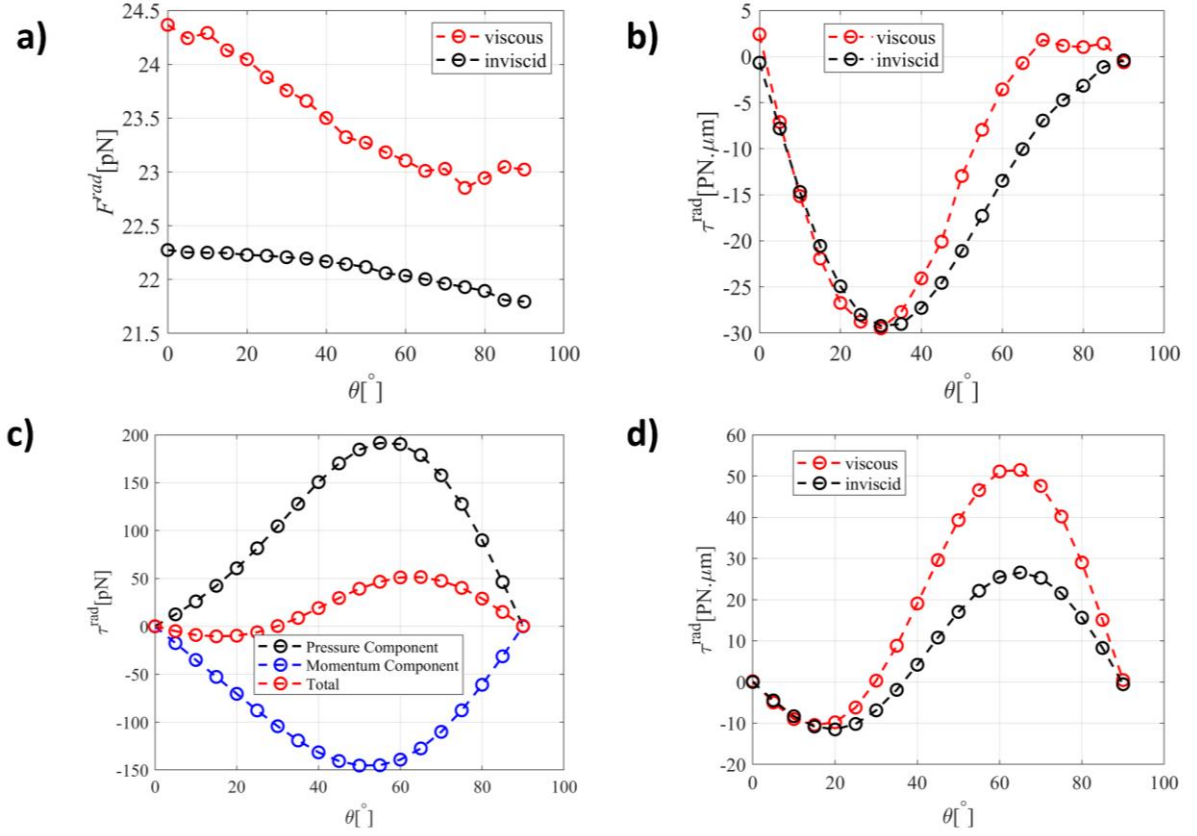


Fig 3.6. (a,b) comparison of Acoustic radiation forces and torques of inviscid and viscous fluids for  $\Delta z = \lambda/8$ , (c) Acoustic radiation torques and contribution of pressure and velocity for a polystyrene ring in viscous fluid for  $\Delta z = 0$ , (d) Comparison of acoustic radiation torque of inviscid and viscous fluid for  $\Delta z = 0$ .

Moreover, the pressure and velocity contributions to the ART computations separately are shown in Fig 3.6c for  $\Delta z = 0$ , meaning the ring is positioned in the velocity node of the standing wave. At low  $\theta$ , the pressure and velocity contributions are in the same order, but with increasing the rotation angle, the pressure contribution exceeds the velocity contribution. Initially, changing the ring orientation from  $\theta = 0$ , second-order velocity contribution to the torque dominates the pressure contribution until  $\theta = 30^\circ$ , but with increased rotation angle, pressure gradient predominates the torque that leads to locating the ring in a vertical alignment. It can be concluded that positive torque is induced by pressure momentum dominating the velocity momentum. The surface plot of ARF and ART acting on a polystyrene ring, in which both  $\Delta z$  and  $\theta$  are varying in a viscous fluid, is shown in Fig 3.7. The torque is positive and tends to locate the ring to the wave direction at  $30^\circ < \theta$  near the pressure antinodes (or velocity nodes), where the pressure gradient dominates the velocity gradients. The positive torque reaches its maximum at  $\theta = 62^\circ$  at pressure antinodes, as can be seen in Fig 3.6d and Fig 3.7b. However, the more significant torque is a restorative torque occurring for rings positioned in

the pressure nodes. The ART is zero not only at  $\theta = 0^\circ, 90^\circ$  but also at separating zone. Similar to inviscid fluids, a zone separating the positive and the negative torque values is observed (depicted in Fig 3.7b). The surface plot indicates which combination of  $\Delta z$  and  $\theta$  aligns with the aim of applying an acoustic standing wave on a polystyrene ring. Harmonic nature of the ARF and ART on a polystyrene ring in a viscous fluid can be seen Fig 3.7a and Fig 3.7b. As it is described in Appendix A, the torque shows cosine dependency and force sinusoidal dependency on the rotation angle.

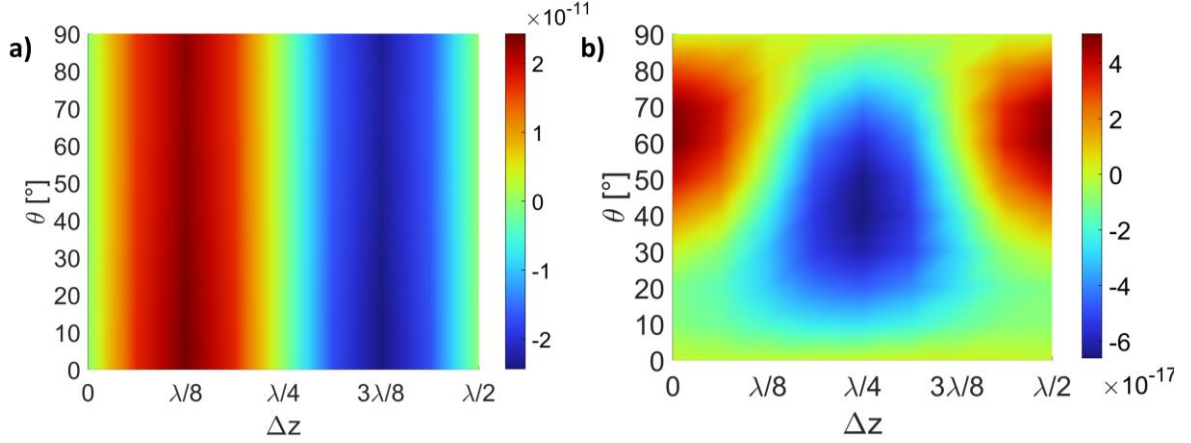


Fig 3.7 The change of (a)  $F^{rad}$  and (b)  $\tau^{rad}$  with respect to  $\theta - \Delta z$ . The standing field is applied in the z-direction on a polystyrene ring in a viscous fluid when  $\theta$  varies between  $0^\circ$  and  $90^\circ$ .

It can be seen that a slightly viscous fluid, such as water studied in this thesis ( $\delta/a = 0.15$ ), does not significantly affect the behavior of the ARF and ART on a rotated ring. Therefore, the relation between viscosity and rotation angle is studied, as shown in Fig 3.8. It is of great interest in the ART plot (Fig 3.8b) that ART increases with increased viscosity; the maximum torque occurs at low  $\theta$  for less viscous fluids, and the strongest torque is at higher  $\theta$  for highly viscous fluids. As seen in Fig 3.8b, positive and negative torques are separated with a zero-torque zone; in contrast to less viscous fluids, zero torque happens at higher  $\theta$ , and zero torque occurs at low  $\theta$  for highly viscous fluids. Note that increased viscosity leads to a sign change of negative ART into positive ART at low  $\theta$ , and tends to align the ring in the wave direction. Fig 3.8a shows that when viscosity increases, as was expected, ARF is insensitive to  $\theta$ ; on the other hand, enhanced positive torque in highly viscous fluids and ring alignment affects the ARF on the ring.

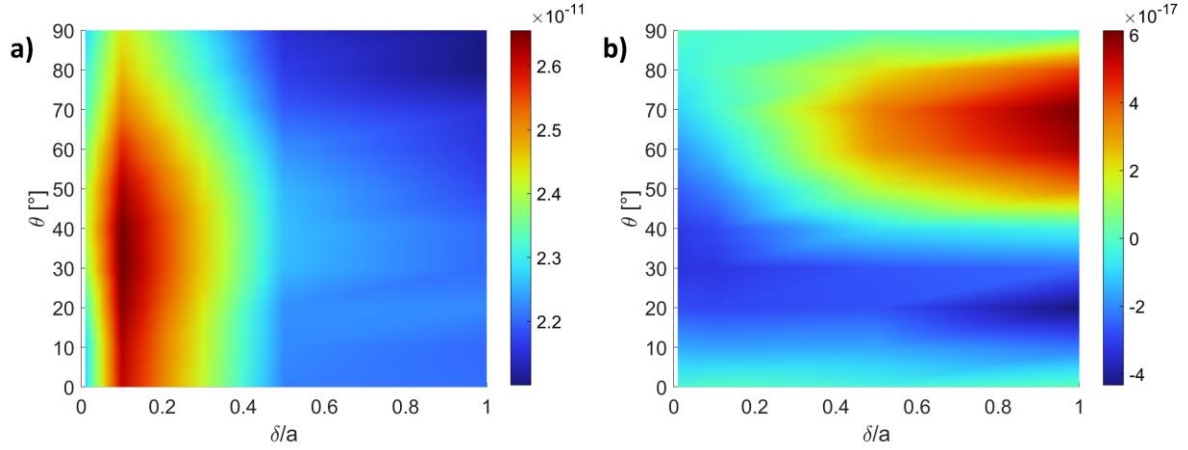


Fig 3.8 The change of (a)  $F^{rad}$  and (b)  $\tau^{rad}$  with respect to  $\theta - \delta/a$ . The standing field is applied in the z-direction on a polystyrene ring in a viscous fluid with different viscosities when  $\theta$  varies between  $0^\circ$  and  $90^\circ$ .

Various parametric studies are performed to determine the dependency of the ARF and ART on the ring orientation and particle-fluid density ratio, as surface plots are displayed in Fig 3.9. As expected, the ART and ARF enhances when the ring particle is heavier than the fluid. Fig 3.9a shows that the heavier ring experiences greater ARF at low  $\theta$ . However, the maximum torque value for the heavier ring is restorative torque at  $\theta = 45^\circ$ .

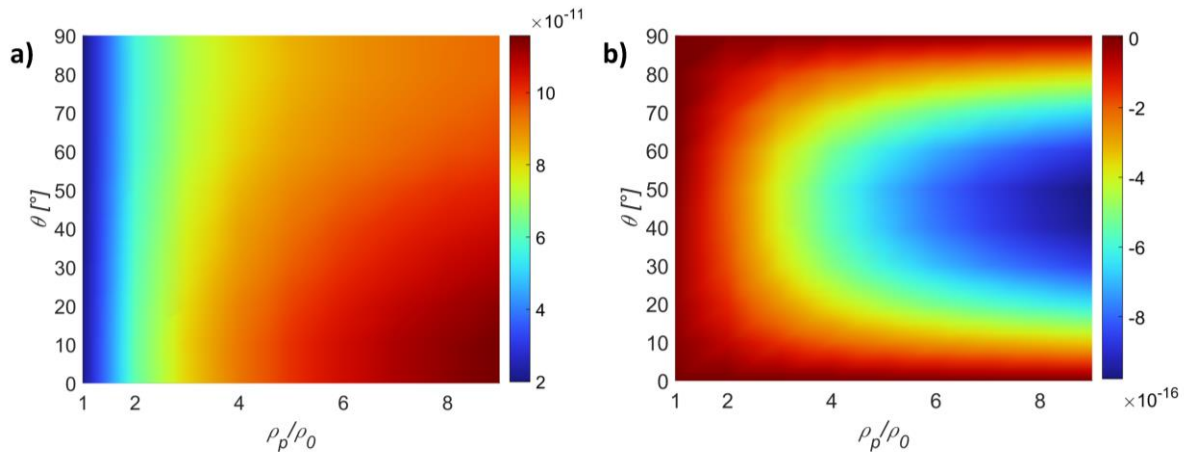


Fig 3.9 The change of (a)  $F^{rad}$  and (b)  $\tau^{rad}$  with respect to  $\theta - \rho_p/\rho_0$ . The standing field is applied in the z-direction in a viscous fluid with different densities for the ring when  $\theta$  varies between  $0^\circ$  and  $90^\circ$  at  $\Delta z = \lambda/8$ .

### 3.2.2. Major and Minor Radius

Minor and major ring radii's impact on the ARF and ART are shown in Fig 3.10.  $F^{rad}$  increases quadratically with increasing  $a$  due to the volume-dependency nature of the ARF, as shown in Fig 3.10a. Fig 3.10b displays the ART for the rotated ring ( $\theta = 30^\circ$ ) with respect to  $a$ , with increasing  $a$  a quadratic enhanced ART is reported until  $a = 4 \mu\text{m}$ , but then the torque exceeds two times, passes through zero, and rises above  $500 \text{ pN} \cdot \mu\text{m}$  at  $a = 4.2 \mu\text{m}$ . Geometry changes influences significantly the ART and at distinct  $a$  leads to sign change of the torque. At small values of  $a$ , the ring experiences a restoring torque that tends to move the ring to a horizontal alignment ( $\theta = 0^\circ$ ). However, after changing the sign of the ART, the larger ring tends to be vertically aligned by the positive torque ( $\theta = 90^\circ$ ).

The ART exhibits a sharp jump with increasing  $R$  (Fig 3.12d), similar to Fig 3.10b. Besides, increasing the major radius of the ring raises the ARF linearly as the volume of the ring varies linearly with  $R$ . This ART moves rings with bigger  $R$  toward a horizontal alignment ( $\theta = 0^\circ$ ), whereas rings with smaller  $R$  are aligned vertically ( $\theta = 90^\circ$ ).

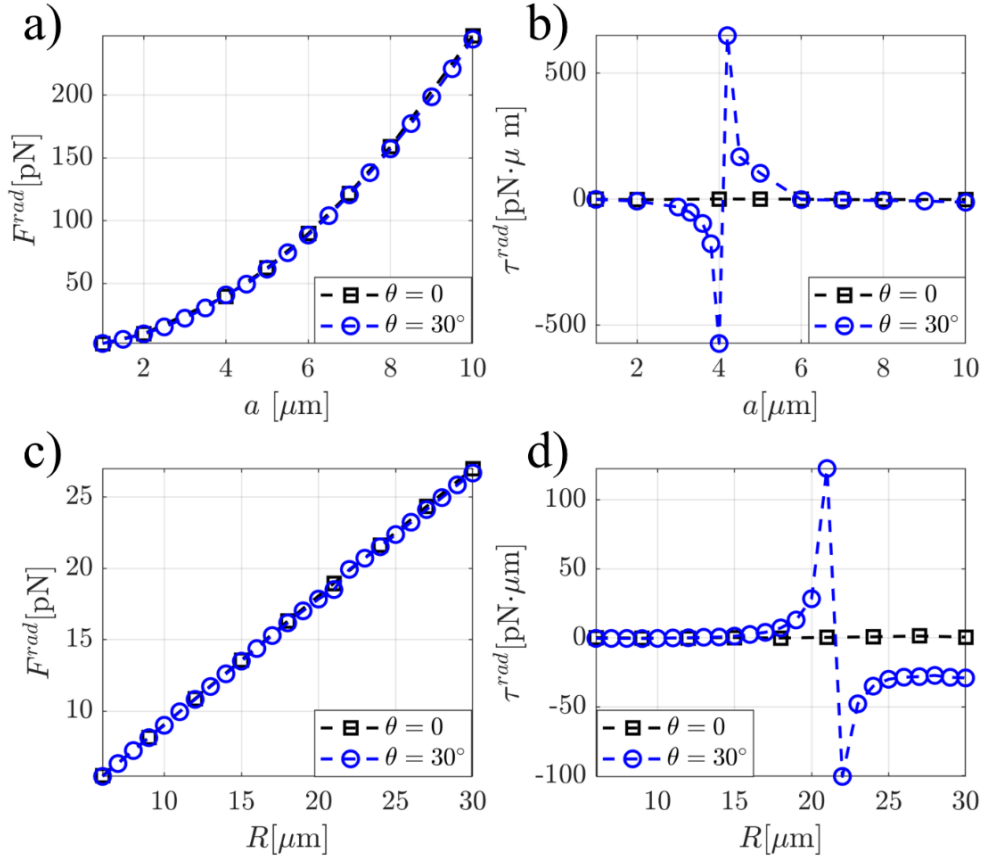


Fig 3.10. (a) Change of  $F^{rad}$  with respect to  $a$ , (b) change of  $\tau^{rad}$  with respect to  $a$ , (c) change of  $F^{rad}$  with respect to  $R$  and (d) Change of  $\tau^{rad}$  with respect to  $R$ .

Resonance effects on the intensity of vibrations and resulting pressures cause dramatic changes in torque values. Near the resonance frequencies of a ring in the standing wave, the magnitude of local vibrations and, as a result, the local momentum flux (because velocity is the product of frequency and displacement amplitude) and pressure considerably rise. These effects are averaged out in the computation of the total ARF using Eq. (2-28) because the overall volume change caused by compressibility is negligible and out-of-phase displacements typically cancel each other out. While the ART depends on the amplitude of local vibrations, those effects are not cancelled out because of the cross-product with the position, as stated by Eq. (2-28).

To further illustrate the consequences of vibrations approaching resonance, displacement and pressure amplitudes are given in Fig 3.11. The displacement field for the ring with a minor radius of  $3.1\mu m$  is depicted in Fig 3.11a, where the displacements are on the order of nanometers. In contrast, displacements in Fig 3.11b for the value of  $a = 4.1\mu m$  are on the order of microns, which are about four orders of magnitude more considerable than displacements for the value of  $a = 3.1\mu m$  as the indication of resonant. Likewise, the corresponding pressure profiles, with the maximum amplitude increasing by four orders of magnitude in the resonating case, are depicted in Fig 3.11c and Fig 3.11d. Moreover, for other asymmetrical structures like discs, resonance has revealed a substantial impact on ARTs in the literature (Garbin et al., 2015).

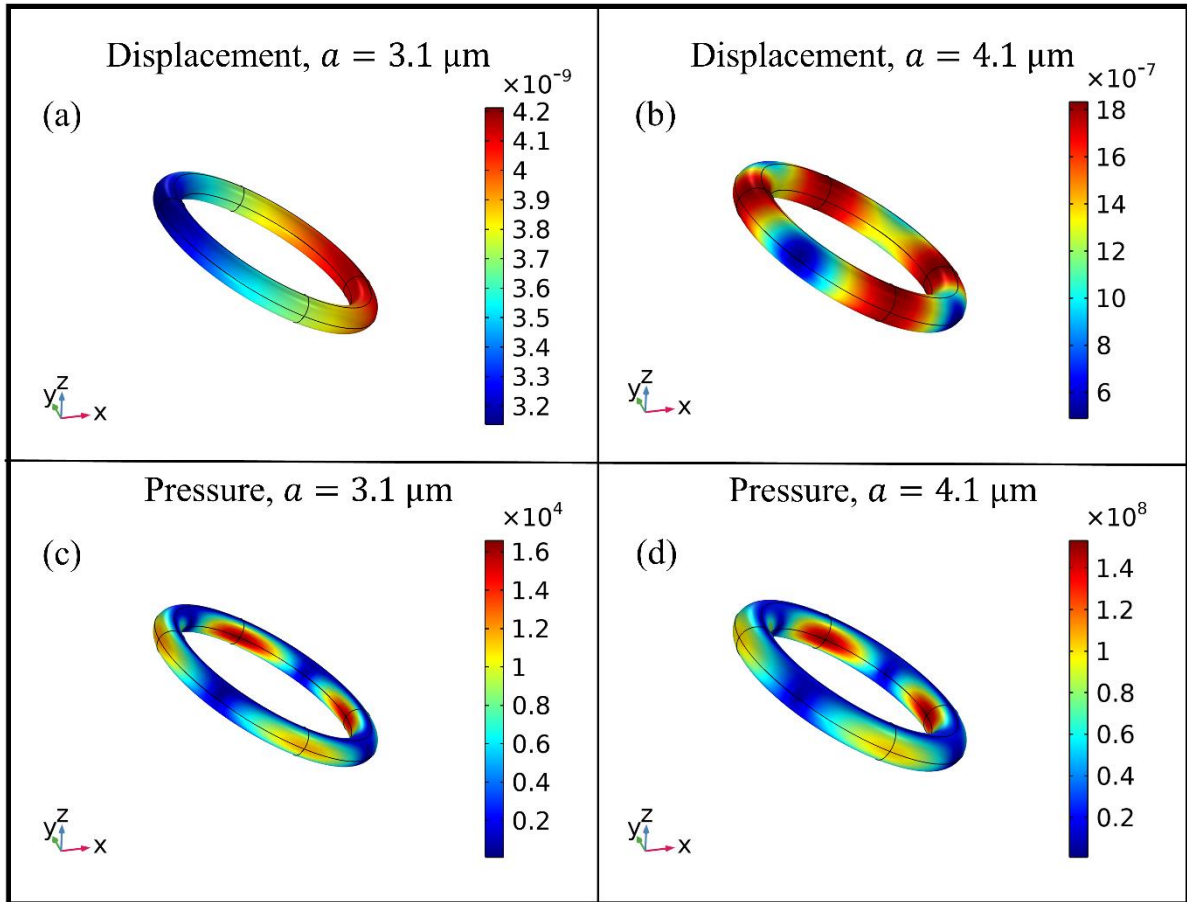


Fig 3.11. The displacement ((a)-(b)) and the pressure ((c)-(d)) distributions on non-resonating ((a) and (c)) and resonating ((b) and (d)) rings.

Viscosity does not affect the volume-dependency of the acoustic radiation force, and as Fig. 3.12 depicts, in both viscous and inviscid fluids, ARF increases linearly with the  $R$  and quadratically with  $a$ . Thus, a larger ring experiences greater ARF than a smaller ring, particularly in a viscous fluid. The resonance behavior can be seen in both viscous and inviscid cases.

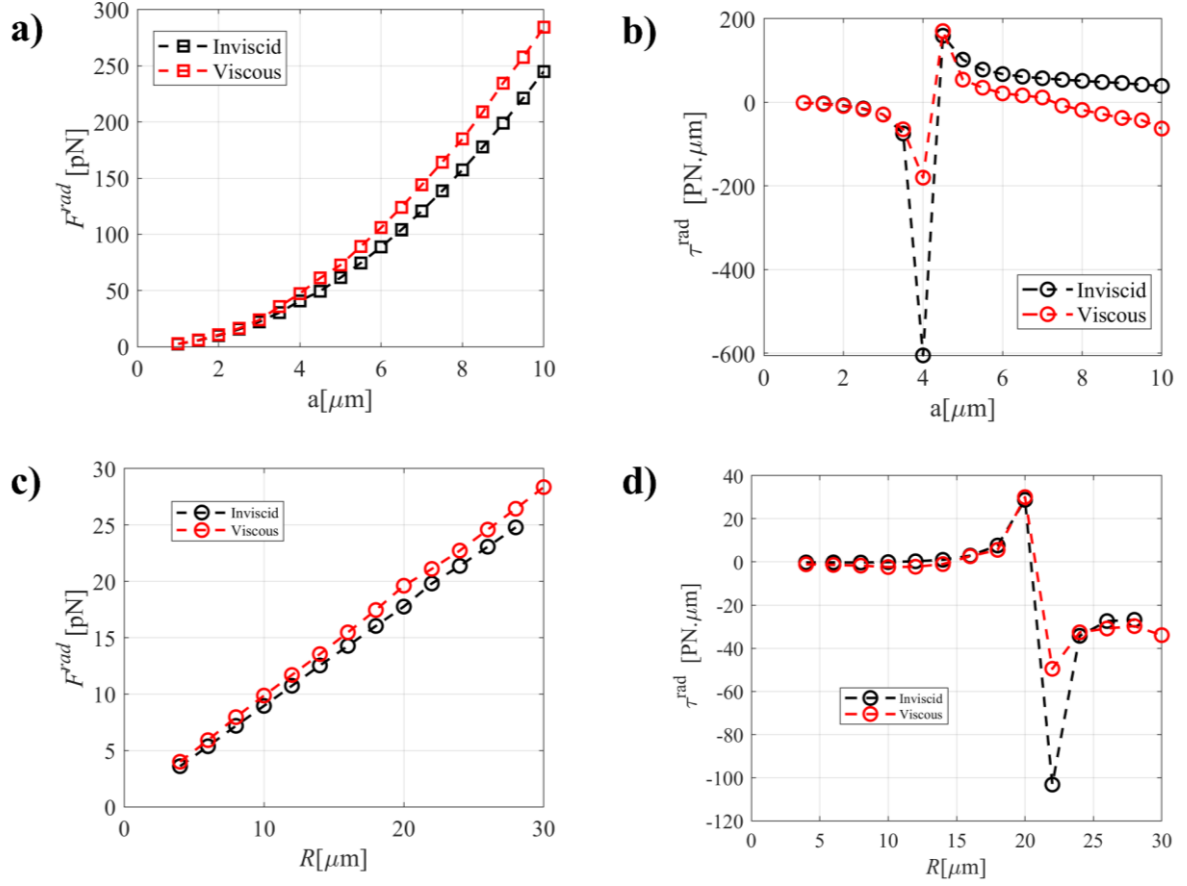


Fig 3.12. Comparison of results for viscous and inviscid fluids (a) Change of  $F^{rad}$  with respect to  $a$ , (b) change of  $\tau^{rad}$  with respect to  $a$ , (c) change of  $F^{rad}$  with respect to  $R$  and (d) Change of  $\tau^{rad}$  with respect to  $R$ .

### 3.3. Effects of the Physical Parameters

This section details how the physical parameters impact the ARFs and ARTs on a tilted ring ( $\theta = 30^\circ$ ). The acoustophoretic contrast factor  $\phi$  is the first parameter investigated here, defined as (Bruus, 2012):

$$\phi(\tilde{\kappa}, \tilde{\rho}) = \frac{1}{3} \left[ \frac{5\tilde{\rho} - 2}{2\tilde{\rho} + 1} - \tilde{\kappa} \right] \quad (3-1)$$

where  $\tilde{\rho} = \rho_p/\rho_f$  and  $\tilde{\kappa} = \kappa_p/\kappa_f$  are the particle-to-fluid density and compressibility ratios, respectively. The sensitivity analysis includes negative and positive  $\phi$  values showing whether the particle is drawn to ( $\phi > 0$ ) or repelled from ( $\phi < 0$ ) a pressure node. Fig 3.13a depicts ARF values and its transition from negative (repulsive) to positive (attractive). The ARF decreases more steeply at low  $\phi$  values, but the decrease rate becomes linear as  $\phi$  approaches zero. On the other hand, the ART values presented in Fig 3.13b demonstrate that the torque is

at its minimal magnitude at  $\phi \approx 0.1$ . Since all torque values are negative, the torques tend to align the ring horizontally at all  $\phi$  values. Finally, Fig 3.13c and Fig 3.13d illustrate how the acoustic frequency  $f$  affects ARFs and ARTs, respectively. As ART enhances concerning  $f$  with a higher-order dependence, the ARF increases linearly with respect to  $f$ . Based on the dimensional analysis in Appendix A, the ART is predicted to scale with  $k^2$ , or  $f^2$  for standing waves. Furthermore, at  $f = 4 \text{ MHz}$ , there is a resonance-type behavior similar to the behavior shown in Fig 3.11. Insets in Fig 3.13d demonstrate the vibrating ring's deformation modes, which, for visual clarity, have been scaled up 5000 times (actual displacements are in the order of nanometers). The amplitude of the Mises stresses nearly ten folds at  $f = 4 \text{ MHz}$  due to the resonance between the polystyrene ring and the standing waves in the fluid medium. According to a coupled eigenfrequency analysis for the deformation of the polystyrene ring and the pressure in the fluid medium that reveals deformation mode with the same shape as the one illustrated in Fig 3.13d occurs at  $f = 4.0118 \text{ MHz}$ , even though that the same mode is detected at  $f = 5.221 \text{ MHz}$  for free-standing rings. Other nonspherical particles in standing waves have also been subjected to resonance effects, including discs by Garbin et al. (Garbin et al., 2015) and helices by Caldag & Yesilyurt (Caldag & Yesilyurt, 2020).

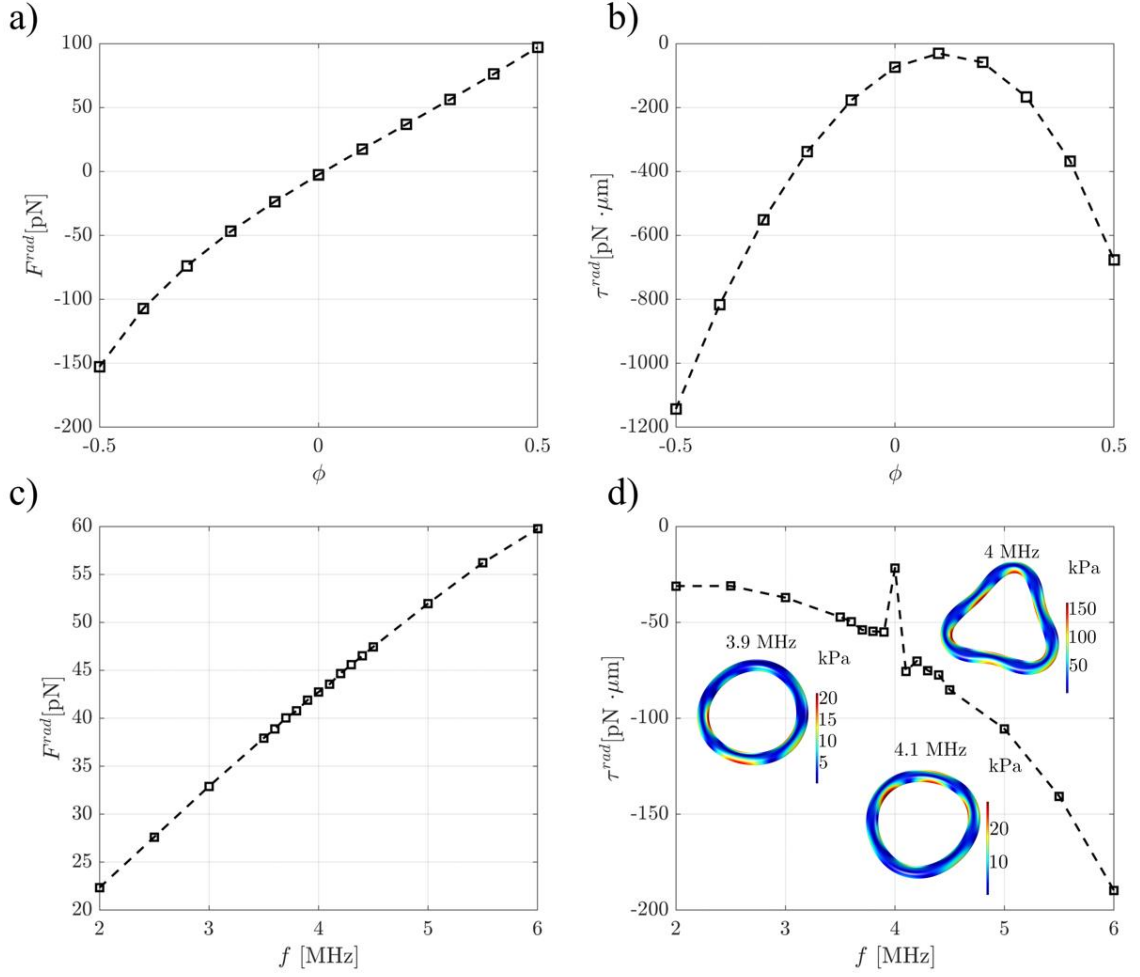


Fig 3.13. The change of (a)  $F^{rad}$  and (b)  $\tau^{rad}$  with respect to  $\phi$ . The change of (c)  $F^{rad}$  and (d)  $\tau^{rad}$  with respect to  $f$ . Insets show the deformations (5000 times scaled-up) and Mises stresses in the rings.

Moreover, the physical parameters that influence the ARFs and ARTs acting on a tilted ring ( $\theta = 30^\circ$ ) in a viscous fluid are investigated. The acoustophoretic contrast factor  $\phi$  considering viscosity is defined as (Settnes & Bruus, 2012):

$$f_1(\tilde{\kappa}) = 1 - \tilde{\kappa}, f_2(\tilde{\delta}, \tilde{\rho}) = Re \left[ \frac{2[1-\gamma(\tilde{\delta})](\tilde{\rho}-1)}{2\tilde{\rho}+1-3\gamma(\tilde{\delta})} \right]$$

$$\phi(\tilde{\kappa}, \tilde{\rho}, \tilde{\delta}) = \frac{1}{3}f_1(\tilde{\kappa}) + \frac{1}{2}f_2(\tilde{\delta}, \tilde{\rho}) \quad (3-2)$$

where  $\tilde{\delta} = \delta/a$  and  $\gamma(\tilde{\delta}) = -\frac{3}{2}Re[1 + i(1 + \tilde{\delta})]\tilde{\delta}$  and  $\delta$  represents the viscous boundary layer thickness. Similar to inviscid fluid, negative and positive  $\phi$  values indicate whether the particle subjected to an acoustic field is attracted ( $\phi > 0$ ) or repelled ( $\phi < 0$ ) from a pressure node. The effect of acoustic frequency,  $f$ , on ARFs and ARTs exerted on a polystyrene ring in viscous and inviscid fluids are compared, as shown in Figs 3.14a and 3.14b, respectively.

The ARF increases linearly with respect to  $f$  in both viscous and inviscid fluids; though, viscous ARF is greater in magnitude as was expected. As seen in Fig 3.14b, viscous effects amplify ART; however, any resonance effect is not reported in the viscous fluid for this variation range of  $f$ .

Fig. 3.14c depicts the contribution of the scattering, viscosity and streaming to the ARF on the polystyrene ring with respect to  $f$ . By using Eq. (2-28), the effect of scattered acoustic field from a compressible ring on ARF is calculated, named  $F^{scat}$ . Computing the ARF using Eq. (2-25) and stress tensor via Eq. (2-26) only in terms of first-order fields reveals the first-order viscosity impact on the ARF,  $F^{vis}$ . To distinguish between the effect of the first-order viscous and microstreaming effects,  $F^{stream}$  refers to the ARF computed by using Eq. (2-25) and (2-26) also taking second-order fields into account. As evident in Fig. 3.14c, the second-order fields maintain significant impact on the ARF particularly at higher frequencies, and it is necessary to solve the viscous model up to the second order for manipulating particles with high efficiency.

Fig. 3.14d and 3.14e show the surface plot with respect to  $\rho_0/\rho_p$  and  $\delta/a$ , implying the influence of the significant parameters in the contrast factor, density and viscosity on the ARF and ART. The force (Fig. 3.14d) exhibits greater force as  $\delta$  approaches 4 (greater viscosity) also when  $\rho_p$  with respect to  $\rho_0$  is high as it was expected. On the other hand, when  $0.8\rho_p < \rho_0 < 2\rho_p$ , the force on the particle has its minimum value. However, the other significant factor in Eq.(3-2), is not taken into account here, the compressibility effects, as compressibility can be calculated by using  $\kappa_p = \frac{1}{K} = \frac{1}{\rho_p c_p^2}$ , and  $c_p$  is fixed in all cases with the parameters given in Table 2.2.

The torque values, plotted in Fig. 3.14e, show that the torque is minimum in magnitude at less dense particles. All torque values are negative, meaning that the torques tend to align the ring horizontally at all values.

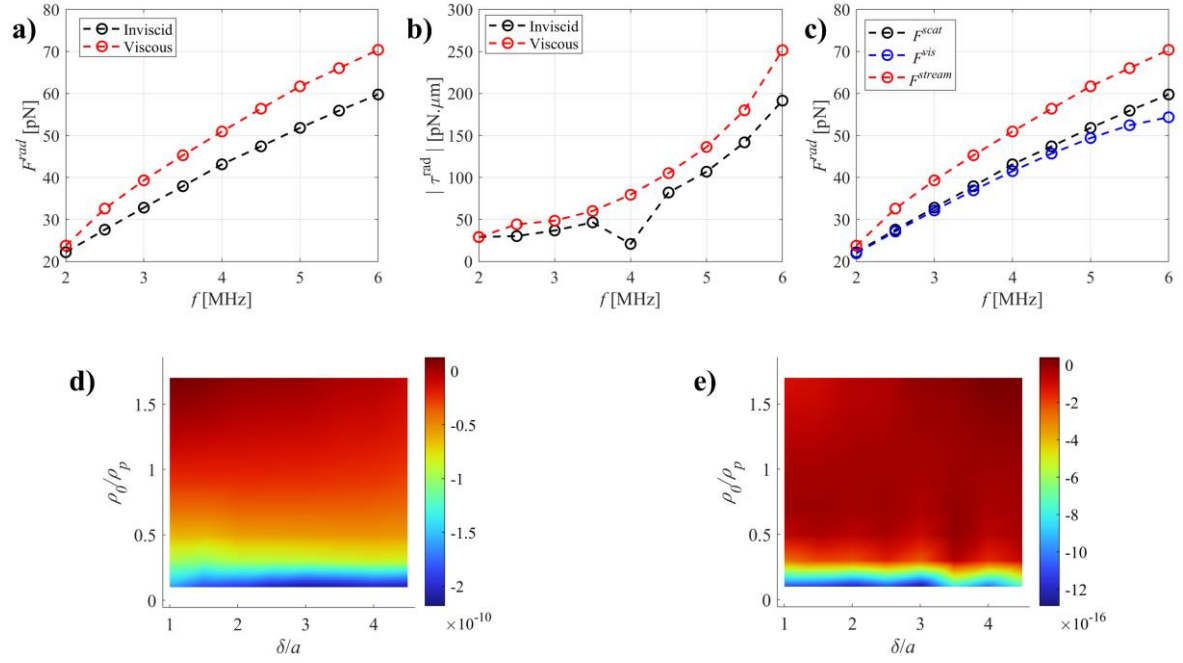


Fig 3.14. Comparison of the results of viscous and inviscid fluids; The change of (a)  $F^{rad}$  and (b)  $\tau^{rad}$  with respect to  $f$  (c) Comparison of  $F^{rad}$  with considering different contributions. The change of (d)  $F^{rad}$  and (e)  $\tau^{rad}$  with respect to  $\rho_0/\rho_p$  and  $\delta/a$ .

## 4. Secondary Forces and Scattering Effects

This chapter first analyses the numerical results compared with the analytical approach of the Chain of spheres. Then, self-scattering on the individual ring and secondary forces on a pair of rings are investigated.

### 4.1. Comparison with Chain of Spheres Approach

The chain-of-spheres approach (CoS), which is developed for the computation of the acoustic radiation forces and torques on thin helices for micro-swimming applications (Caldag & Yesilyurt, 2020), is compared to the results of a finite-element (FEM) model presented in this thesis. Following CoS, a ring can be split into sections, and each section can be represented by an equal volume sphere, for which analytical ARF calculations are available (Hasegawa, 1979). The CoS method ignores two different kinds of interaction forces: first, the forces that arise within the solid as a result of the higher order ring deformation modes such as bending, extension, stretching, and other variations on these modes which differ from the sphere deformation modes; and second, the forces that arise within the fluid as a result of the scattered waves. Those secondary effects are inherently considered using a three-dimensional modelling approach in the FEM model. Thus, differences between the CoS and FEM results are considered to be due to these secondary effects.

In computations of the CoS method, the ring is divided into  $N_{sph}$  equal segments that are roughly represented by spheres with the same volume as each segment, which stretches between  $\varphi_j$  and  $\varphi_{j+1}$ , where  $\varphi$  is the azimuthal angle and  $j = 1, \dots, N_{sph} - 1$ ; the  $j$ th sphere is positioned at the centroid of the  $j$ th segment, which is determined by:

$$\mathbf{c}_j = \frac{N_{sph}}{2\pi} \int_{\varphi_j}^{\varphi_{j+1}} \mathbf{R}_\theta \mathbf{p}_r(\varphi) d\varphi \quad (4-1)$$

where the centerline of the ring is indicated in the reference frame by the position vector,  $\mathbf{p}_r(\varphi) = R[\cos \varphi, \sin \varphi, 0]'$ , and  $\mathbf{R}_\theta$  is the rotation matrix for the frame rotated by  $\theta$  with the ring as shown in Fig 2.1. To ensure that spheres and segments have the same volume, the

radius of spheres is set to  $a_s = \left(\frac{3\pi a^2 R}{2N_{sph}}\right)^{1/3}$ . Fig 4.1 shows a basic schematic of the CoS methodology.

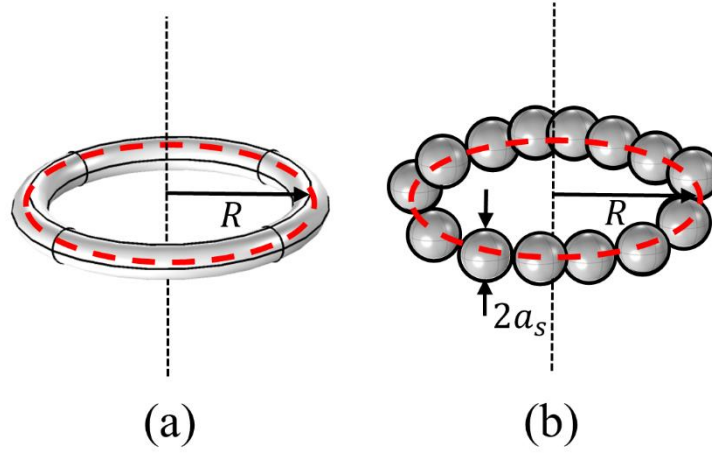


Fig 4.1. Schematic of chain-of-spheres methodology. (a) Shows the original ring geometry, (b) shows the representation of the ring with  $N_{sph} = 14$  spheres with radius  $a_s$  placed along the circle of the ring which is  $R$  away from the center of the ring. The circle is shown in red dashes.

Hasegawa derived a simple theoretical formula for the ARF on a single compressible sphere for standing waves (Hasegawa, 1979):

$$F_j^{rad} = \pi a_s^2 E Y_{st} \sin(2k\Delta z) \quad (4-2)$$

Where  $E = \frac{1}{2} \rho_0 k^2 |A|^2$  denotes the acoustic energy density ( $A$  represents the potential amplitude of the field) and  $Y_{st}$  is known as the acoustic radiation force function (Hasegawa, 1979). As a result, the summations of ARFs over each sphere are used to calculate the overall ARF and ART:

$$F^{rad} = \sum_{j=1}^{N_{sph}} F_j^{rad} \quad (4-3)$$

$$\tau^{rad} = \sum_{j=1}^{N_{sph}} (\mathbf{c}_j - \mathbf{r}_0) \times F_j^{rad} \quad (4-4)$$

Additional information on the CoS and in detail ARF computations in a standing field are discussed further in Appendix B. Comparisons between polystyrene, copper, and aluminum

rings considering  $\Delta z$  variation for tilted rings with  $\theta = 30^\circ$  are displayed in Fig 4.2. In the calculations of CoS, to control the error caused by the segmentation of the ring, a convergence study is first conducted, and a sufficient number of segments is obtained to be  $N_{sph} = 25$ . The results of CoS for ARF computations are in good agreement with FEM results for both polystyrene and copper rings, as shown in Fig 4.2a and Fig 4.2c; the agreement is much better for polystyrene than copper, where a maximum of 5% relative error is seen. However, as Fig 4.2e displays, there is a poor agreement for the aluminum ring for the ARF. Similarly, ARTs are presented in Fig 4.2 b-f, where a dramatic difference between the FEM and the CoS results for polystyrene and copper rings are observed, with the discrepancy being more prominent for the copper ring. Interestingly, the ARTs show extremely high agreement despite the differences between the FEM and the CoS results for the ARFs computation of the aluminum ring.

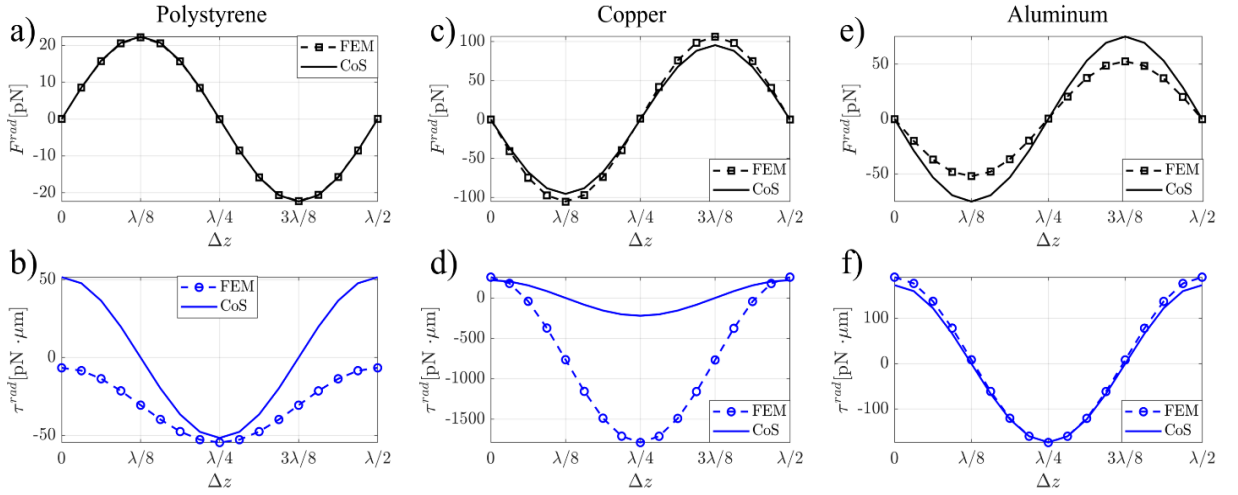


Fig 4.2. Comparison of the radiation forces ((a), (c) and (e)) and torques ((b), (d) and (f)) obtained from the FEM model and with the CoS method. (a) and (b) the results for polystyrene ring, (c) and (d) the results for copper ring and (e) and (f) the results for aluminum ring.

#### 4.1. Self Scattering

To clarify the differences in ART computations of CoS and FEM methods, we first verify that the ARF and ART contributions from each sphere in the CoS model agree with the values calculated from the FEM model by modeling individual ring segments in separate FEM simulations. Results related to these individual models are not reported here since it would not give any extra information and would be a repetition of Fig 4.2a and Fig 4.2b. This study

confirms the main principle of the CoS technique, i.e., shows that individual ring segments can be taken as spheres and the corresponding force and torque computations are consistent. Then, using the FEM model, the radiation forces on rings made up of ten toroidal segments are compared. The ring-shaped toroidal segments with a  $2^\circ$  gap between them are shown in Fig 4.3a; this gap size has no impact on the convergence of FEM simulations. ARF results are shown in Fig 4.3 for segmented polystyrene, copper, and aluminum rings at the baseline parameters in Table 2.1 with  $\Delta z = \lambda/8$  and  $\theta = 30^\circ$ . Under the numbering in Fig 4.3a., segments are placed sequentially in their proper places. Therefore, to maintain each segment's location, the entire ring's location is positioned at the same  $\Delta z = \lambda/8$  and  $\theta = 30^\circ$ . Forces on segments are estimated for three distinct configurations: (i) for each individual segment placed one at a time in the acoustic field; (ii) for all detached segments that form the ring shape as illustrated in Fig 4.3a; and (iii) for the entire ring made up of segments connected to one another. ARF values for polystyrene, copper, and aluminum rings are displayed in Fig 4.3b-d, respectively. The force values between the segments of the polystyrene ring, whether they are assembled as illustrated in Fig 4.3b or inserted one at a time individually, differ very little (less than  $0.05 \text{ pN}$ ). This result clearly implies that self-scattering between the segments does not significantly affect local forces. At the same time, the elastic behavior of the entire slender structure does for which the maximum deviation occurs at segment 6 as high as  $9.9 \text{ pN}$ .

For the copper ring, the force values for individual segments inserted one at a time vary somewhat between  $9.05$  and  $10.57 \text{ pN}$  (black circles in Fig 4.3c); little discrepancies result from a numerical error while computing stresses around the sharp edges of segments. The findings are not considerably changed by mesh improvements up to 3M dof (exceeding a 140 GB memory requirement). When the detached segments are placed in the acoustic field together, the forces on the segments are significantly different from those on the individual segments, up to  $7.5 \text{ pN}$  for the first segment. Furthermore, for segments 3 – 8, the forces on the detached segments (red stars) are very similar to the forces on the corresponding segments in the ring (blue squares), with the difference being less than  $1.8 \text{ pN}$ . According to this finding, the ARF is significantly influenced by the scattering of waves between the segments.

Lastly, for the aluminum ring, the ARF behavior is more like polystyrene than copper since the difference in forces on single and detached segments is less than  $2.8 \text{ pN}$ , as a whole, the deviation between the local forces on detached segments and the complete ring segments is smaller, reaching up to  $5.8 \text{ pN}$  for the sixth segment. It is concluded that the ring being divided into separate segments alters the local forces without changing the overall net force. Therefore,

the ARF prediction of the chain-of-spheres method is near to the FEM results for the entire ring but fails to evaluate the ART accurately. The CoS method must be enhanced by integrating the connections between the spheres to capture the bending moments and the impacts of the scattered acoustic field in order to assess the significance of those effects.

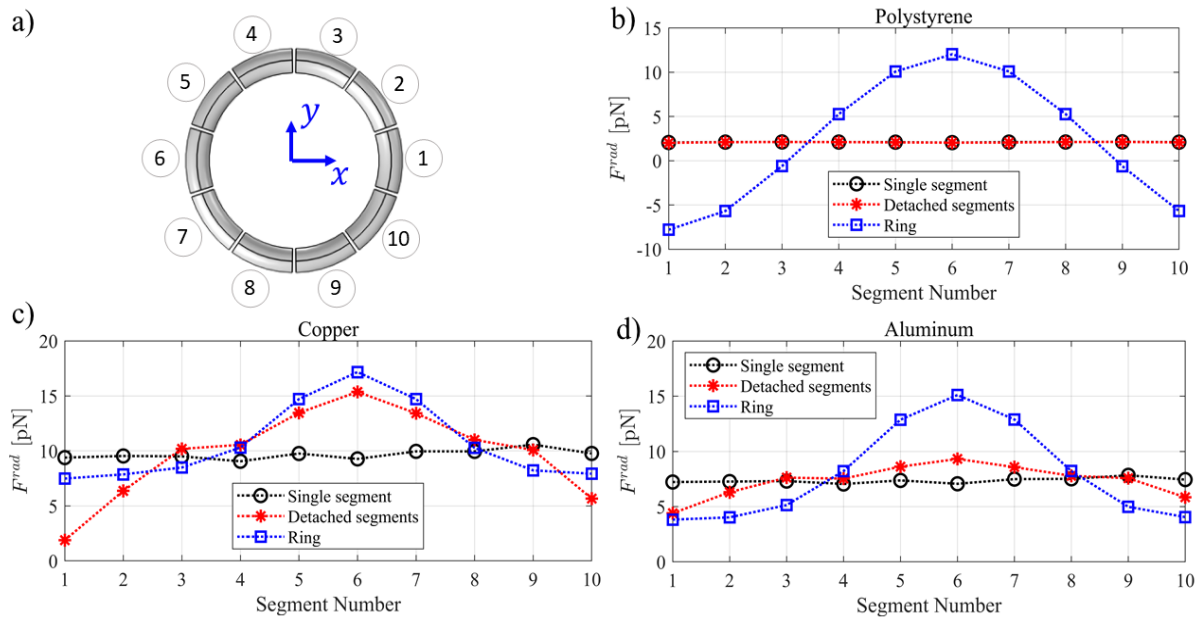


Fig 4.3. (a) The depiction of the ring decomposed into segments; local acoustic radiation forces (ARF) on each segment of polystyrene (b), copper (c) and aluminum (d) rings. ARF on each individual segment placed in the acoustic field without others is shown with black circles; forces on the detached segments forming a ring (see the picture in (a)) is shown with red stars; and the forces on the complete ring composed of segments in contact are shown with blue squares.

The pressure and velocity contributions to the radiation force are examined to determine how each one affects the movement and alignment of the rings for three different materials - polystyrene, aluminum, and copper- each stiffer than the others. Fig 4.4 shows the separated contribution of the velocity and pressure terms for a polystyrene ring in water. Individual segments are slightly in different positions for a standing wave. As can be seen in Fig 4.4a and Fig 4.4c, individual segments similar to segments of detached ring experience constant local forces and their separated contributions are constant except for slight variations in a few positions. However, the contribution is dominated by pressure gradient for the individual and detached segments; velocity contribution predominates the force for the entire ring. Indeed, Fig 4.4. reveals the effect of solidity on the local acoustic radiation forces on individual segments of the ring; also, comparing Fig 4.4a and Fig 4.4b depicts the insignificant influence of self-scattering between segments.

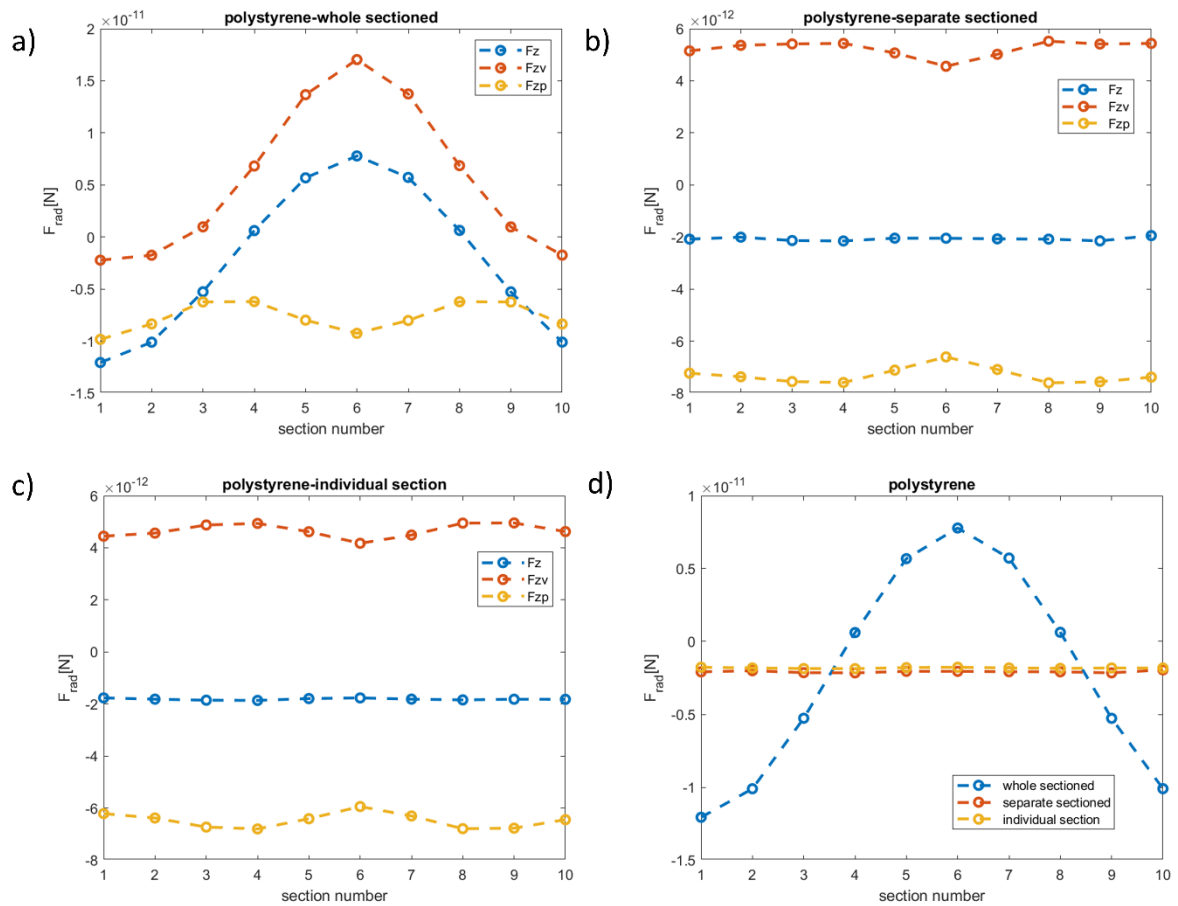


Fig 4.4. Local acoustic radiation forces (ARF) on each segment of polystyrene and contribution of pressure and velocity terms to ARF for  $f = 0.6\text{MHz}$ ; (a) the forces on the complete ring composed of segments in contact, (b) forces on the detached segments forming a ring (c) forces on each individual segment placed in the acoustic field without others (see the picture in Fig.4.3a) .

Fig 4.5 depicts separate contributions for an aluminum ring. As a result of decreasing compressibility and increased density by changing the material of the ring to aluminum, pressure contribution grows in the order of ARF in all cases and dominates the velocity gradient.

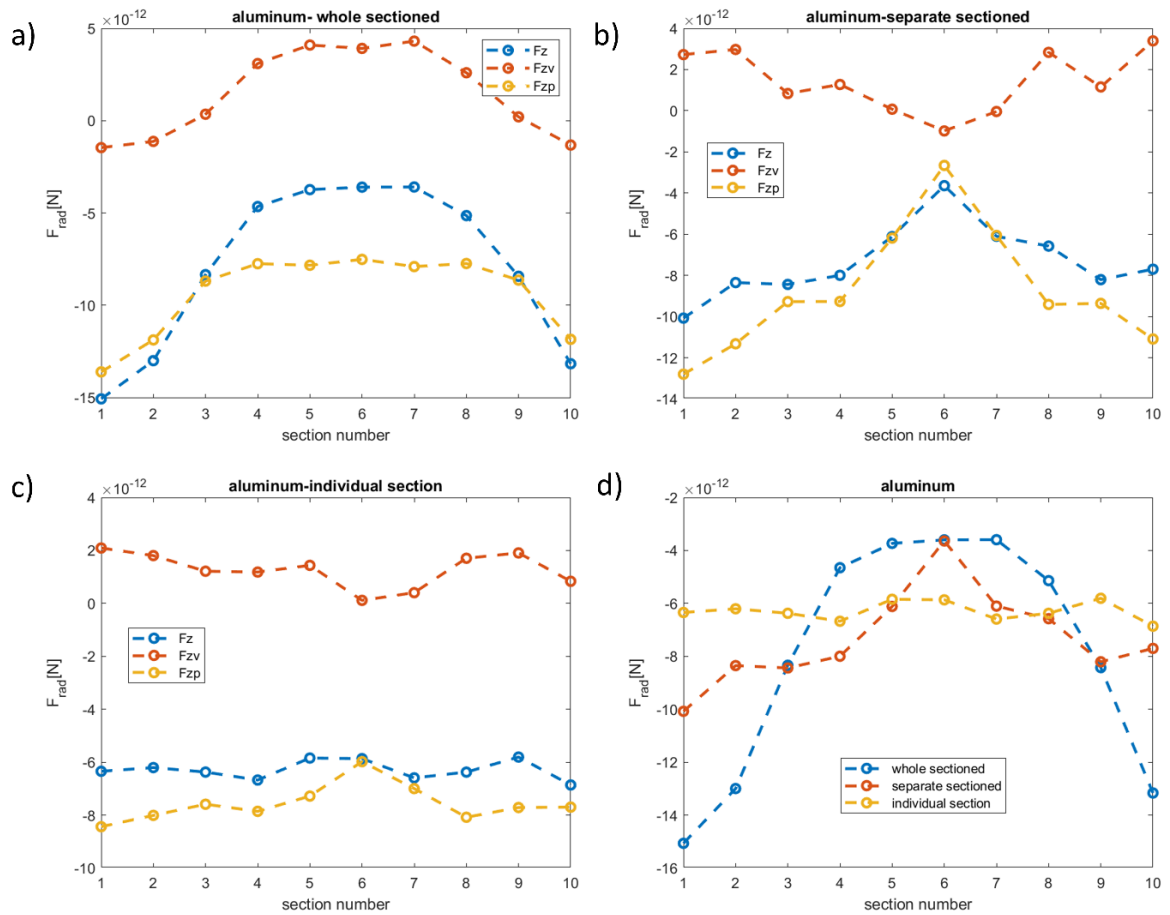


Fig 4.5. Local acoustic radiation forces (ARF) on each segment of aluminum ring and contribution of pressure and velocity terms to ARF; (a) the forces on the complete ring composed of segments in contact, (b) forces on the detached segments forming a ring (c) forces on each individual segment placed in the acoustic field without others (see the picture in Fig. 4.3a).

Fig 4.6 reveals the ARF on the copper ring and the effect of ring compressibility, density, and wave speed on the local forces and the velocity and pressure contribution. It can be seen that with increasing the density of the ring and decreasing compressibility, pressure contribution to the ARF enhances and dominates the velocity contribution even in a ring. In all three cases, velocity and pressure contributions-related changes are in the same order. Comparing the three materials reveals that compressibility increases absorption of the scattering pressure gradients, and local forces are affected by the compressibility factor more than the position and self-scattering.

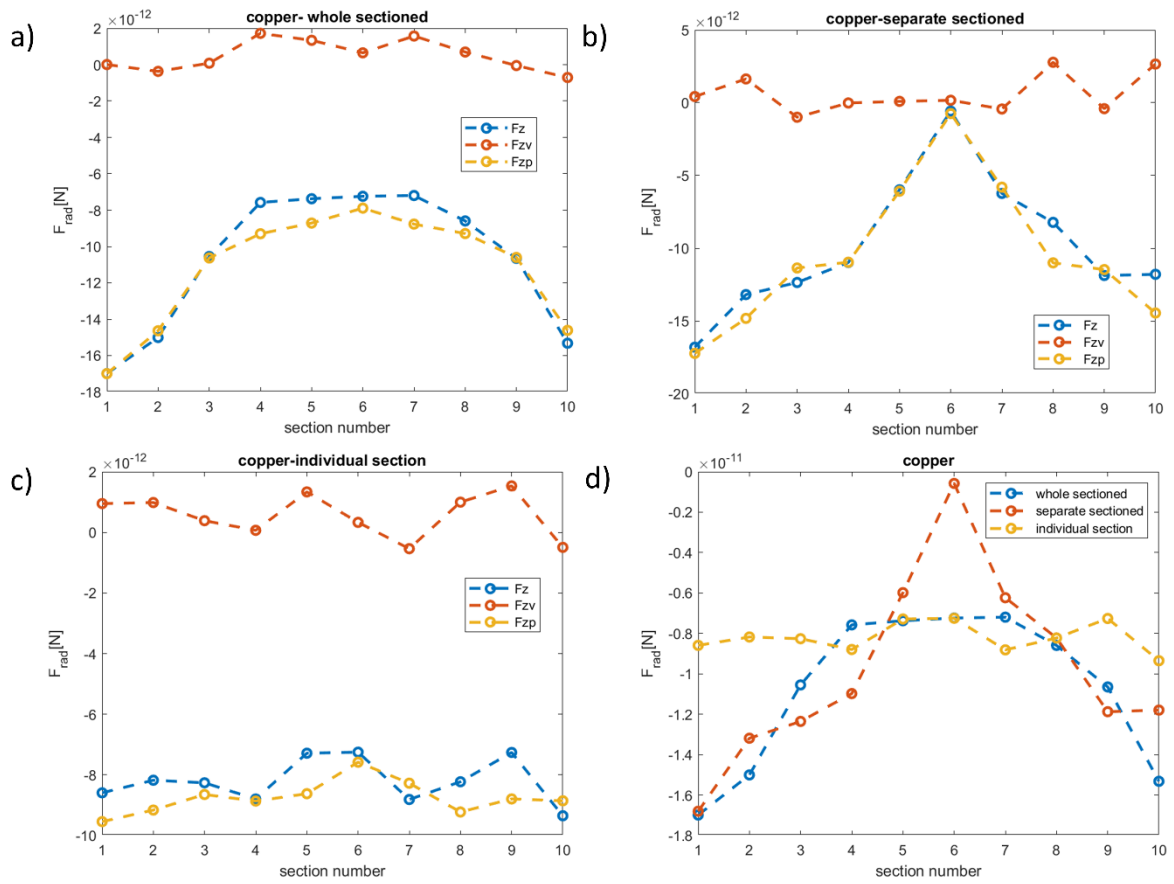


Fig 4.6. Local acoustic radiation forces (ARF) on each segment of copper ring and contribution of pressure and velocity terms to ARF; (a) forces on the complete ring composed of segments in contact; (b) forces on the detached segments forming a ring; (c) forces on each individual segment placed in the acoustic field without others (see the picture in Fig. 4.3a).

## 4.2. Microstreaming Effects on the Secondary Forces

Microstreaming, acoustic radiation, and interaction forces on the particles all result from the scattering of an acoustic wave by existing multiple particles in a fluid medium. These forces comprise the primary acoustic radiation force (ARF) and the secondary acoustic radiation force, respectively, by single-particle sound scattering and acoustic particle-particle interactions. Scattering through viscous losses close to the particle's surfaces results in microstreaming, micro-scale eddies that can affect both the primary and secondary radiation forces. Theoretical models of the acoustic radiation force frequently ignore microstreaming. The streaming flow of fluid around an oscillating object is known as microstreaming. A particle experiences a drag from this streaming, which is predicted to change the behavior of the particle. Streaming develops due to mechanisms for energy dissipation in the bulk phase, including energy absorption by the fluid and dissipation at interfaces between the fluid and solid surfaces. The fluid flow is produced by the vorticity brought on by the boundary layer oscillations surrounding it.

Here, we look into how acoustic microstreaming affects the ARF acting on a pair of elastic ring particles in an ultrasonic standing wave. Using our finite-element model that solves compressible Navier stokes equations up to second order and considers the contribution of microstreaming. These nonlinear effects are numerically investigated for various combinations of elastic spheres and rings in a standing wave: sphere-sphere, sphere-ring, and ring-ring. The results of this section can contribute to the explanation of the high effectiveness of some seed particle-based acoustic trapping techniques (Hammarström et al., 2012; Habibi & Neild, 2019; Habibi et al., 2020), which could be further enhanced by selecting the seed particles in accordance with our predictions.

### 4.2.1. Ring-Ring Interactions

#### 4.2.1.1. Rings Positioned in the Wave Direction

The primary and secondary forces between a pair of rings aligned in the wave direction with different sizes and materials are studied using the FEM model with the perturbation method described in section 2.1.1. As Fig 2.3. shows, the second particle is placed away from the pressure nodal plane, and the first particle is always located on the nodal plane. Fig 4.7 depicts

the primary acoustic radiation force determined for a single ring, the total force for a pair of rings, and the secondary force on a second particle. In this section, only the forces in the z-direction are reported due to the insignificant interactions in the r-direction.

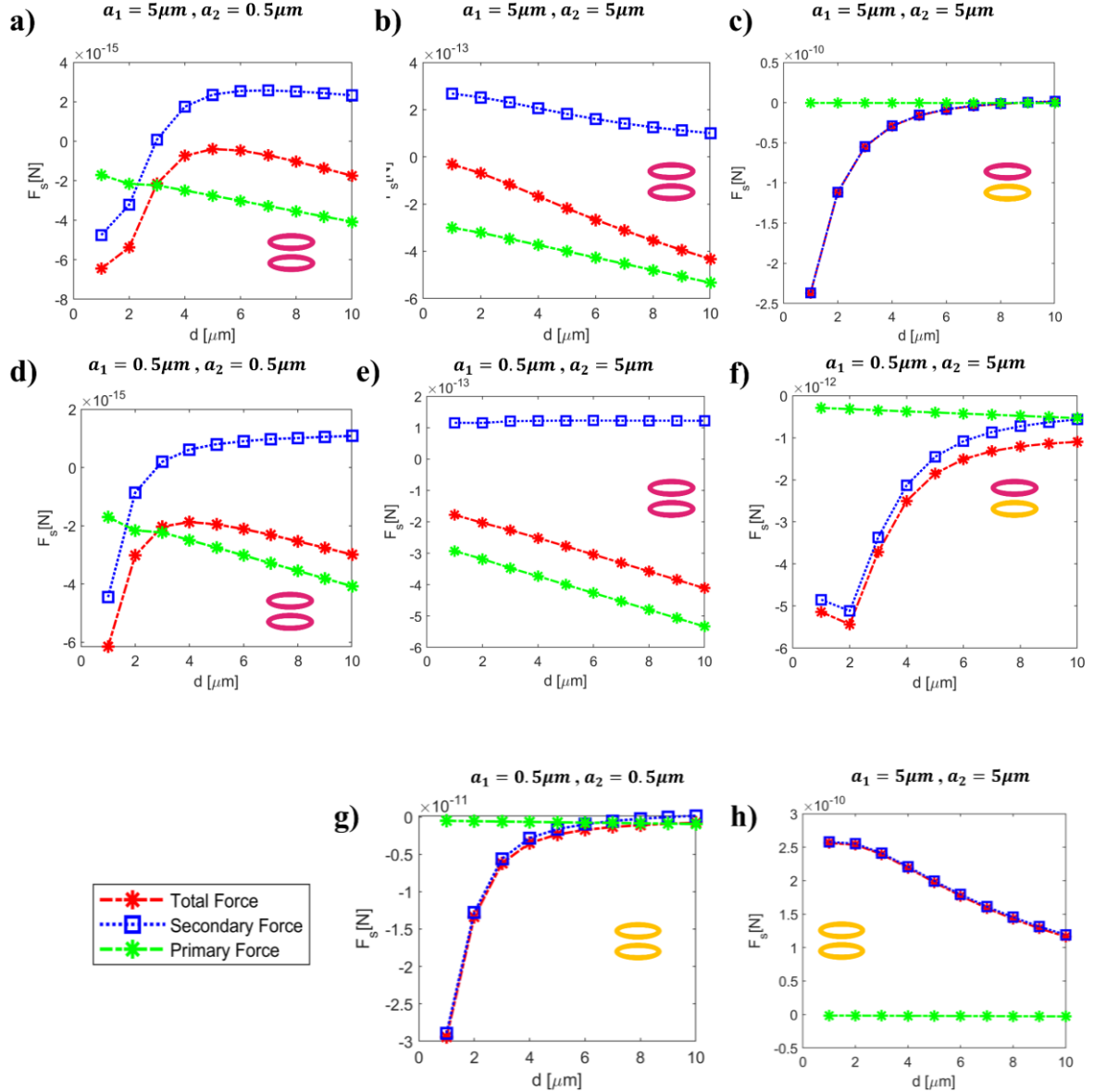


Fig 4.7. Acoustic radiation forces on particle 2 with respect to surface-to-surface distances,  $d$ , ( $1\mu\text{m}$  to  $10\mu\text{m}$ ) for various sizes of the rings at  $f = 500\text{KHz}$  and  $R = 10\mu\text{m}$  with various combination of  $a$  : (a,b,d,e) Polystyrene rings ,(c,f) First particle, a copper ring, centered at nodal plane; second particle is a polystyrene ring away from the nodal plane , (g,h) Copper rings (yellow rings represent the copper rings).

As expected, by increasing the distance between the rings, the primary forces increase due to the change in the position of the rings; however, the secondary force does not depend on the position of the rings, and it mostly depends on  $d$ . As seen in Fig 4.7, for different vertical distances,  $d$ , the change in the primary forces for a single ring is small compared to the

secondary forces when one of the rings in the domain is from a less compressible copper material (Fig 4.7c and 4.7h ). For polystyrene rings, significant differences between the secondary and total forces in Fig 4.7a-b and Fig 4.7d-e reveal that the primary force is dominant; the total and primary forces change in a consistent manner for both the small and large seed particles ( $a_1 = 0.5, 5\mu m$ ). However, for low inter-distances, secondary force dominates for the small second ring whenever the tiny particle is close to the second particle,  $a < \delta$  (Fig 4.7a and Fig 4.7d). It results in attractive force in low inter-distances and reversal of the force direction with increasing  $d$ , while in other cases, the secondary force is repelling. For large  $d$ , the addition of the second ring does not have any significant effect on the acoustic radiation force on the single ring, the effect is only significant for low  $d$  in polystyrene rings, and the total force aligns with the primary force. The interactions are more noticeable with adding copper ring in the domain even at larger  $d$  values and any size of the particles (Fig 4.7c and Fig 4.7f) due to variation in the acoustic contrast factors; also, the results show a dramatic increase in the total and secondary forces magnitude. Interestingly, as shown in Fig 4.7c and Fig 4.7f, adding the copper ring to the domain in contrast to the polystyrene ring (Fig 4.7a-b and Fig 4.7d-e), induces total forces that change close to the secondary forces, meaning that the secondary forces predominate the primary forces.

In our simulations, not only the first-order viscosity effect is considered, but also the contribution of the microstreaming around the ring is included. In addition to the viscosity, compressibility also influences the microstreaming, the magnitude of the acoustic radiation forces and the effective distance, the distance at which the impact of the second ring vanishes. Even in single-particle configurations, microstreaming for small particles ( $a < \delta$ ) can alter the direction of the ARF. Correspondingly, the microstreaming field, particularly around the particle producing the weaker microstreaming field, varies dramatically as the two particles move closer and may cause interparticle attraction. For example as shown in Fig 4.8-Fig 4.10, a  $0.5\mu m$  polystyrene ring experiences a maximum second field velocity of  $0.012\text{ mms}^{-1}$  and for a  $5\mu m$  polystyrene ring,  $\max(\|\langle v_2 \rangle\|) = 0.022\text{ mms}^{-1}$ , a  $0.5\mu m$  copper ring has  $\max(\|\langle v_2 \rangle\|) = 0.021\text{ mms}^{-1}$  and a  $5\mu m$  copper ring has  $\max(\|\langle v_2 \rangle\|) = 0.19\text{ mms}^{-1}$ .

Microstreaming around the surface of the particles at different inter-distances,  $d = 1, 3, 10\mu m$ , can be used to describe its effect on the direction and magnitude of the radiation forces. Fig 4.8a-c show the symmetric microstreaming of a  $5\mu m$  repelling pair of polystyrene rings at different inter-distances. As shown in Fig 4.8d-f for  $0.5\mu m$  polystyrene rings, at  $d = 1\mu m$ , the secondary force is attractive, and at  $d = 3, 10\mu m$  the secondary force changes its direction

to repulsive by variation of the streaming pattern.

For rings with equal  $a$  and  $R$  (Fig 4.8a-f), four small inner vortices are accompanied by four more giant vortices around them and another one in between the rings. As particles get close to one another (Fig 4.8b and Fig 4.8e), a pair of larger outer vortices changes to a pair of small vortices perpendicular to the wave direction. Fig 4.8c and Fig 4.8f show that inner vortices combine, and the vortices between the rings disappear as  $d$  decreases. In all cases shown in Fig 4.8a-f, the rings experience repulsive forces.

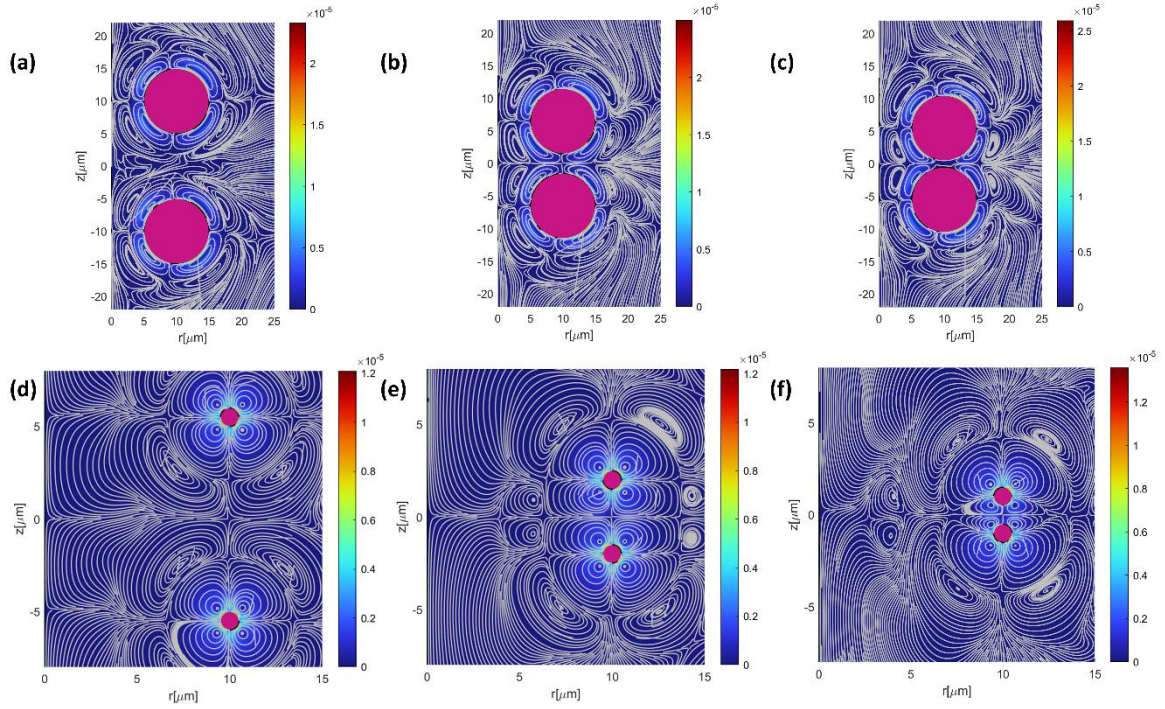


Fig 4.8. Streaming patterns and second-order velocity field are shown for polystyrene rings at  $f = 500\text{KHz}$  and  $R = 10\mu\text{m}$  with various inter-distances,  $d = 10, 3, 1\mu\text{m}$  respectively (a-c) for  $a_1 = a_2 = 5\mu\text{m}$ , (a-c) for  $a_1 = a_2 = 0.5\mu\text{m}$ .

Different sizes of particles lead to nonsymmetric streaming, as our model can capture precise inner vortices of various sizes, as seen in Fig 4.9. Because of this lack of symmetry, a transverse force creates a moment on the rings around their center, which causes the rings to realign themselves in a lateral arrangement. The stability results from the force between the rings being attractive at close ranges and repulsive at far ranges for large rings centered at the pressure node; however, a small ring at the pressure node led to the repulsive force to be in equilibrium (Fig 4.9d-f). The rings rotate around their common center and tend to realign themselves into the lateral configuration since the force acting on each one is transverse, equal, and opposite.

In contrast to equal-sized rings, the four inner vortices of smaller rings do not accompany the outer vortices in small rings, as shown in Fig 4.9. By approaching the larger ring, the vortices of a small ring disappear and shrink until they reach the inner vortices of the larger ring. Another vorticity appears around the larger ring due to reaching the smaller ring's vortices to the inner vortices around the larger ring. It can be seen in Fig 4.9c that getting inside the viscous boundary layer of the greater seed ring leads to an attractive secondary force.

The scaling laws of the principal acoustic radiation forces and the hydrodynamic drag force brought on by the induced acoustic streaming present the most significant obstacle when using acoustic standing wave technology for sub-micron particle manipulation. The fundamental acoustic radiation force rapidly declines relative to Stokes drag as particles get smaller, resulting in significant streaming.

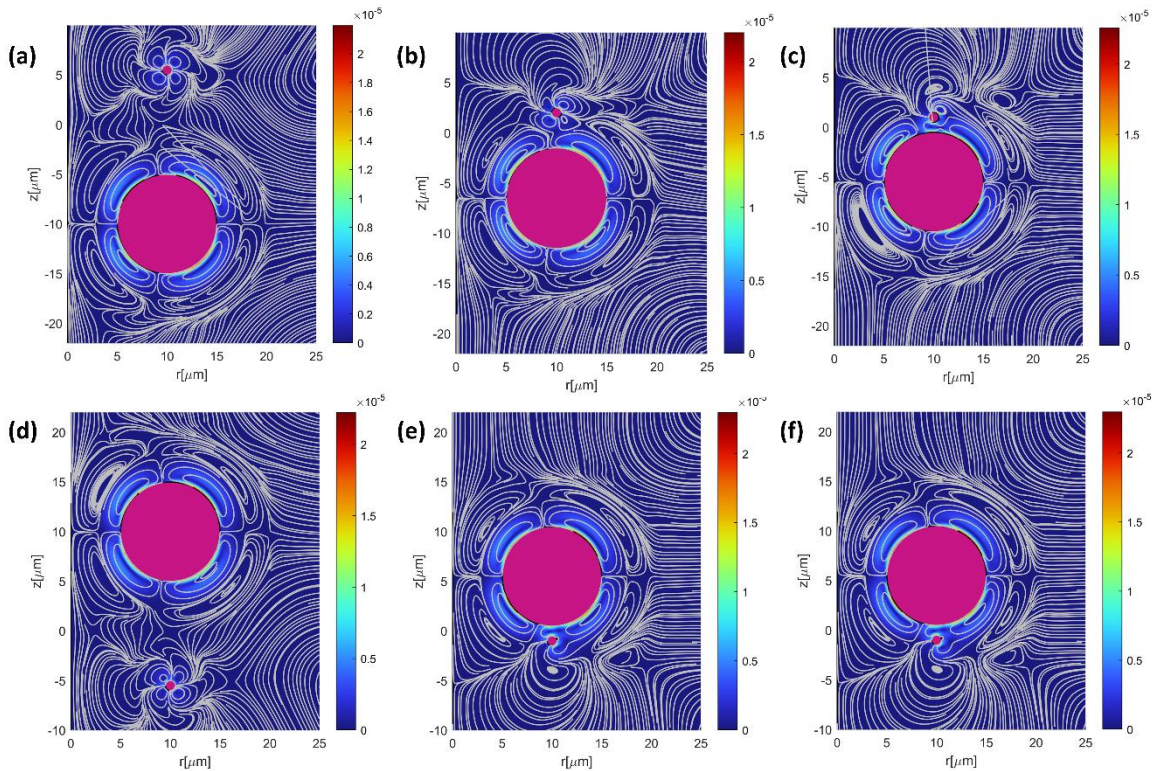


Fig 4.9. Streaming patterns and second-order velocity field are shown for polystyrene rings at  $f = 500\text{KHz}$  and  $R = 10\mu\text{m}$  with various inter-distances,  $d = 10, 3, 1 \mu\text{m}$  respectively (a-c) for  $a_1 = 5\mu\text{m}, a_2 = 0.5\mu\text{m}$ , (a-c) for  $a_1 = 0.5\mu\text{m}, a_2 = 5\mu\text{m}$ .

With changing one of the ring's materials to the less compressible copper, as the velocity field around the copper ring is stronger than the polystyrene, the streaming pattern stays symmetric around it. Its streaming influences the weaker particle's streamlines, especially when approaching the copper ring. The copper ring, even in smaller size due to its greater maximum velocity ( $\max(\|\langle v_2 \rangle\|) = 0.51\text{mms}^{-1}$ ), can influence the other particle's streamlines and

always results in attractive force. The symmetric streamlines of the copper ring encompass the second ring that is evident at close distances (Fig 4.10c and Fig 4.10f). As can be seen in Fig 4.9 and Fig 4.10, the streamlines around two rings are not a simple superposition of the streamlines, and it depends on the materials of the particles, their inter-distances, and their sizes.

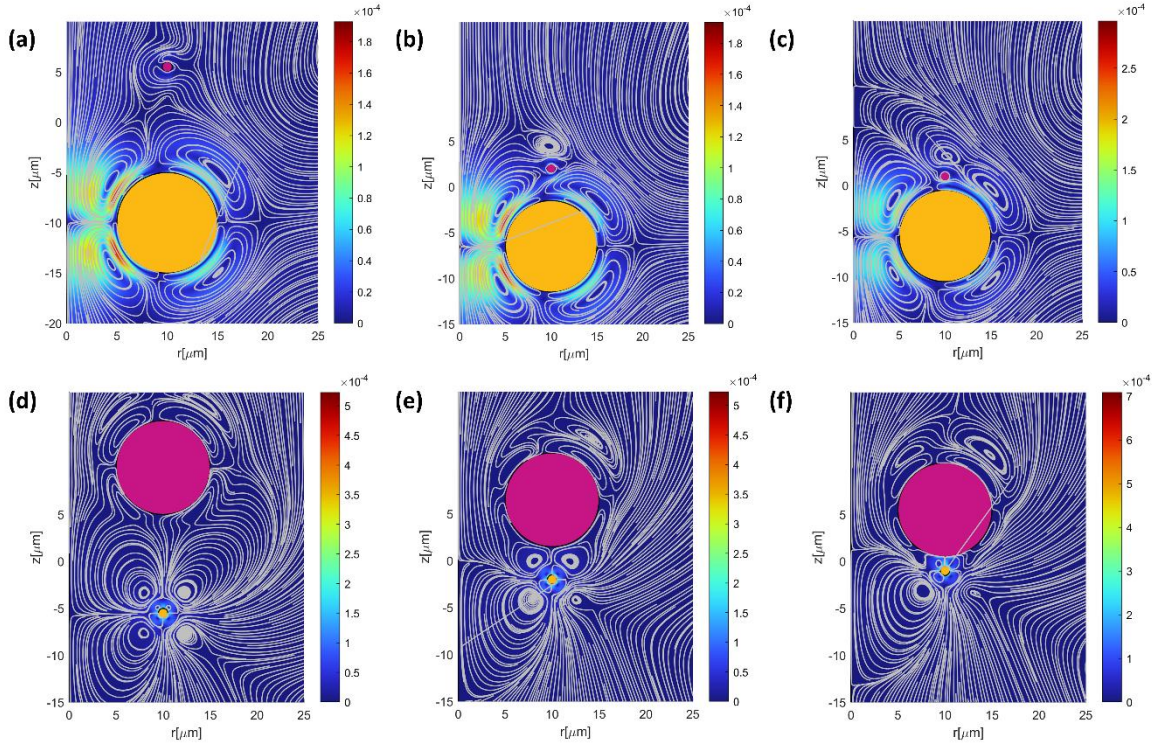


Fig 4.10. Streaming patterns and second-order velocity field are shown for polystyrene and copper rings at  $f = 500\text{KHz}$  and  $R = 10\mu\text{m}$  with various inter-distances,  $d = 10,3,1\mu\text{m}$  respectively (a-c) for  $a_1 = 5\mu\text{m}$  copper,  $a_2 = 0.5\mu\text{m}$  polystyrene, (a-c) for  $a_1 = 0.5\mu\text{m}$  copper,  $a_2 = 5\mu\text{m}$  polystyrene.

## 4.2.2. Sphere-Sphere Interactions

### 4.2.2.1. Spheres Positioned in the Wave Direction

For a better understanding of the primary and secondary forces and microstreaming that play a pivotal role in manipulating bacteria and nanoparticles based on interaction-forces techniques (Hammarström et al., 2012; Evander et al., 2015; Gutiérrez-Ramos et al., 2018), interaction forces between a pair of spheres are studied in this section. The forces between a

pair of polystyrene spheres aligned in the wave direction with different sizes are studied using the FEM model with the perturbation method, as described in section 2.1.1. The second particle is placed away from the pressure nodal plane, and the first particle is always located on the nodal plane. Fig 4.11. depicts the primary acoustic radiation force determined for a single sphere, the total force for a pair of spheres, and the secondary force on a second particle. Fig 4.11 shows that adding a particle in the pressure node can attract even larger spheres at close distances and repulsive at far distances; however, larger particles experience repulsive forces at all distances.

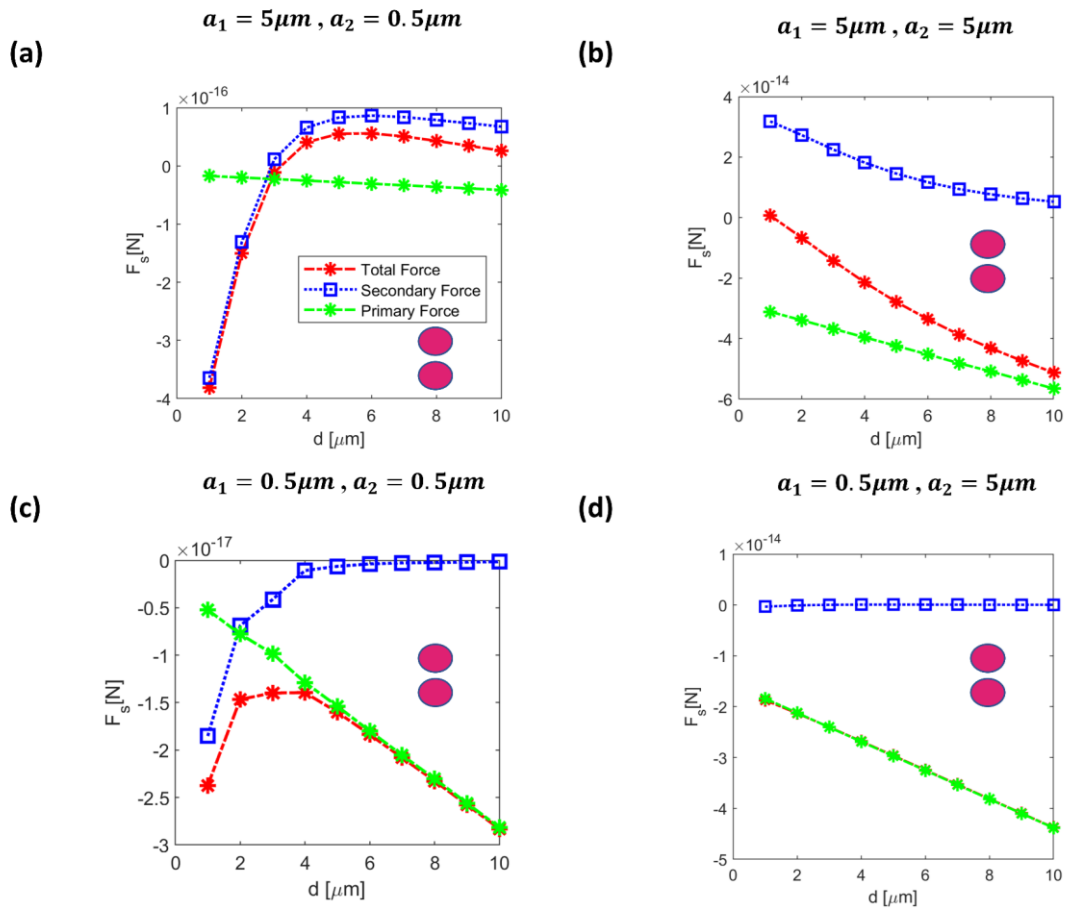


Fig 4.11. Acoustic radiation forces shown for polystyrene spheres at  $f = 500 \text{ KHz}$  and reported forces are forces on the second particle.

### 4.2.3. Ring-Sphere Interactions

#### 4.2.3.1. Ring and Spheres Positioned in the Wave Direction

The possibility of using rings as seed particles to induce the trapping of a spherical shape particle is examined here. A ring with  $a_1 = 0.5, 5 \mu\text{m}$  and  $R = 10 \mu\text{m}$  is used to capture the

sphere with  $a_2 = 0.5, 5 \mu\text{m}$ . As shown in Fig. 4.12a, the attractive force acts on the sphere by the larger ring that can be used for aggregation of cells and trapping purposes. However, Fig.4.12b reveals attractive force in close distances and switches to repulsive force in far distances that can be used where it is required to hold equal-sized particles in specific positions.

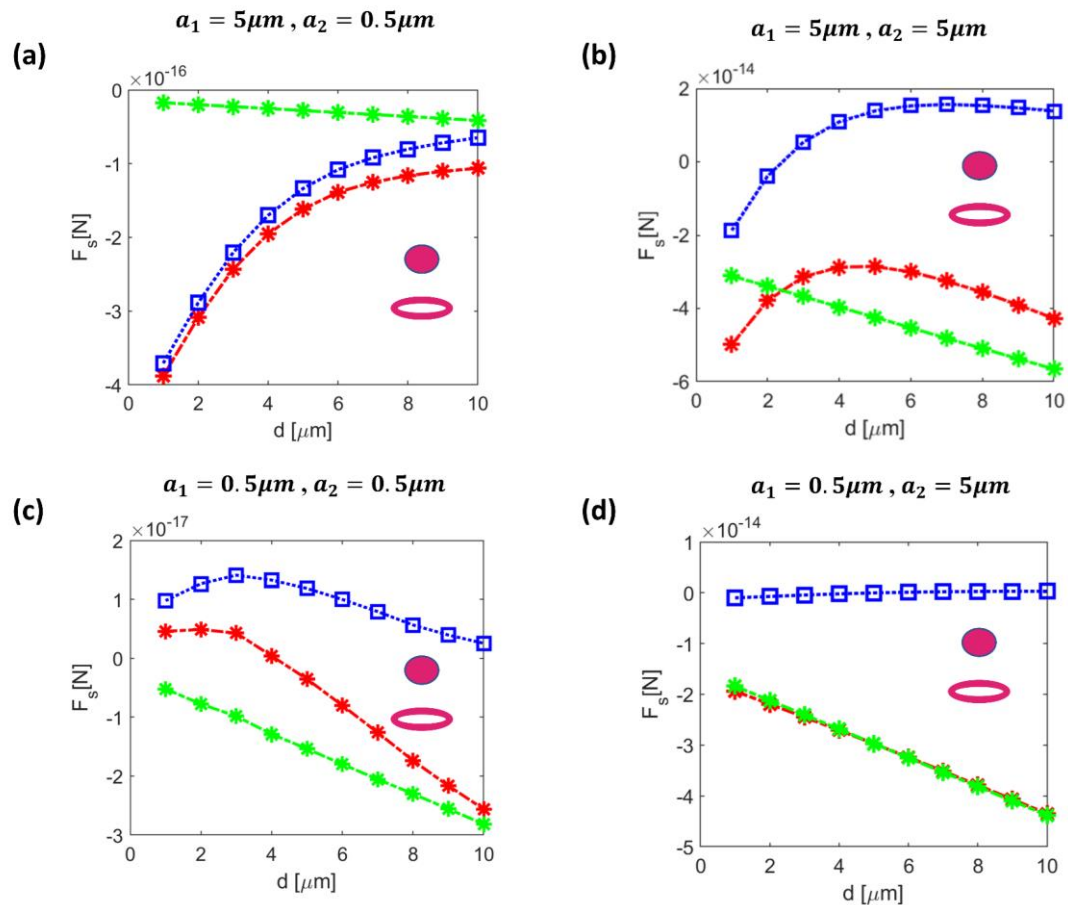


Fig 4.12. Acoustic radiation forces shown for polystyrene sphere and ring at  $f = 500\text{KHz}$  and (first particle is ring with  $R = 10\mu\text{m}$  and second particle is sphere): reported forces are forces on the second particle.

As in the previous section, the material dependency of the secondary forces is examined to find the best seed particle under the condition of using different shapes of particles; here, the copper ring is added to the fluid domain including a polystyrene sphere. Fig 4.13 shows that the total force tends to move the polystyrene sphere in the opposing (negative). The dominant role of the secondary force in contributing to the total acoustic forces acting on the polystyrene sphere is the first salient characteristic of the plots in Fig.4.13. A packed bed may suffer

significantly from such repellent interparticle effects. However, the framework provided by another study (Silva et al., 2019) will help determine the frequencies at which a packed bed of seed particles is likely to be stable.

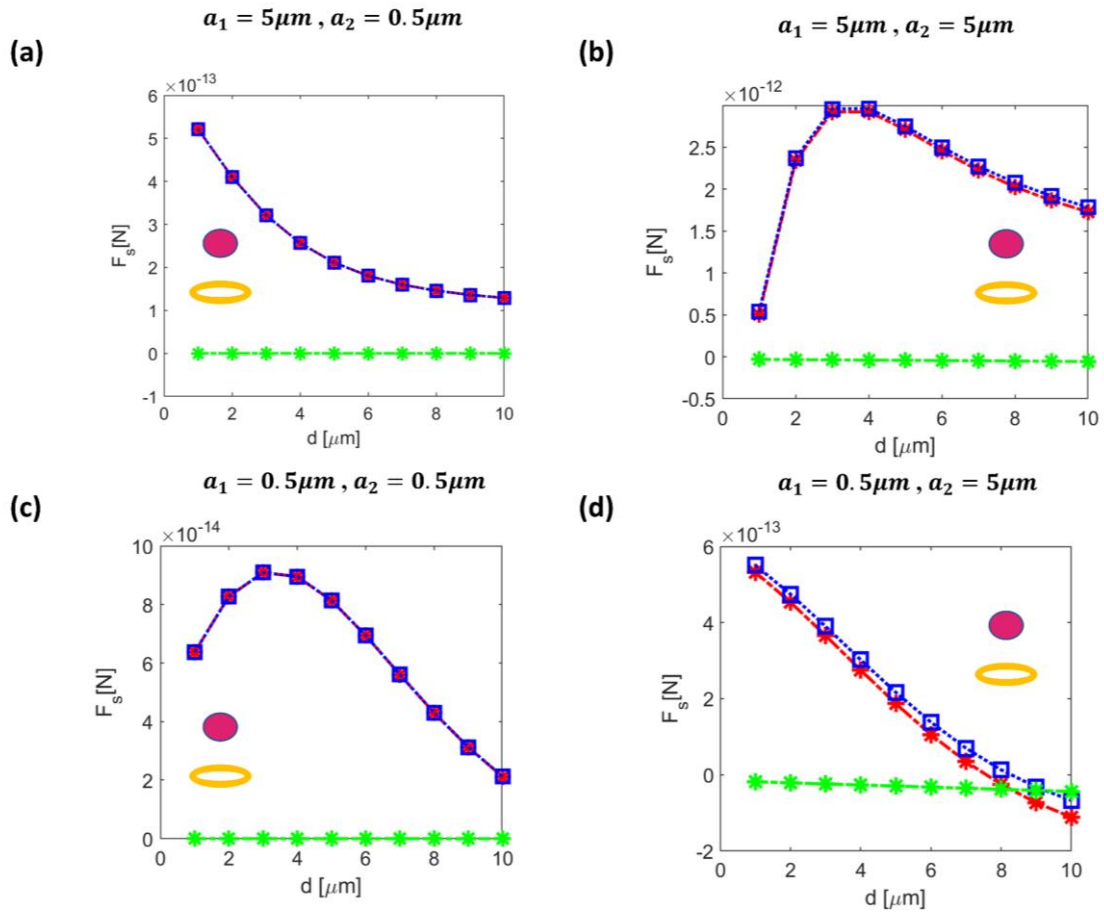


Fig 4.13. Acoustic radiation forces shown for polystyrene sphere and copper ring at  $f = 500\text{KHz}$  and (first particle is ring with  $R = 10\mu\text{m}$  and second particle is sphere).

Adding the copper ring to the fluid domain results in extra radiation forces on the polystyrene sphere, a few scales greater than the primary radiation force, also Fig.4.13 implies that secondary forces dominate the ARF in all sizes for the copper ring. Streamline patterns of the equal-sized particles in Fig 4.14 (the radius of the sphere is the same as the minor radius of the ring,  $a = 5\mu\text{m}$ ) show that the streamline of the copper ring dominates the streamline pattern in both small and large particles. Fig 4.14c shows the streamline pattern around a copper ring and a polystyrene sphere at a close distance, in which the sphere can be moved with the ring's streamline in outward directions. These results arose from both the Stokes drag and the

radiation forces. In contrast to Stokes drag, which scales with particle radius, the primary radiation force scales with particle volume, as depicted in section 3.2.

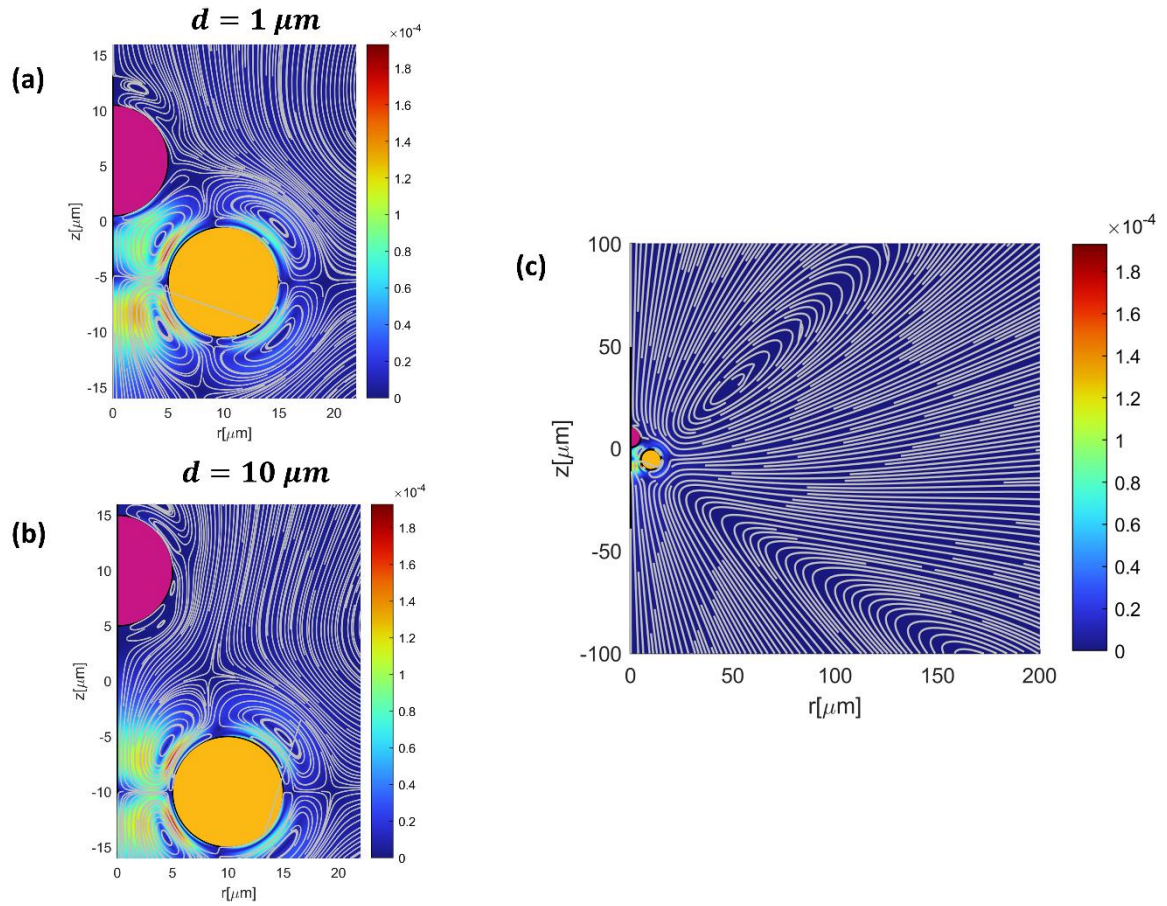


Fig 4.14. Streamline patterns for polystyrene sphere and copper ring in water subjected to a standing wave at  $f = 500\text{KHz}$  at different inter-distances: a)  $d = 1\mu\text{m}$  b)  $d = 10 \mu\text{m}$  c)  $d = 1 \mu\text{m}$  ; first particle is a ring with  $a = 5\mu\text{m}$  and  $R = 10\mu\text{m}$ , and second particle is a sphere with the radius of  $a = 5\mu\text{m}$ .

## 5. Conclusions

Manipulation of single and multiple biological objects using ultrasound waves has attracted a great deal of interest in the fields of biology, chemistry, physics, and medicine. This technique offers the potential for the precise, contact-free, and noninvasive manner of cell manipulation in various applications, including cellular analysis, drug deliveries, disease prognosis, and medical therapies. Since biological cells can be in any size, shape, or orientation, there is a need for a more adaptable and reliable numerical model for predicting acoustic radiation force and torque. Motivated by this, the numerical simulations of this thesis have provided valuable insights into the underlying physics and have enhanced the potential of using acoustic radiation forces and torques for ring-shaped particle manipulation and separation in various applications such as biomedical engineering and materials science. In conclusion, this research investigated the effects of geometry, position, direction, and physical properties on the acoustic radiation forces (ARFs) and torques (ARTs) induced on micro rings in a standing acoustic field in both viscous and inviscid fluids. ARFs and ARTs are calculated based on the perturbation method using the tensor integral approach, in which the first and second-order fields are obtained from the finite element method (FEM).

Similar to the force on spherical particles in both inviscid and viscous fluids, the ARF is proportional to the volume of the ring and reaches its maximum when the ring is  $\lambda/8$  away from the pressure nodes. Varying the orientation of the ring does not significantly affect the ARF in both inviscid and viscous fluids. On the other hand, ART in both inviscid and viscous fluids is always negative, restoring the ring to the horizontal alignment for rings positioned in the plane standing wave at low rotation angles. However, the ART is positive, aligning the ring vertically for rings positioned close to pressure antinodes when the rings are rotated with higher rotation angles ( $40^\circ < \theta < 80^\circ$ ). In both inviscid and viscous fluids cases, maximum torques occur whereby acoustic radiation force is minimum at the pressure nodes. Viscosity varies the effective range of  $\theta$  and zero-torque regions, obtaining these regions can have a crucial role in the selective manipulating of particles.

Indeed, the findings show that ring position and alignment in a standing wave can affect the magnitude and direction of the ARF and ART acting on the ring, implying that ring position

in a standing wave and its alignment should be adjusted according to desired acoustophoretic purposes in both viscous and inviscid fluids. Furthermore, with increasing the viscosity of the fluid medium, the trend of variation of the ART varies; highly viscous fluids cause the maximum ART to occur at higher rotation angles, tending to align the ring in the wave direction; however, slightly viscous fluids lead to maximum restorative torque at low rotation angles. Moreover, heavier rings with respect to their surrounding fluid experience maximum restorative torques at  $\theta = 45^\circ$ , and more robust acoustic radiation forces at low  $\theta$ , the proper rotation angle can be picked concerning the manipulation aim.

The ART tends to align the rings with respect to the plane waves depending on the geometric and physical factors. The ring's stable alignment could be either horizontal or vertical. For example, in the inviscid fluid for  $\Delta z = 0$ , the negative ART tries to keep rings with orientations of  $\theta > 35^\circ$  horizontally and vertically aligned otherwise ( $\tau^{rad} > 0$  for  $35^\circ < \theta < 90^\circ$ ), whereas for  $\Delta z = \lambda/8$  the ring alignment is always horizontal. Resonance behavior of the ring in distinct configurations leads to tremendous ART due to dependency of the ART on local force distributions; The resonance behavior is also revealed in the torque findings in a viscous fluid; however, at a bit different value from the inviscid study.

The ARF on a ring is also sensitive to the acoustophoretic contrast factor, attractive ( $F^{rad} < 0$ ) for  $\phi < 0$  and repulsive otherwise. On the other hand, the ART does not change sign with  $\phi$  for the configurations examined here, but ART reaches the minimum values at a small positive contrast factor. Also, the FEM results are compared to those of a chain-of-spheres model (COS), a reduced-order model that predicts the ARF particularly well for soft materials. However, the COS approach does not account for the effects of self-scattering, which results in inaccurate torque predictions. Separate FEM simulations for a segmented ring show the importance of local forces. It has been found that the elastic behavior of the solid, rather than self-scattering, dominates local forces for the polystyrene ring. On the other hand, self-scattering is crucial to the local force in the case of the less compressible ring. Comparing the three materials reveals that compressibility increases absorption of the scattering pressure gradients, and local forces are affected by the compressibility factor more than the position and self-scattering. Finally, the secondary acoustic radiation forces and microstreaming revealed that using a ring in a pressure node can lead to significant attractive force in the wave direction in specific combinations of ring size and material, applicable to attract even other shapes of particles.

Acoustophoretic manipulation and reorientation of ring-like micro filaments and other non-

spherical thin entities are expected to benefit from the study's overall conclusions. Our analysis demonstrates that the overall ART on the structure is significantly influenced by the self-scattering of acoustic waves and the bending of the thin rods. These results may be used to determine the orientation of the structure at equilibrium as well as orientational instabilities under resonance. Predictions may be used to rotate and manipulate these structures in a non-contact way without causing any damage, which is very helpful when orienting a biological sample for imaging, trapping, or separating. Given the widespread use of acoustic fields in biomedicine, these applications can be successfully implemented to achieve efficient, robust, and selective manipulations. The chain-of-spheres method is beneficial for calculating acoustic radiation forces; however, it needs to be improved by considering internal stresses and acoustic wave self-scattering to provide accurate torque predictions.

### **5.1. Future Work**

The findings of this dissertation have significant potential in many applications, such as in the biomedical field for cell manipulation, in the oil and gas industry for pipeline inspection, and material science for non-destructive testing. The following are some possible avenues of future work in this field.

The thesis has focused on theoretical calculations and numerical simulations to determine the primary and secondary acoustic radiation forces and acoustic radiation torques on elastic rings. Future work could involve fabricating micro rings, designing and conducting experiments to validate the findings and assessing the accuracy of the theoretical and numerical methods.

Acoustic trapping is used in various fields to manipulate and move particles using acoustic radiation forces and torques. This thesis has explored the potential for using primary and secondary acoustic radiation forces on elastic rings for acoustic trapping. Future work could extend the work and focus on optimizing the conditions for acoustic trapping of elastic rings or different shapes of particles, such as the acoustic frequency and amplitude, ring size and material, and fluid properties. Future work could involve exploring potential applications further and identifying new areas where this technique could be helpful. For example, in biomedicine, acoustic radiation force could be used to manipulate and sort cells or to deliver drugs to specific locations in the body.

The possibility of using multiple rings in acoustic manipulation to trap or separate other

particles can be explored. In some cases, more than a single ring may be required to achieve the desired manipulation accuracy or efficiency level. Using multiple rings can provide more degrees of freedom and flexibility in controlling the target object's position, orientation, and velocity. The interaction between multiple rings can also give rise to interesting collective phenomena, such as self-assembly and pattern formation. Investigating the multi-ring acoustic manipulation system can open up new possibilities for advanced applications in various fields. Finally, the thesis has focused on elastic rings as the geometry of interest. Future work could extend the investigation to other geometries, such as rings with different shapes of cross-sections, ribbons, or plates, and explore the primary and secondary acoustic radiation force on these geometries. This could provide a more comprehensive understanding of the behavior of elastic objects under the influence of acoustic radiation forces and torques. Further modal analysis and investigating the particle's mechanical response to the acoustic field, affecting its resonance frequency and damping, can help to achieve more efficient and selective separation and manipulation. The geometrical parameters can also influence the magnitude and direction of the radiation force and torque, as well as the mode of vibration of the particle. A systematic study of the radiation force and torque behaviors on rings can provide valuable insights into the design and optimization of acoustic manipulation devices.

## BIBLIOGRAPHY

- Alloul, M., B. Dollet, O. Stephan, E. Bossy, C. Quilliet and P. Marmottant (2022). "Acoustic Resonance Frequencies of Underwater Toroidal Bubbles." Physical Review Letters **129**(13): 134501.
- Altay, R., A. K. Sadaghiani, M. I. Sevgen, A. Şişman and A. Koşar (2020). "Numerical and Experimental Studies on the Effect of Surface Roughness and Ultrasonic Frequency on Bubble Dynamics in Acoustic Cavitation." Energies **13**(5): 1126.
- Baasch, T., A. Pavlic and J. Dual (2019). "Acoustic radiation force acting on a heavy particle in a standing wave can be dominated by the acoustic microstreaming." Physical Review E **100**(6): 061102.
- Bjerknes, V. (1906). Fields of force; supplementary lectures, applications to meteorology; a course of lectures in mathematical physics delivered December 1 to 23, 1905. New York, The Columbia university press; [etc., etc.].
- Bruus, H. (2012). "Acoustofluidics 7: The acoustic radiation force on small particles." Lab on a Chip **12**(6): 1014-1021.
- Cai, F., L. Meng, C. Jiang, Y. Pan and H. Zheng (2010). "Computation of the acoustic radiation force using the finite-difference time-domain method." J Acoust Soc Am **128**(4): 1617-1622.
- Cai, H., Z. Wu, Z. Ao, A. Nunez, B. Chen, L. Jiang, M. Bondesson and F. Guo (2020). "Trapping cell spheroids and organoids using digital acoustofluidics." Biofabrication **12**(3): 035025.
- Caldag, H. O. and S. Yesilyurt (2020). "Acoustic radiation forces on magnetically actuated helical swimmers." Physics of Fluids **32**(9): 092012.
- Cao, Q., Q. Fan, Q. Chen, C. Liu, X. Han and L. Li (2020). "Recent advances in manipulation of micro-and nano-objects with magnetic fields at small scales." Materials Horizons **7**(3): 638-666.
- Chen, Z., Z. Pei, X. Zhao, J. Zhang, J. Wei and N. Hao (2022). "Acoustic microreactors for chemical engineering." Chemical Engineering Journal **433**: 133258.
- Coakley, W. T., D. W. Bardsley, M. A. Grundy, F. Zamani and D. J. Clarke (1989). "Cell manipulation in ultrasonic standing wave fields." Journal of Chemical Technology & Biotechnology **44**(1): 43-62.
- COMSOL COMSOL Multiphysics Reference Manual.
- Crum, L. A. (1975). "Bjerknes forces on bubbles in a stationary sound field." The Journal of the Acoustical Society of America **57**(6): 1363-1370.

- Danilov, S. (1985). "Average force acting on a small sphere in a traveling-wave field in a viscous fluid." Akusticheski Zhurnal **31**: 45-49.
- Danilov, S. (1986). "The mean force acting on a small body in an axisymmetric sound field in a real medium." Fluid Dynamics **21**(5): 812-820.
- Deshmukh, S., Z. Brzozka, T. Laurell and P. Augustsson (2014). "Acoustic radiation forces at liquid interfaces impact the performance of acoustophoresis." Lab on a Chip **14**(17): 3394-3400.
- Doinikov, A. (1994). "Acoustic radiation pressure on a rigid sphere in a viscous fluid." Proceedings of the Royal Society of London. Series A: Mathematical and Physical Sciences **447**(1931): 447-466.
- Doinikov, A. and S. Zavtrak (1995). "On the mutual interaction of two gas bubbles in a sound field." Physics of Fluids **7**(8): 1923-1930.
- Doinikov, A. and S. Zavtrak (1996). "Interaction force between a bubble and a solid particle in a sound field." Ultrasonics **34**(8): 807-815.
- Doinikov, A. A. (1994). "Acoustic radiation pressure on a compressible sphere in a viscous fluid." Journal of Fluid Mechanics **267**: 1-22.
- Doinikov, A. A. (1996). "Mutual interaction between a bubble and a drop in a sound field." The Journal of the Acoustical Society of America **99**(6): 3373-3379.
- Doinikov, A. A. (1997). "Acoustic radiation force on a spherical particle in a viscous heat-conducting fluid. I. General formula." The Journal of the Acoustical Society of America **101**(2): 713-721.
- Doinikov, A. A. (1997). "Acoustic radiation force on a spherical particle in a viscous heat-conducting fluid. II. Force on a rigid sphere." The Journal of the Acoustical Society of America **101**(2): 722-730.
- Doinikov, A. A. (1997). "Acoustic radiation force on a spherical particle in a viscous heat-conducting fluid. III. Force on a liquid drop." The Journal of the Acoustical Society of America **101**(2): 731-740.
- Doinikov, A. A. (1999). "Bjerknes forces between two bubbles in a viscous fluid." The Journal of the Acoustical Society of America **106**(6): 3305-3312.
- Doinikov, A. A. (2002). "Viscous effects on the interaction force between two small gas bubbles in a weak acoustic field." The Journal of the Acoustical Society of America **111**(4): 1602-1609.
- Doinikov, A. A. (2003). "Acoustic radiation forces: Classical theory and recent advances." Recent research developments in acoustics **1**: 39-67.

Doinikov, A. A., P. Thibault and P. Marmottant (2017). "Acoustic streaming in a microfluidic channel with a reflector: Case of a standing wave generated by two counterpropagating leaky surface waves." Physical Review E **96**(1): 013101.

Egbo, M. K. (2021). "A fundamental review on composite materials and some of their applications in biomedical engineering." Journal of King Saud University - Engineering Sciences **33**(8): 557-568.

Embleton, T. (1962). "Mutual interaction between two spheres in a plane sound field." The Journal of the Acoustical Society of America **34**(11): 1714-1720.

Evander, M., O. Gidlöf, B. Olde, D. Erlinge and T. Laurell (2015). "Non-contact acoustic capture of microparticles from small plasma volumes." Lab on a Chip **15**(12): 2588-2596.

Fakhfour, A., C. Devendran, D. J. Collins, Y. Ai and A. Neild (2016). "Virtual membrane for filtration of particles using surface acoustic waves (SAW)." Lab on a Chip **16**(18): 3515-3523.

Fan, Q., W. Hu and A. T. Ohta (2014). "Laser-induced microbubble poration of localized single cells." Lab on a Chip **14**(9): 1572-1578.

Friend, J. and L. Y. Yeo (2011). "Microscale acoustofluidics: Microfluidics driven via acoustics and ultrasonics." Reviews of Modern Physics **83**(2): 647.

Fu, Q., Y. Zhang, T. Huang, Y. Liang and Y. Liu (2021). "Measurement of cell compressibility changes during epithelial–mesenchymal transition based on acoustofluidic microdevice." Biomicrofluidics **15**(6): 064101.

Gao, Y., M. Wu, Y. Lin and J. Xu (2020). "Acoustic Microfluidic Separation Techniques and Bioapplications: A Review." Micromachines **11**(10): 921.

Garbin, A., I. Leibacher, P. Hahn, H. L. Ferrand, A. Studart and J. Dual (2015). "Acoustophoresis of disk-shaped microparticles: A numerical and experimental study of acoustic radiation forces and torques." The Journal of the Acoustical Society of America **138**(5): 2759-2769.

Garbin, A., I. Leibacher, P. Hahn, H. Le Ferrand, A. Studart and J. Dual (2015). "Acoustophoresis of disk-shaped microparticles: A numerical and experimental study of acoustic radiation forces and torques." J Acoust Soc Am **138**(5): 2759-2769.

Garcia-Sabaté, A., A. Castro, M. Hoyos and R. González-Cinca (2014). "Experimental study on inter-particle acoustic forces." The Journal of the Acoustical Society of America **135**(3): 1056-1063.

Givoli, D. and B. Neta (2003). "High-order non-reflecting boundary scheme for time-dependent waves." Journal of Computational Physics **186**(1): 24-46.

Glynn-Jones, P., R. J. Boltryk, M. Hill, N. R. Harris and P. Baclet (2009). "Robust acoustic

particle manipulation: A thin-reflector design for moving particles to a surface." The Journal of the Acoustical Society of America **126**(3): EL75-EL79.

Glynne-Jones, P., P. P. Mishra, R. J. Boltryk and M. Hill (2013). "Efficient finite element modeling of radiation forces on elastic particles of arbitrary size and geometry." The Journal of the Acoustical Society of America **133**(4): 1885-1893.

Gong, Z. and M. Baudoin (2021). "Three-Dimensional Trapping and Dynamic Axial Manipulation with Frequency-Tuned Spiraling Acoustical Tweezers: A Theoretical Study." Physical Review Applied **16**(2): 024034.

Gor'kov, L. P. (1962). "On the Forces Acting on a Small Particle in an Acoustical Field in an Ideal Fluid." Soviet Physics Doklady **6**: 773.

Graff, K. F. (2012). Wave motion in elastic solids, Courier Corporation.

Grinenko, A., P. D. Wilcox, C. R. Courtney and B. W. Drinkwater (2012). "Acoustic radiation force analysis using finite difference time domain method." J Acoust Soc Am **131**(5): 3664-3670.

Gruziel-Słomka, M., P. Kondratiuk, P. Szymczak and M. L. Ekiel-Jeżewska (2019). "Stokesian dynamics of sedimenting elastic rings." Soft Matter **15**(36): 7262-7274.

Gutiérrez-Ramos, S., M. Hoyos and J. C. Ruiz-Suárez (2018). "Induced clustering of Escherichia coli by acoustic fields." Scientific Reports **8**(1): 4668.

Haake, A., A. Neild, G. Radziwill and J. Dual (2005). "Positioning, displacement, and localization of cells using ultrasonic forces." Biotechnology and Bioengineering **92**(1): 8-14.

Habibi, R., V. He, S. Ghavamian, A. de Marco, T.-H. Lee, M.-I. Aguilar, D. Zhu, R. Lim and A. Neild (2020). "Exosome trapping and enrichment using a sound wave activated nano-sieve (SWANS)." Lab on a Chip **20**(19): 3633-3643.

Habibi, R. and A. Neild (2019). "Sound wave activated nano-sieve (SWANS) for enrichment of nanoparticles." Lab on a Chip **19**(18): 3032-3044.

Hahn, P., I. Leibacher, T. Baasch and J. Dual (2015). "Numerical simulation of acoustofluidic manipulation by radiation forces and acoustic streaming for complex particles." Lab on a Chip **15**(22): 4302-4313.

Hammarström, B., T. Laurell and J. Nilsson (2012). "Seed particle-enabled acoustic trapping of bacteria and nanoparticles in continuous flow systems." Lab on a Chip **12**(21): 4296-4304.

Hasegawa, T. (1979). "Acoustic radiation force on a sphere in a quasistationary wave field— theory." The Journal of the Acoustical Society of America **65**(1): 32-40.

Hasegawa, T. and K. Yosioka (1969). "Acoustic-Radiation Force on a Solid Elastic Sphere." The Journal of the Acoustical Society of America **46**(5B): 1139-1143.

- Haydock, D. (2005). "Lattice Boltzmann simulations of the time-averaged forces on a cylinder in a sound field." Journal of Physics A: Mathematical and General **38**(15): 3265.
- Hoque, S. Z. and A. K. Sen (2020). "Interparticle acoustic radiation force between a pair of spherical particles in a liquid exposed to a standing bulk acoustic wave." Physics of Fluids **32**(7): 072004.
- Huang, P.-H., Y. Xie, D. Ahmed, J. Rufo, N. Nama, Y. Chen, C. Y. Chan and T. J. Huang (2013). "An acoustofluidic micromixer based on oscillating sidewall sharp-edges." Lab on a Chip **13**(19): 3847-3852.
- Hultström, J., O. Manneberg, K. Dopf, H. M. Hertz, H. Brismar and M. Wiklund (2007). "Proliferation and viability of adherent cells manipulated by standing-wave ultrasound in a microfluidic chip." Ultrasound in Medicine & Biology **33**(1): 145-151.
- Jeger-Madiot, N., X. Mousset, C. Dupuis, L. Rabiet, M. Hoyos, J.-M. Peyrin and J.-L. Aider (2022). "Controlling the force and the position of acoustic traps with a tunable acoustofluidic chip: Application to spheroid manipulations." The Journal of the Acoustical Society of America **151**(6): 4165-4179.
- Johnson, K. A., H. R. Vormohr, A. A. Doinikov, A. Bouakaz, C. W. Shields, G. P. López and P. A. Dayton (2016). "Experimental verification of theoretical equations for acoustic radiation force on compressible spherical particles in traveling waves." Physical Review E **93**(5): 053109.
- Jr., J. J. F. (1951). "Sound Scattering by Solid Cylinders and Spheres." The Journal of the Acoustical Society of America **23**(4): 405-418.
- JunáHuang, T. (2014). "A reliable and programmable acoustofluidic pump powered by oscillating sharp-edge structures." Lab on a Chip **14**(22): 4319-4323.
- Karlsen, J. T. and H. Bruus (2015). "Forces acting on a small particle in an acoustical field in a thermoviscous fluid." Phys Rev E Stat Nonlin Soft Matter Phys **92**(4): 043010.
- King, L. V. (1934). "On the acoustic radiation pressure on spheres." Proceedings of the Royal Society of London. Series A-Mathematical and Physical Sciences **147**(861): 212-240.
- King, L. V. (1935). "On the acoustic radiation pressure on circular discs: Inertia and diffraction corrections." Proceedings of the Royal Society of London. Series A - Mathematical and Physical Sciences **153**(878): 1-16.
- Krasnitskii, S., A. Trofimov, E. Radi and I. Sevestianov (2019). "Effect of a rigid toroidal inhomogeneity on the elastic properties of a composite." Mathematics and Mechanics of Solids **24**(4): 1129-1146.
- Kummer, M. P., J. J. Abbott, B. E. Kratochvil, R. Borer, A. Sengul and B. J. Nelson (2010).

"OctoMag: An electromagnetic system for 5-DOF wireless micromanipulation." IEEE Transactions on Robotics **26**(6): 1006-1017.

Kvåle Løvmo, M., B. Pressl, G. Thalhammer and M. Ritsch-Marte (2021). "Controlled orientation and sustained rotation of biological samples in a sono-optical microfluidic device." Lab on a Chip **21**(8): 1563-1578.

Laurell, T., F. Petersson and A. Nilsson (2007). "Chip integrated strategies for acoustic separation and manipulation of cells and particles." Chemical Society Reviews **36**(3): 492-506.

Leão-Neto, J. P., M. Hoyos, J.-L. Aider and G. T. Silva (2021). "Acoustic radiation force and torque on spheroidal particles in an ideal cylindrical chamber." The Journal of the Acoustical Society of America **149**(1): 285-295.

Lenshof, A., M. Evander, T. Laurell and J. Nilsson (2012). "Acoustofluidics 5: Building microfluidic acoustic resonators." Lab on a Chip **12**(4): 684-695.

Li, S., F. Guo, Y. Chen, X. Ding, P. Li, L. Wang, C. E. Cameron and T. J. Huang (2014). "Standing surface acoustic wave based cell coculture." Anal Chem **86**(19): 9853-9859.

Li, Y., X. Liu, Q. Huang, A. T. Ohta and T. Arai (2021). "Bubbles in microfluidics: an all-purpose tool for micromanipulation." Lab on a Chip **21**(6): 1016-1035.

Li, Z., D. Wang, C. Fei, Z. Qiu, C. Hou, R. Wu, D. Li, Q. Zhang, D. Chen and Z. Chen (2021). "The forbidden band and size selectivity of acoustic radiation force trapping." Iscience **24**(1): 101988.

Mallea, R. T., A. Bolopion, J.-C. Beugnot, P. Lambert and M. Gauthier (2018). "Closed-loop particle motion control using laser-induced thermocapillary convective flows at the fluid/gas interface at micrometric scale." IEEE/ASME transactions on mechatronics **23**(4): 1543-1554.

Manjare, M., B. Yang and Y.-P. Zhao (2013). "Bubble-propelled microjets: Model and experiment." The Journal of Physical Chemistry C **117**(9): 4657-4665.

Marston, P. L., W. Wei and D. B. Thiessen (2006). Acoustic Radiation Force On Elliptical Cylinders And Spheroidal Objects In Low Frequency Standing Waves. Innovations in Nonlinear Acoustics.

Mitri, F. G. (2005). "Theoretical calculation of the modulated acoustic radiation force on spheres and cylinders in a standing plane wave-field." Physica D: Nonlinear Phenomena **212**(1): 66-81.

Mitri, F. G. (2006). "Theoretical and experimental determination of the acoustic radiation force acting on an elastic cylinder in a plane progressive wave—far-field derivation approach." New Journal of Physics **8**(8): 138-138.

- Mitri, F. G. (2008). "Acoustic radiation force on a sphere in standing and quasi-standing zero-order Bessel beam tweezers." Annals of Physics **323**(7): 1604-1620.
- Mitri, F. G. (2009). "Acoustic radiation force of high-order Bessel beam standing wave tweezers on a rigid sphere." Ultrasonics **49**(8): 794-798.
- Mitri, F. G. (2010). "Transition from progressive to quasi-standing waves behavior of the radiation force of acoustic waves—Example of a high-order Bessel beam on a rigid sphere." Journal of Sound and Vibration **329**(16): 3319-3324.
- Mitri, F. G. (2015). "Acoustic radiation force on oblate and prolate spheroids in Bessel beams." Wave Motion **57**: 231-238.
- Mitri, F. G. (2016). "Acoustic radiation force and spin torque on a viscoelastic cylinder in a quasi-Gaussian cylindrically-focused beam with arbitrary incidence in a non-viscous fluid." Wave Motion **66**: 31-44.
- Mohapatra, A. R., S. Sepehrirahnama and K.-M. Lim (2018). "Experimental measurement of interparticle acoustic radiation force in the Rayleigh limit." Physical Review E **97**(5): 053105.
- Mousavi, S. M., G. Gompper and R. G. Winkler (2019). "Active Brownian ring polymers." The Journal of Chemical Physics **150**(6): 064913.
- Muller, P. B., R. Barnkob, M. J. H. Jensen and H. Bruus (2012). "A numerical study of microparticle acoustophoresis driven by acoustic radiation forces and streaming-induced drag forces." Lab on a Chip **12**(22): 4617-4627.
- Muller, P. B., M. Rossi, A. Marin, R. Barnkob, P. Augustsson, T. Laurell, C. J. Kaehler and H. Bruus (2013). "Ultrasound-induced acoustophoretic motion of microparticles in three dimensions." Physical Review E **88**(2): 023006.
- Ng, J. W., C. Devendran and A. Neild (2017). "Acoustic tweezing of particles using decaying opposing travelling surface acoustic waves (DOTSAW)." Lab Chip **17**(20): 3489-3497.
- Nyborg, W. L. (1989). "Theoretical criterion for acoustic aggregation." Ultrasound in Medicine & Biology **15**(2): 93-99.
- Pavlic, A., L. Ermanni and J. Dual (2022). "Interparticle attraction along the direction of the pressure gradient in an acoustic standing wave." Physical Review E **105**(5): L053101.
- Pavlic, A., P. Nagpure, L. Ermanni and J. Dual (2022). "Influence of particle shape and material on the acoustic radiation force and microstreaming in a standing wave." Physical Review E **106**(1): 015105.
- Peng, X., W. He, F. Xin, G. M. Genin and T. J. Lu (2020). "The acoustic radiation force of a focused ultrasound beam on a suspended eukaryotic cell." Ultrasonics **108**: 106205.
- Rezk, A. R., L. Y. Yeo and J. R. Friend (2014). "Poloidal Flow and Toroidal Particle Ring

Formation in a Sessile Drop Driven by Megahertz Order Vibration." Langmuir **30**(37): 11243-11247.

Rufo, J., F. Cai, J. Friend, M. Wiklund and T. J. Huang (2022). "Acoustofluidics for biomedical applications." Nature Reviews Methods Primers **2**(1): 30.

Saeidi, D., M. Saghafian, S. Haghjooy Javanmard and M. Wiklund (2020). "A Quantitative Study of the Secondary Acoustic Radiation Force on Biological Cells during Acoustophoresis." Micromachines (Basel) **11**(2).

Schmitt, F. O. (1929). "Ultrasonic micromanipulation." protoplasma **7**(1): 332-340.

Sepehrirahnama, S., F. S. Chau and K.-M. Lim (2016). "Effects of viscosity and acoustic streaming on the interparticle radiation force between rigid spheres in a standing wave." Physical Review E **93**(2): 023307.

Sepehrirahnama, S., K.-M. Lim and F. S. Chau (2015). "Numerical Analysis of the Acoustic Radiation Force and Acoustic Streaming Around a Sphere in an Acoustic Standing Wave." Physics Procedia **70**: 80-84.

Settnes, M. and H. Bruus (2012). "Forces acting on a small particle in an acoustical field in a viscous fluid." Physical Review E **85**(1): 016327.

Shi, W. T. and R. E. Apfel (1996). "Deformation and position of acoustically levitated liquid drops." The Journal of the Acoustical Society of America **99**(4): 1977-1984.

Silva, G. T. and H. Bruus (2014). "Acoustic interaction forces between small particles in an ideal fluid." Physical Review E **90**(6): 063007.

Silva, G. T. and B. W. Drinkwater (2018). "Acoustic radiation force exerted on a small spheroidal rigid particle by a beam of arbitrary wavefront: Examples of traveling and standing plane waves." The Journal of the Acoustical Society of America **144**(5): EL453-EL459.

Silva, G. T., J. H. Lopes, J. P. Leão-Neto, M. K. Nichols and B. W. Drinkwater (2019). "Particle Patterning by Ultrasonic Standing Waves in a Rectangular Cavity." Physical Review Applied **11**(5): 054044.

Simon, G., M. A. Andrade, M. P. Desmulliez, M. O. Riehle and A. L. Bernassau (2019). "Numerical determination of the secondary acoustic radiation force on a small sphere in a plane standing wave field." Micromachines **10**(7): 431.

Svennebring, J., O. Manneberg, P. Skafte-Pedersen, H. Bruus and M. Wiklund (2009). "Selective bioparticle retention and characterization in a chip-integrated confocal ultrasonic cavity." Biotechnology and Bioengineering **103**(2): 323-328.

Vargas-Jiménez, A., M. Camacho, J. D. Muñoz and I. González (2021). "A 3D analysis of the acoustic radiation force in microfluidic channel with rectangular geometry." Wave Motion

**101:** 102701.

Wang, J. and J. Dual (2009). "Numerical simulations for the time-averaged acoustic forces acting on rigid cylinders in ideal and viscous fluids." Journal of Physics A: Mathematical and Theoretical **42**(28): 285502.

Wang, J. and J. Dual (2011). "Theoretical and numerical calculations for the time-averaged acoustic force and torque acting on a rigid cylinder of arbitrary size in a low viscosity fluid." J Acoust Soc Am **129**(6): 3490-3501.

Wang, K., W. Zhou, Z. Lin, F. Cai, F. Li, J. Wu, L. Meng, L. Niu and H. Zheng (2018). "Sorting of tumour cells in a microfluidic device by multi-stage surface acoustic waves." Sensors and Actuators B: Chemical **258**: 1174-1183.

Wang, L. (2018). "Acoustic Radiation Force Based Ultrasound Elasticity Imaging for Biomedical Applications." Sensors **18**(7): 2252.

Wang, Q., A. Riaud, J. Zhou, Z. Gong and M. Baudoin (2021). "Acoustic Radiation Force on Small Spheres Due to Transient Acoustic Fields." Physical Review Applied **15**(4): 044034.

Westervelt, P. J. (1951). "The Theory of Steady Forces Caused by Sound Waves." The Journal of the Acoustical Society of America **23**(3): 312-315.

Westervelt, P. J. (1957). "Acoustic Radiation Pressure." The Journal of the Acoustical Society of America **29**(1): 26-29.

Wijaya, F. B. and K. M. Lim (2016). Boundary Element and Meshless Methods on Acoustics and Vibrations : Paper ICA 2016-181 Boundary element method for acoustic radiation force and torque acting on non-spherical particles.

Wijaya, F. B. and K. M. Lim (2016). "Numerical calculation of acoustic radiation force and torque on non-spherical particles in Bessel beams." Proceedings of Meetings on Acoustics **26**(1): 045002.

Wijaya, F. B., S. Sepehrirahnama and K.-M. Lim (2018). "Interparticle force and torque on rigid spheroidal particles in acoustophoresis." Wave Motion **81**: 28-45.

Wu, M., A. Ozcelik, J. Rufo, Z. Wang, R. Fang and T. Jun Huang (2019). "Acoustofluidic separation of cells and particles." Microsystems & Nanoengineering **5**(1): 32.

Wu, R., K. Cheng, X. Liu, J. Liu, X. Gong and Y. Li (2016). "Study of axial acoustic radiation force on a sphere in a Gaussian quasi-standing field." Wave Motion **62**: 63-74.

Xie, W. J. and B. Wei (2004). "Dynamics of acoustically levitated disk samples." Physical Review E **70**(4): 046611.

Xie, Y., H. Bachman and T. J. Huang (2019). "Acoustofluidic methods in cell analysis." TrAC Trends in Analytical Chemistry **117**: 280-290.

- Yamamoto, D. and A. Shioi (2015). "Self-propelled nano/micromotors with a chemical reaction: Underlying physics and strategies of motion control." KONA Powder and Particle Journal **32**: 2-22.
- Yasui, K., Y. Iida, T. Tuziuti, T. Kozuka and A. Towata (2008). "Strongly interacting bubbles under an ultrasonic horn." Physical Review E **77**(1): 016609.
- Yosioka, K. and Y. Kawasima (1955). "Acoustic radiation pressure on a compressible sphere." Acta Acustica united with Acustica **5**(3): 167-173.
- YupeiQiao, MenyangGong, HaibinWang, JunLan, TengLiu, JiehuiLiu, YiweiMao, AijunHe and XiaozhouLiu (2021). "Acoustic radiation force on a free elastic sphere in a viscous fluid: Theory and experiments." Physics of Fluids **33**(4): 047107.
- Zheng, X. and R. E. Apfel (1995). "Acoustic interaction forces between two fluid spheres in an acoustic field." The Journal of the Acoustical Society of America **97**(4): 2218-2226.
- Zhuk, A. P. (1983). "Interaction of a sound wave with solid particles in a viscous fluid." Soviet Applied Mechanics **19**(11): 1013-1020.
- Zhuk, A. P. (1984). "Hydrodynamic interaction of two spherical particles from sound waves." Soviet Applied Mechanics **20**(9): 875-880.
- Zhuk, A. P. (1985). "Hydrodynamic interaction of two spherical particles due to sound waves propagating perpendicularly to the center line." Soviet Applied Mechanics **21**(3): 307-312.

## Appendix A

The general functional formula for the acoustic radiation force of a plane standing wave used in the literature can be written as:

$$F^{rad} = C\varphi kVE_a \sin(2k\Delta z) \quad (A1)$$

where  $C$  is a constant,  $\varphi$  is a function of surrounding fluid and particle material and the particle's geometry and frequency of the plane wave.  $V$  is the particle's volume,  $E_a$  is the acoustic energy density, and  $\Delta z$  is the particle's position in the standing wave.

Assume a ring, which has minor radius  $a$ , major radius  $R$ , volume  $V$ , density  $\rho_p$ , speed of sound  $c_p$ , and module elasticity  $E$ , is immersed in a fluid with density  $\rho_0$ , speed of sound  $c_0$ , and viscosity of  $\mu$ , subjected to a standing acoustic wave with pressure amplitude  $p_a$ , frequency  $f$ , potential amplitude  $\phi$ . According to Fig A1, the ring's orientation about the x-y plane is indicated by  $\theta$ .

The Eq. (A1) must be modified to create a dimensionless acoustic radiation force. Indicators of the length, mass, and time dimensions among all variables can be chosen as  $a$ ,  $\rho_0$ , and  $c_0$ ; the dimensionless  $\Pi$  numbers for the other variables are as follows:

$$\Pi_{\{R,\Delta z,\rho_p,c_p,p_a,f,\mu\}} = \left\{ \frac{R}{a}, \frac{\Delta z}{a}, \frac{\rho_p}{\rho_0}, \frac{c_p}{c_0}, \frac{p_a}{\rho_0 c_0^2}, \frac{af}{c_0}, \frac{\delta}{a} \right\} \quad (A2)$$

Other variables are not listed among the abovementioned variables, as they can be obtained from the given variables, such as  $\lambda = \frac{c_0}{f}$  and  $k = \frac{2\pi}{\lambda}$ ; therefore,  $\Pi_\lambda = a/\lambda$  or  $\Pi_k = ka$  can be used when it is more convenient rather than  $\Pi_f = \frac{af}{c_0}$ .

The dimensionless acoustic radiation force and torque can be acquired as the following dimensionless groups, by nondimensionalizing the pressure terms by  $\rho_0 c_0^2$ :

$$\Pi_{\{F,\tau\}} = \left\{ \frac{F_{rad}}{\rho_0 c_0^2 a^2}, \frac{\tau_{rad}}{\rho_0 c_0^2 a^3} \right\} \quad (A3)$$

Therefore,  $\Pi$  terms of the force and torque are functions of the seven terms in Eq. (A2) in addition to rotation angle.

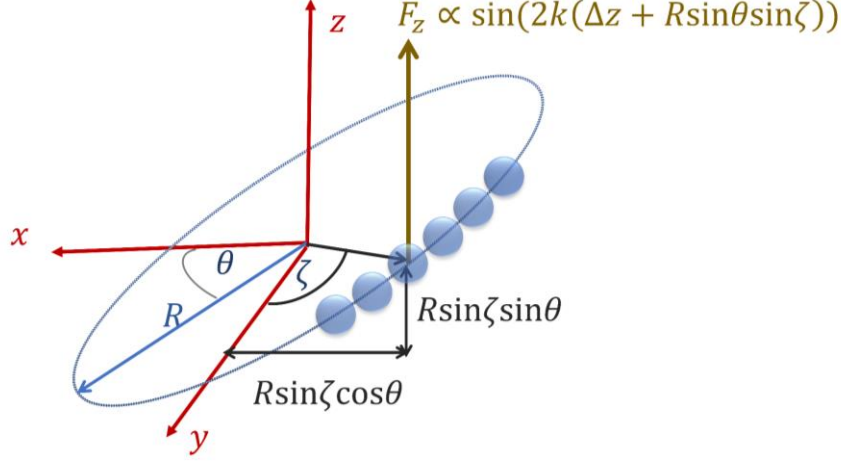


Fig. A1. Representation of the local acoustic radiation force on a tilted ring, which is approximated by a chain of spherical particles.

Using Eqs. (A1) and (A3) , and similar to the analytical solution proposed for the spherical particle in a cosine standing wave in an inviscid fluid (Yosioka & Kawasima, 1955), and modified by other authors for viscous fluid (Settnes & Bruus, 2012), the dimensionless form of the force,  $\mathcal{F}$ , is driven as follows:

$$\mathcal{F} = \frac{4\pi a^3 E_a \phi k \sin(2k\Delta z)}{\rho_0 c_0^2 a^2} \Rightarrow \Pi_F = C \Pi_{p_a}^2 \Pi_k \sin(2\Pi_{\Delta z} \Pi_k) \phi \left( \Pi_{\rho_p}, \Pi_{c_p}, \Pi_{\mu} \right) \quad (\text{A4})$$

where  $\phi$  represents the acoustophoretic contrast factor determined by Eq (3-2), and  $E_a = \frac{1}{4} k_0 p_a^2$  is the acoustic energy density and  $k_0 = \frac{1}{\rho_0 c_0^2}$  is the fluid compressibility. The expression employed in Eq. (4-2) is more precise than the expression mentioned above for inviscid cases but less practical for illustrating the parametric dependences.

The ring is assumed to be comprised of a chain of spherical particles like in Fig. A1 in order to determine how  $\theta$  affects the force. To determine the total force on the rotated ring, the sinusoidal expression in Eq. (A4) is integrated with respect to toroidal angle  $\zeta$ :

$$\begin{aligned} & \int_{-\pi}^{\pi} \sin(2k(\Delta z + R \sin \theta \sin \zeta)) d\zeta \\ &= \int_0^{\pi} \sin(2k(\Delta z + R \sin \theta \sin \zeta)) + \sin(2k(\Delta z - R \sin \theta \sin \zeta)) d\zeta \\ &= \int_0^{\pi} 2 \cos(2Rk \sin \zeta \sin \theta) \sin(2k\Delta z) d\zeta \\ &= 2\pi \sin(2k\Delta z) J_0(2Rk \sin \theta) \end{aligned} \quad (\text{A5})$$

Thus, the zeroth order Bessel function of the first kind  $J_0(2Rk\sin\theta)$  describes how the force acting on the ring depends on the  $\theta$ . The wave number is defined as  $k = \frac{2\pi}{\lambda}$  that results in  $2Rk\sin\theta = 4\pi\sin\theta R/\lambda$ ; for  $R \ll \lambda$ , this effect is insignificant as  $J_0(x) \rightarrow 1$  as  $x \rightarrow 0$ . Therefore, the ARF on small rings slightly varies with the  $\theta$ .

Due to volume-dependency nature of the acoustic radiation force,  $\alpha^2 R$  must take place of the  $\alpha^3$  in Eq. (A4). In this case, the nondimensional force would be proportional to other dimensionless quantities because the pre-factor could be different;

$$\Pi_F \propto \Pi_R \Pi_{p_a}^2 \Pi_k \sin(2\Pi_{\Delta z} \Pi_k) \phi(\Pi_{\rho_p}, \Pi_{c_p}, \Pi_{\mu}) J_0(4\Pi_R \Pi_k \sin\theta) \quad (\text{A6})$$

Integrating the torque on all the spherical particles over the toroidal angle  $\zeta$ , as depicted in Fig. A1, the influence of the  $\theta$  on the torque is obtained:

$$\int_{-\pi}^{\pi} \sin(2k(\Delta z + R\sin\theta\sin\zeta)) R\cos\theta\sin\zeta d\zeta$$

The closed form of this integral, however, cannot be calculated. But, if we take a simplified approach and assume that the ring is made up of two spherical particles representing the opposing segments arranged at  $\zeta = \pm\pi/2$ , the orientation influence on the torque can be approximated as follows:

$$T \propto R\cos\theta \left( F_{\zeta=\frac{\pi}{2}} - F_{\zeta=-\frac{\pi}{2}} \right) = R\cos\theta [\sin(2k(\Delta z + R\sin\theta)) - \sin(2k(\Delta z - R\sin\theta))] \quad (\text{A7})$$

The sinusoidal terms can be simplified as:

$$\sin(2k(\Delta z + R\sin\theta)) - \sin(2k(\Delta z - R\sin\theta)) = \cos(2k\Delta z) \sin(2kR\sin\theta)$$

The influence of the rotation angle on the torque can be represented by  $\sin(2kR\sin\theta) = \sin(4\pi R\sin\theta/\lambda)$ . As a result, in the case of  $R \ll \lambda$  the total torque scales with  $kR\sin\theta$ . Therefore, the dimensionless acoustic torque for tiny rings can be expressed as follows, with cosine dependency on the location and sinusoidal dependence on the orientation:

$$\Pi_T \propto \Pi_R^3 \Pi_{p_a}^2 \Pi_k^2 \cos(2\Pi_{\Delta z} \Pi_k) \sin\theta \phi(\Pi_{\rho_p}, \Pi_{c_p}, \Pi_{\mu}) \quad (\text{A8})$$

The acoustophoretic coefficient,  $\phi(\Pi_{\rho_p}, \Pi_{c_p}, \Pi_{\mu})$ , only takes into account the compression of spherical particles and is not appropriate for the time-harmonic deformation of a slender structures.

To investigate the bending and resonance effects that dominate the time-harmonic torque on the ring in a standing wave, frequencies related to the ring bending modes should be considered; these frequencies depend on not only the ring geometrical parameters but also on the material properties. To explain further, bending frequency,  $f_b$ , scales with  $c_p$ ,  $1/R$ , and  $I_y$  ( $c_p = \sqrt{E/\rho_p}$ ,  $I_y = \pi a^4/4$ ):

$$\Pi_{f_p} \propto \Pi_k \propto \Pi_R^{-1} \Pi_{c_p} \quad (\text{A9})$$

Thus, the corresponding torque of the resonance can be written as:

$$\Pi_T \propto \Pi_R \Pi_{p_a}^2 \Pi_{c_p}^2 \cos(2\Pi_{\Delta z} \Pi_k) \sin\theta \phi(\Pi_{\rho_p}, \Pi_{c_p}, \Pi_{\mu}) \quad (\text{A10})$$